Search for Higgs Boson Production in Association with a W Boson in 1.96-TeV Proton-Antiproton Collisions

Tatsuya MASUBUCHI

February 2008

Search for Higgs Boson Production in Association with a W Boson in 1.96-TeV Proton-Antiproton Collisions

Tatsuya MASUBUCHI
(Doctoral Program in Physics)

Submitted to the Graduate School of Pure and Applied Sciences in Partial Fulfillment of the Requirements for the Degree of Doctor of Philosophy in Science

at the
University of Tsukuba

Abstract

We have searched for the Standard Model Higgs boson production in association with a $W^{\pm}$ boson. This search is based on the data collected between February 2002 and May 2007, corresponding to an integrated luminosity of 1.9 fb^{-1} collected by the Collider Detector at Fermilab (CDF) at the Tevatron which is a $p\bar{p}$ collider at a center of mass energy 1.96 TeV. W+Higgs channel is one of the most promising channels for the Higgs search at Tevatron in the low Higgs mass region ($m_H < 135$ GeV/c^2), where Higgs boson decays into $b\bar{b}$ dominantly. The detection of lepton from the W boson decay makes the W+Higgs events much cleaner than the direct Higgs production events which have the largest production cross section.

Experimentally we select events with a high p_T lepton, high missing transverse energy and two b-quark jets. This signature is same as for the W + jets background which has a huge cross section. To reduce the W + jets background, b-jet identification algorithms are applied to at least one jet.

The expected signal events in $1.9\mathrm{fb}^{-1}$ are 1.82$\pm$0.15 and 1.68$\pm$0.20 for one b-tagged events and two b-tagged events, respectively. The observed data is 805 for one b-tagged events and 173 for two b-tagged events. They are consistent with the Standard Model background expectation. After selecting the events, Neural Network (NN) discriminant technique is performed to distinguish the signal events from still residual backgrounds. We see no evidence for a Higgs signal in the dijet mass distribution and in the NN output distribution. We set a 95% confidence level upper limit on the W+Higgs production cross section times the branching ratio of the Higgs decaying into a $b\bar{b}$ pair. We obtained $\sigma(p\bar{p} \rightarrow W^{\pm}H) \times BR(H \rightarrow b\bar{b}) < 1.4$ to 0.9 pb for Higgs masses from 110 GeV/c^2 to 150 GeV/c^2 using the NN output distribution. The limits are about 10 times higher than the Standard Model expectation in the low Higgs mass region.

Acknowledgments

I would like to express my thanks to all of the people who supported and encouraged me during the course of my Ph.D programs. I would like to thank Prof. Shinhong Kim. He welcomed me to the elementary particle experiment laboratory when Prof. Kunitaka Kondo retired from Waseda and provided me a great opportunity to study high-energy experimental physics at CDF Run II and financial supports in staying at Fermilab. He also read this thesis and gave me a lot of invaluable suggestions and comments.

I would like to thank the leader of the analysis group, Prof. Weiming Yao. He gave me a great opportunity to work on this analysis. He understood my situations and always encouraged me providing useful comments. I was very impressed with his dedicated attitude toward high energy physics and his kindness. I also would like to thank other members, Prof. Jason Nielsen, Prof. Anyes Taffard, Prof. Richard Huges, Prof. Brain Winer, Dr. Kevin Lannon, Prof. Jay Dittmann and Dr. Nils Krumnack. Their experiences in l+jets analysis provided numberless suggestions and advices. Their educational and kind attitudes encouraged me. I would like to thank Jason Slaunwhite, Martin Frank and Yoshikazu Nagai. Their attitude for analysis was very impressive. I enjoyed discussion with them. I also would like to thank Dr. Yoshio Ishizawa and Dr. Yoshiaki Kusakabe who carried out the analysis previously. They provided useful information and comments based on their experiences and knowledges in Higgs search. I could not have completed this analysis without their supports.

I would like to express many thanks to Prof. Matthew Herndon and Prof. Mark Kruse for the convener-ship in the Higgs Discovery group. I also would like to thank Dr. Chris Neu, Dr. Sebastian Grinstein, Dr. Kenichi Hatakeyama, Prof. Tomas Junk, Dr. Anton Anastassov, Prof. Song Ming Wang, Prof Jane Natchman, Douglus Glenzinski and Robin Erbacher for the convener-ship. They helped me and led this analysis to the correct direction when I faced difficult situations.

I also appreciate Prof. Makoto Shimojima, Prof. Hiroyuki Matsunaga, Prof. Frank Chlebana, Prof. Willis Sakumotom, Dr. Ilija Bizjak, Prof. Dehong Zhang, Geum Bong Yu and all members in the CSL upgrade project.

I want to say thanks to Ms. Kazuko Kumashiro, Ms. Kyoko Kunori, Ms. Carol Picciolo, Ms. Barbara Perington, and Ms. Dee Hahn. They supported me with a lot of kindness, setting up trips and other secretary works.

I would like to thank the staff members of the University of Tsukuba, Prof. Fumihiko Ukegawa, Kazuhiko Hara, Takasumi Maruyama, Yuji Takeuchi, Dr. Tomonobu Tomura, Hideki Miyake, Masakazu Kurata and Takashi Akimoto. Discussions with them were invaluable to polish up this analysis. I also thank the staff members of other universities and the students in CDF Japan group, Prof. Toru Okusawa, Prof. Yukihiro Kato, Prof. Kazuhiro Yamamoto, Prof. Reisaburo Tanaka and Prof. Ituo Nakano, and Mr. Junji Naganoma, Mr. Taichi Kubo, Mr. Naoki Kimura, Ms. Ai Nagano, Mr. Koji Nakamura, Mr. Takayuki Wakisaka. I also thank Prof. Shyuichi Kunori, Prof. Nobuaki Oshima, Prof. Kaori Maeshima, Dr. Kohei Yorita, Dr. Koji Sato, Dr. Yuji Enari, Dr. Masato Aoki and the members of university of Kyoto. I enjoyed the discussion, lunch and dinner parties and exercises with them during the two year life at Fermilab. I also thank Fermilab' Soccer members. I enjoyed soccer with the members from various countries who are my friends. The Soccer game made me relief from my difficulties and were good opportunities to exercise.

I thank the Fermilab staff and the technical staffs of the participating institutions for their vital contributions. This work was supported by U.S. Department of Energy and National Science Foundation; the Italian Instituto Nazionale di Fisica Nucleare; the ministry of Education, Culture, Sports, Science and Technology of Japan; the Natural Sciences and Engineering Research Council of Canada; the National Science Council of the Republic of China; the Swiss

Notional Science Foundation; the A.P. Sloan Foundation; the Bundesministerium fuer Bildung und Forschung, Germany; the Lorean Science and Engineering Foundation and the Lorean Research Foundation; the Particle Physics and Astronomy Research Council and the Royal Society, UK; the Russian Foundation for Basic Research; the Comision Interministerial de Cienciay Tecnologia, Spain; in part by the European Community's Human Potential Programme under contract HPRN-CT-2002-00292, Probe for New Physics; and by the Research Fund of Istanbul University Project No.1755/21122001.

I would like to thank my parents, Toshio, Teruko and Kenji. They provided me the financial support, and grateful encouragement. I can never thank you enough.

Finally I thank Madoka Shintani earnestly. She always cheered me up from Japan and visited to me many times. The life with her made me relax and encourage at U.S. She's the best person who understanding my situation. I could not accomplish this thesis without her understanding, kindness, encouragement and love. The thesis is dedicated to her as well.

Contents

List of Figures

List of Tables

Chapter 1

Introduction

What is the matter? In ancient Greece, Demokritos first established atomism and he believed the existence of *atom*, which was the un-dividable particle when the matter was divided to smaller pieces. The discovery of ultimate elementary particle is the one ultimate goal of elementary particle physics.
Why does the matter have mass? What is the origin of mass? Human has extended the knowledge since Isaac Newton first introduced the mass in Philosophiae Naturalis Principia Mathematica. In the beginning of 20th century, Albert Einstein advocated mass-energy equivalence, in other words, the mass can convert to the energy as this equation, $E = mc^2$, in relativity.

Human absolutely has deepened the scientific knowledge for the mass since human knows the mass. However nobody knows the answer yet for the question that what is the origin of mass yet.

In current elementary particle physics, the theory called the Standard Model is the most successful one. The quarks and leptons are introduced as the particles for matter constituents and the Higgs boson is considered as the particle giving masses to the elementary particles. Are the quarks and leptons are the ultimated elementary particles? Is this Higgs boson the origin of mass? If that's the case, the Human's knowledge reach to the origin of mass and obtain the Demokritos's *atom* by the progress of the elementary particle physics.

1.1 The Standard Model

The Standard Model (SM) in current elementary particle physics is based on the gauge theory and some symmetries. It describes three forces, strong, weak and electromagnetic, except for gravity out of the four known fundamental forces. The force is a result of mediating gauge bosons. Dynamics and behavior of matter and energy is well-described by this model. This model is most successful since it is most precisely tested in many various experiments.

The Standard Model is based on the gauge symmetry group $\mathrm{SU}(3)_C \otimes \mathrm{SU}(2)_L \otimes \mathrm{U}(1)_Y$. The first gauge group $\mathrm{SU}(3)_C$ describes the strong interaction known as Quantum Chromodynamics (QCD) [1, 2], where suffix C stands for the color charge carried by the gauge bosons, gluon (g), mediating strong interaction.

Next, two gauge groups $\mathrm{SU}(2)_L \otimes \mathrm{U}(1)_Y$ describe the electroweak interactions [3–5] unifying weak and electromagnetic (EM) interaction. Where L and Y stand for left-handed weak isospin and hypercharge. The weak interaction is mediated by weak bosons (W/Z) and electromagnetic interaction is mediated by photons (γ). These gauge bosons and fermions which construct matters were already discovered and the various experiments prove that the Standard Model is right to extreme precision. However the Higgs boson which gives particles their masses with keeping

gauge invariance is the only particle undiscovered in the Standard Model prediction.

1.1.1 Elementary Particles of the Standard Model

Our world consists of fermions which construct matter and gauge bosons which mediate the force. The properties and classification of these particles are described below.

Fermions - matter particles -

The leptons and quarks are considered as the elementary particles composing matters in our universe. The fermions have half-integer spins and obey the Pauli exclusion principle.

There are six kinds of leptons in three generations of weak isospin doublets consisting of neutral and charged leptons. The charged leptons are electron (e), muon (μ) and tau (τ), and the neutral leptons are three kinds of neutrinos corresponding to the charged leptons. The charged lepton has an integer charge and is colorless. Neutrinos are assigned as weak isospin $+1/2$ and charged leptons are $-1/2$.

There are also six kinds of quarks similarly. The up-type (down-type) quark has a charge of $2/3(-1/3)$ and an weak isospin of $+1/2(-1/2)$. These quarks carry the color charge of the strong interactions. Historically before the existence of quark was proved, hadrons were considered as elementary particles. However, as a lot of hadrons were observed in 1960s it became difficult to consider them as elementary particles. Now the hadrons are categorized by the inner structure, quarks. This quark model was advocated originally by Gell-Mann [7].

For each particle, an anti-particle which has the opposite quantum numbers to the particle exists. In Table 1.1, the properties of quarks and leptons are shown.

Bosons - particles mediating force -

The gauge bosons are particles that mediate the force. Three forces, electromagnetic, weak and strong, are described within the Standard Model and specific gauge bosons are mediated corresponding to each interaction. They have an integer spin of 1. One force, gravity, is not included in the Standard Model because it is negligibly small in the Standard Model energy scale. The boson mediating gravity is predicted as a graviton which has spin 2 in some theories [8,9]. If the graviton is discovered in future, it proves that all forces is mediated by bosons beyond the Standard Model. In Table1.2, boson properties are summarized.

	Generation			Properties			
	1st	2nd	3rd	Spin	Weak isospin	Charge	Interaction
Quarks	u	c	t	$1/2$	$+1/2$	$+2/3$	EM, Weak, Strong
	d	s	b		$-1/2$	$-1/3$	
Leptons	ν_e	ν_μ	ν_τ	$1/2$	$+1/2$	0	Weak
	e	μ	τ		$-1/2$	-1	EM, Weak

Table 1.1: The elementary particles in the Standard Model. There are also antiparticles for each lepton and quark. The antiparticles are exactly the same as the particles with opposite signs of quantum numbers such as charge, isospin, lepton number and baryon number.

		Mass (GeV/c^2)	Spin	Charge	Interaction
Vector bosons	W	80.4	1	±1	Weak
	Z	91.2		0	EM, Weak
	γ	0		0	EM
	g	0		0	Strong
Scalar boson	H	unknown	0	0	Yukawa

Table 1.2: The properties of bosons in the Standard Model.

1.1.2 Gauge Theory Overview

The Standard Model description, SU(3)$_C \otimes$ SU(2)$_L \otimes$ U(1)$_Y$, is based on the gauge theory. The gauge theory requires the gauge invariance in the relativistic quantum field theory. The gauge invariance means that a Lagrangian is invariant under a certain symmetry transformation described below. In the gauge theory, gauge bosons are introduced by imposing a local gauge invariance and then the Lagrangian is able to describe the interaction between a gauge field and a matter field. However, the introduced gauge bosons should be massless imposed by the gauge invariance. W and Z bosons have massive masses though photons and gluons are massless. To overcome this difficulty, a Higgs boson is introduced [10]. In the following sections, we show how to introduce the gauge bosons by imposing the gauge invariance on the Lagrangian for a free Dirac field under SU(2) and U(1) groups and show how a massless gauge boson acquires its mass by introducing the spontaneous symmetry breaking so called the Higgs mechanism.

1.1.3 Electromagnetic, U(1) Group, Gauge Transformation

The electromagnetic interaction is described as Quantum Electrodynamics (QED) in U(1) group. In this section, we first start from a free Dirac field like an electron, then introduce the conserved current and the gauge field under global and local gauge transformations.

The Lagrangian for a free Dirac field $\psi(x)$ with spin 1/2, mass m and charge eQ is given by the following equation

$$\mathcal{L} = i\bar{\psi}(x)\gamma_\mu\partial^\mu\psi(x) - m\bar{\psi}(x)\psi(x) \tag{1.1}$$

where $\bar{\psi}(x)$ is defined as $\psi^\dagger(x)\gamma^0$. The Dirac equation is obtained by substituting this Lagrangian in the Euler-Lagrange equation. Obviously Eq. 1.1 is invariant under the following global transformation

$$\psi(x) \rightarrow \psi'(x) = e^{iQ\alpha}\psi(x) \tag{1.2}$$

where Q is the charge of the field and α is a continuous real parameter. According to Noether's theorem, if a system is invariant under a continuous transformation, a conserved current and associated charge exists. In fact, there is the following conserved current

$$j^\mu = e\bar{\psi}\gamma^\mu Q\psi \tag{1.3}$$

satisfying $\partial_\mu j^\mu = 0$. Then conserved charge is provided by integrating the 0-th component.

$$eQ = \int d^3x j^0 \tag{1.4}$$

Next, we consider a local gauge transformation instead of the global gauge transformation. It corresponds to changing α to $\alpha(x)$ which depends on the space-time point x. Under the local

gauge transformation, Lagrangian 1.1 is not invariant as the partial derivative term introduces an extra term. To compensate the extra term, a real gauge field and a covariant derivative D_μ are introduced as follows,

$$D_\mu(x) \equiv \partial_\mu(x) - ieQA_\mu(x) \tag{1.5}$$

$$A_\mu(x) \to A_\mu(x) + \frac{1}{e}\partial_\mu\alpha(x) \tag{1.6}$$

Under the transformation, a newly introduced photon field $A_\mu(x)$ in the Lagrangian provides local gauge invariance. Finally the invariant Lagrangian under U(1) local gauge transformation is given in adding a kinetic term of gauge field,

$$\mathcal{L} = \bar{\psi}(i\gamma^\mu\partial_\mu - m)\psi + e\bar{\psi}\gamma^\mu QA_\mu\psi - \frac{1}{4}F_{\mu\nu}F^{\mu\nu} \tag{1.7}$$

where the term of the field strength $F_{\mu\nu}$ is defined as

$$F_{\mu\nu} = \partial_\mu A_\nu(x) - \partial_\nu A_\mu(x) \tag{1.8}$$

The mass therm $\frac{1}{2}m^2A_\mu A^\mu$ is not allowed due to gauge invariance. Therefore the photon is massless which is consistent with the experimental observation and ensure that the electromagnetic force has infinite range.

1.1.4 SU(2) $\otimes$ U(1) Electroweak Theory

The electroweak theory which unified the electromagnetic and weak interactions was established by Glashow, Weinberg and Salam [3–5]. It is based on SU(2)$_L$ $\otimes$ U(1)$_Y$ symmetry group. The electromagnetic symmetry group, U(1)$_Q$, is included as a subgroup of the electroweak symmetry group. The gauge bosons of electroweak interaction are introduced by requiring local gauge invariance in the massless fermion field $i\psi\gamma^\mu\partial_\mu\psi$.

The local gauge transformation for SU(2)$_L$ $\otimes$ U(1)$_Y$ group is

$$\psi'_L(x) = U\psi_L(x) \tag{1.9}$$

$$\psi'_R(x) = U\psi_R(x), \tag{1.10}$$

where ψ_L and ψ_R mean the left-handed and right-handed fermions respectively. The SU(2)$_L$ group transformation operates only on the left-handed fermions. Here U is defined as

$$U = \exp(i\boldsymbol{\alpha}(x)\cdot\boldsymbol{T}_i + i\beta(x)Y) \tag{1.11}$$

$\boldsymbol{T}$ is a generator of the SU(2) group defined as $T_i = \frac{1}{2}\tau_i$. τ_i is the Pauli spin matrix. Y is a generator of the U(1) group. The weak charge is given by $Q = T_3 + \frac{Y}{2}$. $\boldsymbol{\alpha}(x)$ and $\beta(x)$ are real and continuous parameters which represent the phases.

Under this local gauge transformation, the covariant derivative and vector boson field are introduced to keep the gauge invariance.

$$D_\mu = \partial_\mu + ig\boldsymbol{T}\cdot\boldsymbol{W}_\mu(x) + ig'\frac{Y}{2}B_\mu(x) \tag{1.12}$$

$$\boldsymbol{W}_\mu(x) \to \boldsymbol{W}_\mu(x) - \frac{1}{g}\partial_\mu\boldsymbol{\alpha}(x) - \boldsymbol{\alpha}(x)\times\boldsymbol{W}_\mu(x)$$

$$B_\mu(x) \to B_\mu(x) - \frac{1}{g'}\partial_\mu\beta(x)$$

where $\boldsymbol{W}_\mu(x)$ is three gauge fields introduced from the SU(2)$_L$ local gauge transformation, and $B_\mu(x)$ is a gauge field introduced from U(1)$_Y$. g and g' stand for coupling for each interaction. The Lagrangian including kinetic energy term of the gauge fields is given by

$$\mathcal{L} = i\bar{\psi}\gamma^\mu\partial_\mu\psi \tag{1.13}$$

$$+ \bar{\psi}_L\gamma^\mu\left[-\frac{g}{2}\boldsymbol{\tau}\cdot\boldsymbol{W}_\mu - \frac{g'}{2}YB_\mu\right]\psi_L \tag{1.14}$$

$$- \bar{\psi}_R\gamma^\mu\frac{g'}{2}YB_\mu\psi_R \tag{1.15}$$

$$- \frac{1}{4}\boldsymbol{W}_{\mu\nu}\boldsymbol{W}^{\mu\nu} - \frac{1}{4}B_{\mu\nu}B^{\mu\nu} \tag{1.16}$$

where $\boldsymbol{W}_{\mu\nu}$ and $B_{\mu\nu}$ are defined as

$$\boldsymbol{W}_{\mu\nu} = \partial_\mu\boldsymbol{W}_\nu - \partial_\nu\boldsymbol{W}_\mu - g\boldsymbol{W}_\mu\times\boldsymbol{W}_\nu, \tag{1.17}$$

$$B_{\mu\nu} = \partial_\mu B_\nu - \partial_\nu B_\mu. \tag{1.18}$$

Here, the last term of $\boldsymbol{W}_{\mu\nu}$ arises from the non-Abelian character of the SU(2) group.

This gauge invariance is preserved by ensuring that the fields are massless. The charged W bosons ($W^\pm$) are mixed states of W^1_μ and W^2_μ as given by

$$W^\pm_\mu = \frac{1}{\sqrt{2}}(W^1_\mu \mp iW^2_\mu), \tag{1.19}$$

while W^3_μ and B_μ are neutral fields and the physical neutral gauge fields A_μ and Z_μ are mixed states of W^3_μ and B_μ. This mixing angle is called the Weinberg angle θ_W. It relates to the couplings of the electromagnetic and weak interactions according to $g\sin\theta_W = g'\cos\theta_W = e$.

$$\begin{pmatrix} A_\mu \\ Z_\mu \end{pmatrix} = \begin{pmatrix} \cos\theta_W & \sin\theta_W \\ -\sin\theta_W & \cos\theta_W \end{pmatrix}\begin{pmatrix} B_\mu \\ W^3_\mu \end{pmatrix} \tag{1.20}$$

The gauge bosons are naturally introduced by requiring gauge invariance, but they are still massless. Mass terms such as $\frac{1}{2}m_V^2V_\mu V^\mu$ for bosons and $m\bar{\psi}\psi$ for fermions would violate the gauge invariance of the Lagrangian. The actually observed W and Z bosons and quarks are massive. In the next section, the Higgs mechanism is introduced to give masses without violating the gauge invariance.

1.1.5 Spontaneous Symmetry Breaking and the Higgs Mechanism

In the proceeding section, the four massless gauge bosons, γ, $W^\pm$ and Z^0 were introduced in the electroweak theory. These bosons need to be massless in order to preserve the local gauge invariance of the Lagrangian. However it is not consistent with actual experimental results. An SU(2) doublet of complex scalar field is introduced and the following Gauge invariant Lagrangian SU(2) $\otimes$ U(1) is considered as follows,

$$\mathcal{L}_\mathcal{H} = (D_\mu\phi(x))^\dagger(D^\mu\phi(x)) - V(\phi) \tag{1.21}$$

$$V(\phi) = \mu^2\phi^\dagger\phi + \lambda(\phi^\dagger\phi)^2 \tag{1.22}$$

where

$$\phi = \begin{pmatrix} \phi^+(x) \\ \phi^0(x) \end{pmatrix} = \frac{1}{\sqrt{2}}\begin{pmatrix} \phi_1(x) + i\phi_2(x) \\ \phi_3(x) - i\phi_4(x) \end{pmatrix} \tag{1.23}$$

The covariant derivative D_μ is the same as Eq. 1.12. This Lagrangian keeps the local gauge invariance. If μ^2 is positive, this Lagrangian describes the four scalar fields ϕ_i interact with the massless electroweak gauge bosons. However if μ^2 is negative, the symmetry breaks spontaneously and the weak gauge bosons acquire masses. The potential $V(\phi)$ shape is shown in Figure 1.1.

The minimum of potential $V(\phi)$ for $\mu^2 < 0$ shifts to

$$|\phi|^2 = \phi^\dagger\phi = \frac{1}{2}(\phi_1^2 + \phi_2^2 + \phi_3^2 + \phi_4^2) = -\frac{\mu^2}{2\lambda} \equiv \frac{v^2}{2} \tag{1.24}$$

Thus the ground state due to $\mu^2 < 0$ moves to $\phi \neq 0$. It is natural to expand the Lagrangian around the ground state $\phi = v$. It means that the symmetry is broken spontaneously.

$\phi(x)$ is expanded around a minimum potential state, $\phi_3 = v$, $\phi_1 = \phi_2 = \phi_4 = 0$. The ground state called a vacuum state is given by

$$\phi_0 \equiv \frac{1}{\sqrt{2}}\begin{pmatrix}0\\ v\end{pmatrix} \tag{1.25}$$

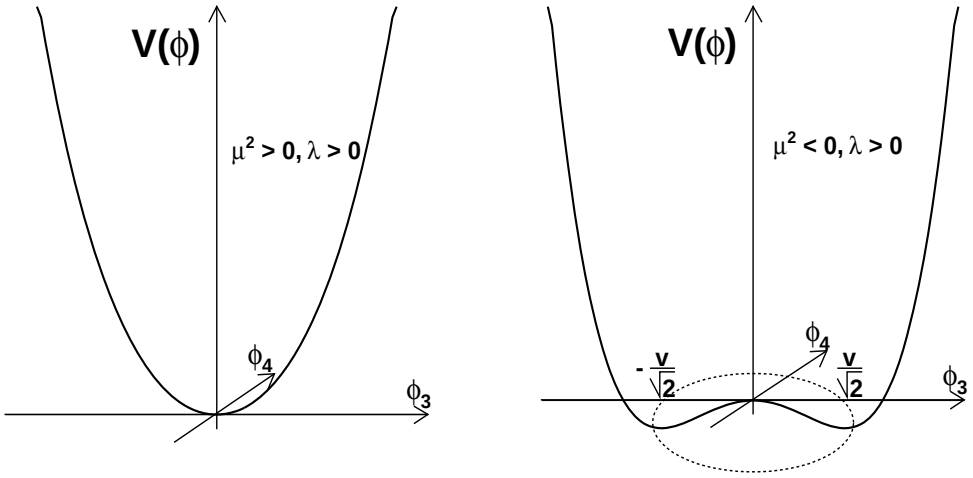

Figure 1.1: Potential $V(\phi)$ with $\mu^2 > 0$ and $\lambda > 0$ (Left), with $\mu^2 < 0$ and $\lambda > 0$ (Right).

Now, expand around this vacuum state as $\phi_3(x) = v + \eta_3(x)$ and $\phi_4(x) = \eta_4(x)$, where η is the quantum fluctuation around this vacuum state. The Lagrangian expresses the appearance of a neutral scalar gauge boson which has $m = \sqrt{2\lambda v^2}$, the Higgs boson H with respect to a new field η_3 and three unwanted massless Numbu-Goldstone bosons ϕ_1, ϕ_2 and η_4. These Numbu-Goldstone bosons can be removed by applying a unitary gauge transformation. In other words, the gauge fields eat Numbu-Goldstone bosons and acquire the masses and hence the longitudinal polarization states. This is called Higgs mechanism. Finally the scalar field is modified as

$$\phi(x) = \frac{1}{\sqrt{2}}\begin{pmatrix}0\\ v + H(x)\end{pmatrix} \tag{1.26}$$

The masses of the gauge bosons in the electroweak interaction is given by

$$\left|\left(ig\boldsymbol{T}\cdot W_\mu + ig'\frac{Y}{2}B_\mu\right)\phi(x)\right|^2 = \frac{1}{8}\left|\begin{pmatrix} gW_\mu^3 + g'B_\mu & g(W_\mu^1 - iW_\mu^2) \\ g(W_\mu^1 + iW_\mu^2) & -gW_\mu^3 + g'B_\mu \end{pmatrix}\begin{pmatrix}0\\ v\end{pmatrix}\right|^2 \tag{1.27}$$

$$= \frac{1}{8}v^2g^2((W_\mu^1)^2 + (W_\mu^2)^2) + \frac{1}{8}v^2(g'B_\mu - gW_\mu^3)^2 \tag{1.28}$$

$$= \left(\frac{1}{2}vg\right)^2 W_\mu^+ W^{-\mu} + \frac{1}{2}\left(\frac{1}{2}v\sqrt{g^2+g'^2}\right)^2 Z_\mu Z^\mu \tag{1.29}$$

The last line of this equation represents, the mass terms for the charged gauge bosons and the neutral gauge boson. Therefore the acquired masses from the Higgs mechanism are given by

$$m_W = \frac{1}{2}vg \tag{1.30}$$

$$m_Z = \frac{1}{2}v\sqrt{g^2+g'^2} \tag{1.31}$$

$$m_\gamma = 0 \tag{1.32}$$

The mass of the Higgs boson introduced for breaking symmetry is given by

$$m_h = \sqrt{2\lambda}v \tag{1.33}$$

1.1.6 Fermion Masses

The fermions are capable of acquiring masses by the same Higgs doublet as introduced above. We consider that the following Lagrangian which is SU(2)⊗U(1) gauge invariant to generate lepton masses.

$$\mathcal{L}_{\text{Yukawa}} = -G_l[\bar{\chi}_L\phi\psi_R + \bar{\psi}_R\phi^\dagger\chi_L] \tag{1.34}$$

where χ_L and ψ_R represent isospin doublet of left-handed lepton and isospin singlet of right-handed lepton such as

$$\chi_L = \begin{pmatrix}\nu_\ell \\ \ell\end{pmatrix}_L, \psi_R = \ell_R \tag{1.35}$$

After spontaneous symmetry breaking, Lagrangian obtains the following equation by using Eq.1.26

$$\mathcal{L}_{\text{Yukawa}} = -\frac{G_\ell}{\sqrt{2}}v(\bar{\ell}_L l_R + \bar{\ell}_R\ell_L) - \frac{G_\ell}{\sqrt{2}}(\bar{\ell}_L\ell_R + \bar{\ell}_R\ell_L)h \tag{1.36}$$

where leptons are capable of acquiring masses by defining lepton masses as $m_\ell = \frac{G_\ell}{\sqrt{2}}v$. However we can not predict the lepton masses because G_ℓ is an arbitrary parameter.

For quarks, masses are generated similarly. The one difference is the treatment for the up-type of quark isospin doublet. To generate up-type fermion masses, the charge-conjugate Higgs doublet is introduced:

$$\phi_c = i\tau_2\phi = \begin{pmatrix}-\bar{\phi}^0 \\ \phi^-\end{pmatrix} \xrightarrow[\text{symmetry breaking}]{} \frac{1}{\sqrt{2}}\begin{pmatrix}v + H(x) \\ 0\end{pmatrix} \tag{1.37}$$

The gauge invariance Lagrangian is

$$\mathcal{L}_{\text{Yukawa}} = -G_d^{ij}(\bar{u}_i, \bar{d}_i')_L\phi d_{jR} - G_u^{ij}(\bar{u}_i, \bar{d}_i')_L\phi_c u_{jR} + h.c. \tag{1.38}$$

In the similar way to the lepton case, after the spontaneous symmetry breaking, this Lagrangian becomes

$$\mathcal{L}_{\text{Yukawa}} = -\frac{G_d^i}{\sqrt{2}}v\bar{d}_i d_i - \frac{G_u^i}{\sqrt{2}}v\bar{u}_i u_i - \frac{G_d^i}{\sqrt{2}}\bar{d}_i d_i h - \frac{G_u^i}{\sqrt{2}}\bar{u}_i u_i h \tag{1.39}$$

To obtain this equation, the Lagrangian is diagonalized. Up-type quarks and down-type quarks acquire masses, $m_u = G_u^i v/\sqrt{2}$ and $m_d = G_d^i v/\sqrt{2}$, respectively, where G_d and G_d are arbitrary parameters which are proportional to the fermion masses.

In general, the mass of any fermion depends on the coupling constant, arbitrary parameter G_f and is proportional to it.

$$m_f = \frac{G_f v}{\sqrt{2}} \tag{1.40}$$

The $v \sim 246$ GeV is calculated but the mass of fermion is not predicted by this theory because the coupling constant is a free parameter. The neutral Higgs boson mass is also not predicted. All of these parameters need to be measured experimentally.

Currently the Higgs boson itself is not detected and the Higgs potential shape is not understood. When the Higgs boson is discovered, it must be followed to measure the potential shape causing the spontaneous symmetry breaking and the vacuum state to give the particles their masses.

1.2 Higgs Boson Properties and Experimental Background

In the previous section, we described how the Higgs mechanism was introduced in the Standard Model. In this section we discuss some theoretical and experimental constraints on the Higgs boson, mass and the properties of Higgs boson and describe how the Higgs boson is searched at the Tevatron in this section. Then we give an experimental overview summarizing the previous experimental results.

1.2.1 Theoretical Constraint on the Higgs Boson Mass

There are interesting theoretical constraints on the Higgs mass which can be derived from assumptions on the energy range where the Standard Model is valid before perturbation theory breaks down and new phenomena should emerge. In this section, the theoretical constraint on the Higgs boson mass is discussed.

First, the Feynman diagrams for the tree-level and one loop corrections to the Higgs boson self-coupling are considered. The typical Feynman diagrams are shown in Figure 1.2. The variation of the quartic Higgs coupling with the energy scale Q is described by the Renormalization Group Equation [11]. The solution is written in choosing the natural reference energy point to be the electroweak symmetry breaking scale, $Q_0 = v$:

$$\lambda(Q^2) = \lambda(v^2)\left[1 - \frac{3}{4\pi^2}\lambda(v^2)\log\frac{Q^2}{v^2}\right]^{-1} \tag{1.41}$$

According to this solution, if the energy is much smaller than the electroweak breaking scale, $Q^2 \ll v^2$, the quartic coupling becomes extremely small $\lambda(Q^2) \sim 0$ and the theory is trivial as the coupling is zero. In the opposite limit, In $Q^2 \gg v^2$ case, the quartic coupling eventually becomes infinite, $\lambda(Q^2) \sim \infty$. This point is called Landau pole, where the coupling becomes infinite at the energy, Λ_C. The relation between this energy and the Higgs boson mass is given by

$$m_h^2 = \frac{8\pi^2 v^2}{3\log\left(\Lambda_C^2/v^2\right)} \tag{1.42}$$

The Higgs mass should be smaller than m_h to avoid the Landau pole. For example, the Higgs boson mass should be less than $m_h \leq 200$ GeV/c^2 for the value $\Lambda_C \sim 10^{16}$ GeV. If the cut-off Λ_C is small, $\Lambda_C \sim 10^3$ GeV, the Higgs boson mass is allowed to be the order of 1 TeV.

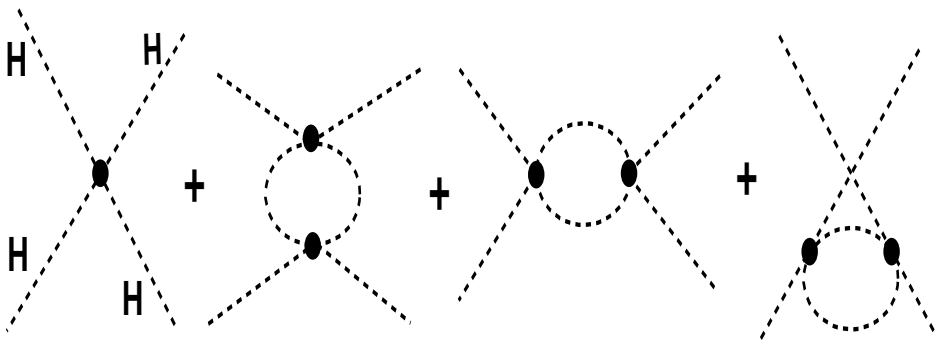

Figure 1.2: The typical Feynman diagrams for the tree-level and one loop Higgs self-coupling.

Next, we consider the lower bound on the Higgs mass to include the contributions from fermions and gauge bosons on the running of the quartic coupling λ. Actually we consider only the contributions of top quark and massive gauge bosons, which is a good approximation because the Higgs boson couplings are proportional to the particle masses. Typical Feynman diagrams for these additional contributions are shown in Figure 1.3.

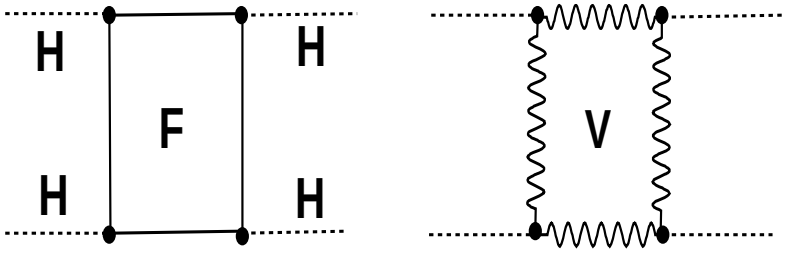

Figure 1.3: The Feynman diagrams for one loop contributions of fermions and gauge bosons on the Higgs mass.

The following equation is obtained from one loop renormalization group equation [11] for the quartic coupling, including the heaviest fermion, top quark, and gauge boson contributions.

$$\lambda(Q^2) = \lambda(v^2) + \frac{1}{16\pi^2}\left[-12\frac{m_t^4}{v^4} + \frac{3}{16}(2g^4 + (g^2 + g'^2)^2)\right]\log\frac{Q^2}{v^2} \qquad (1.43)$$

where, m_t is the mass of top quark. According to this equation, if the coupling λ is too small, the

top quark contribution can be dominant and λ could take negative value $\lambda(Q^2) < 0$, leading to a scalar potential $V(Q^2) < V(v)$. The vacuum is not stable since the potential shape does not have minimum. The stability argument requires to keep $\lambda(Q^2) > 0$, then the Higgs boson mass should be larger than the value.

$$m_h^2 > \frac{3}{8\pi^2 v^2}\left[4m_t^4 - 2m_W^4 - m_Z^4\right]\log\frac{Q^2}{v^2} \tag{1.44}$$

This equation gives the constraint on the Higgs boson mass, which depends on the value of the cut-off Λ_C. For example, $m_h > 70$ GeV/c^2 at $\Lambda_C \sim 10^3$ GeV and $m_h > 130$ GeV/c^2 at $\Lambda_C \sim 10^{16}$ GeV.

Finally, Figure 1.4 shows the allowed region of Higgs mass as a function of cut-off scale Λ after taking higher order effects into account [11]. This upper bound is obtained from the triviality and the lower bound is obtained from the stability of vacuum as discussed above. If the new physics scale Λ_C is at the TeV scale, the Higgs boson mass is allowed to be in the range

$$50 \text{ GeV}/c^2 < m_h < 800 \text{ GeV}/c^2$$

while, if we require the Standard Model to be valid up to the Grand Unification scale, $\Lambda_{GUT} \sim 10^{16}$ GeV, the Higgs boson mass should lie in the range

$$130 \text{ GeV}/c^2 < m_h < 180 \text{ GeV}/c^2$$

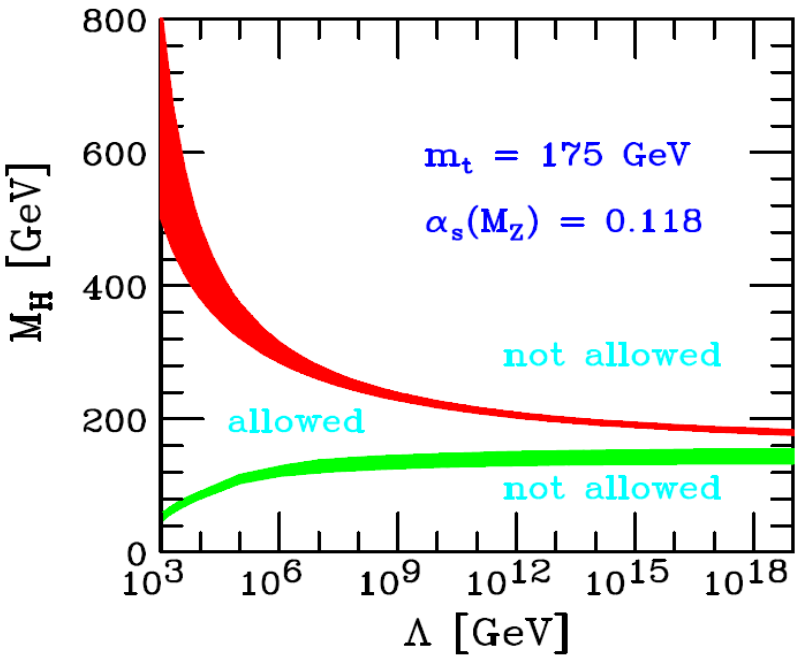

Figure 1.4: The triviality bound and the vacuum stability bound on the Higgs boson mass as a function of cut-off scale Λ.

1.2.2 Higgs Boson Production and Decay at the Tevatron

The Tevatron located in Fermilab is currently the only accelerator in the world which is capable of searching directly for the Higgs boson. It is a $p\bar{p}$ collider with a center of mass energy of 1.96 TeV. The difficulties to search for the Higgs boson at the Tevatron are caused by huge hadronic background. At first the decay properties of the Higgs boson are described. Figure1.5 shows the branching ratio as a function of Higgs mass in Tevatron search region. The branching ratio is calculated using HDECAY program [13, 14]. The main decay mode is $b\bar{b}$ in the low Higgs mass region less than 135 GeV/c^2, and W^+W^- and Z^0Z^0 in the high Higgs mass region more than 135 GeV/c^2. In the mass region above the mass of these boson pairs, the decay is dominated by the two channels, W^+W^- and Z^0Z^0. In the low Higgs mass region, the Higgs boson also decays into various fermion/boson pairs ($H \rightarrow \tau^+\tau^-, c\bar{c}$ and gg) in addition to $b\bar{b}$. Especially τ pair decay channel where signal-to-background ratio is tolerable, is searched by identifying characteristic τ decay. $H \rightarrow \gamma\gamma$ channel which provides very clean signature and allows very precise mass measurement signature has been studied at CDF though the branching ratio is too small.

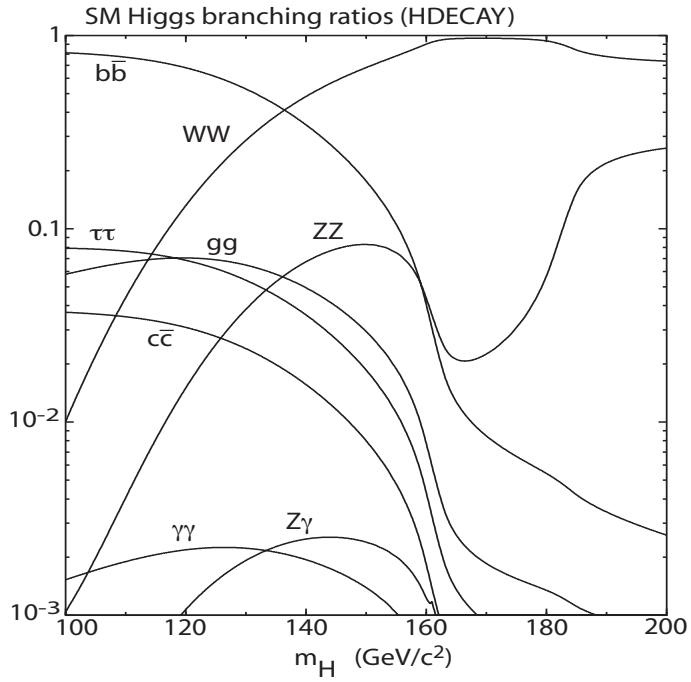

Figure 1.5: The branching ratios of the Higgs boson as a function of masses in the Tevatron search region.

Higgs boson decay into Fermions

In the low mass region, the dominant decay mode of the Higgs boson is fermion pairs. Since the coupling of the Higgs boson to fermions is proportional to the fermion mass, the decay branching ratio to a pair of any fermion $f\bar{f}$ is proportional to m_f^2. The partial width to any fermion pair channel is

$$\Gamma(H \rightarrow f\bar{f}) = \frac{N_c G_F m_f^2 m_h}{4\sqrt{2}\pi}\beta^3 \tag{1.45}$$

where N_c is a color factor, $\beta^2 = 1 - m_f^2/m_h^2$ and G_F is the Fermi coupling constant. According to

this equation, $b\bar{b}$ decay is dominant as shown in Figure 1.5 because the partial width is proportional to the square of the fermion mass. Since β is almost 1 in the search region, the partial width to a fermion pair is almost proportional to the Higgs boson mass,

$$\Gamma(H \to f\bar{f}) \propto m_h \tag{1.46}$$

Higgs boson decay into boson

In the high mass region, the dominant decay is a pair of W^+W^- or Z^0Z^0 bosons. The partial widths of these channel are

$$\Gamma(H \to W^+W^-) = \frac{G_F m_h^3}{8\sqrt{2}\pi}\sqrt{1-x_W}\left(1 - x_W + \frac{3}{4}x_W^2\right) \tag{1.47}$$

$$\Gamma(H \to Z^0Z^0) = \frac{G_F m_h^3}{16\sqrt{2}\pi}\sqrt{1-x_Z}\left(1 - x_Z + \frac{3}{4}x_Z^2\right) \tag{1.48}$$

$$\tag{1.49}$$

where $x_W = 4m_W^2/m_h^2$ and $x_Z = 4m_Z^2/m_h^2$. The two partial widths are almost proportional to the cube of the Higgs bosom mass.

$$\Gamma(H \to VV) \propto m_h^3 \tag{1.50}$$

Figure 1.6 shows the decay width of the Higgs boson obtained from HDECAY. The partial decay width is characterized by dominant decay into a pair of fermion, $\bar{b}b$, $\tau\tau$, $c\bar{c}$ in the low mass region and by dominant decay into a pair of boson, W^+W^-, Z^0Z^0 in the high mass region.

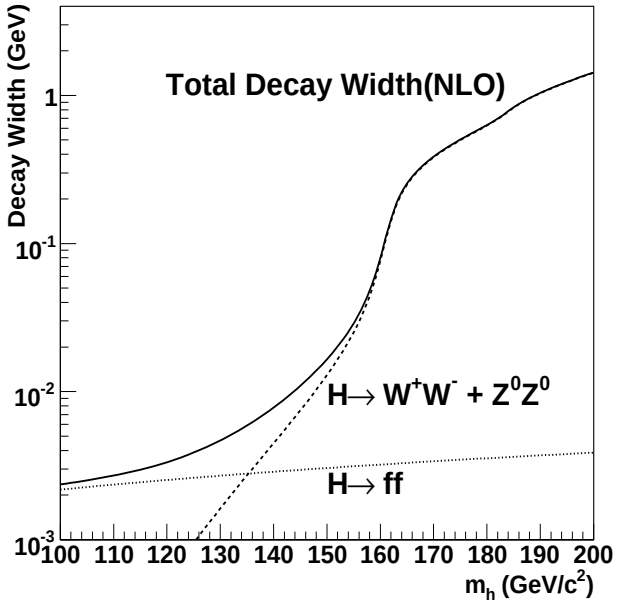

Figure 1.6: The decay width of the Higgs boson calculated from HDECAY in the Tevatron search region.

Higgs boson production

Figure 1.7 shows the Higgs boson production cross section at the Tevatron. The most dominant process is a gluon-gluon fusion process where the Higgs boson is produced via a fermion loop. The Feynman diagram of this process is shown in Figure 1.8. This process is widely used in the high mass Higgs search where the Higgs decay into a W boson pair is dominant. It is not used in the low mass Higgs search, because this production channel has exactly the same final state as the QCD 2jet background which has a high cross section in the low Higgs mass region. For this reason, the channel where the Higgs boson production in association with a W or Z boson is used to search for low mass Higgs though the production cross section is lower. We can make use of a high p_T lepton and a high p_T neutrino from W/Z semileptonic decay to trigger signature this channel and suppress background efficiently.

At the Tevatron, the channel $q\bar{q} \to WH$ is one of the most promising channels. The Higgs boson search in this channel is a subject of this thesis. The production cross section for this channel is

$$\sigma(q_i\bar{q}'_j \to WH) = \frac{\pi\alpha^2|V_{ij}|^2}{35\sin^4\theta_W}\frac{2K}{\sqrt{\hat{s}}}\frac{(K^2+3m_W^2)}{(\hat{s}-m_W^2)^2} \tag{1.51}$$

where $|V_{ij}|$ is one of the Cabibbo-Kobayashi-Maskawa matrix [16, 17] elements associated at the $q_i\bar{q}'_j \to W$ vertex, $\sqrt{\hat{s}}$ is the center of mass energy of the $q_i\bar{q}'_j$, K is the center of mass momentum of the produced Higgs boson. Since this process is most promising for Higgs search, it is important to compute the cross section as accurately as possible with including QCD radiative corrections. The production cross section with higher order QCD corrections is shown in Figure 1.7. To search for W+Higgs events, we first identify a lepton from W leptonic decay. The background is significantly reduced by imposing the isolation cuts around the lepton candidates. The typical production cross section for W+Higgs channel is 0.16 pb for $m_h = 115$ GeV/c^2. Figure 1.9 shows the Feynman diagram of W+Higgs channel.

1.2.3 Review of Previous Higgs Boson Searches

Proof of the Higgs boson existence is one of the most important research in the present elementary particle physics. Therefore many experiments have looked for the evidence of Higgs boson production in the last decades. There are some impressive and motivated results but no experiments have found the evidence of the Higgs boson. We summarize the search results are described below.

Direct Searches at LEP

At Large Electron Positron Collider (LEP) the Higgs boson could be produced mainly in association with the Z boson as $e^+e^- \to HZ$. This $HZ \to b\bar{b}ff$ channel where f means any fermion under search. Though branching ratio is lower, the $HZ \to \tau\tau q\bar{q}$ channel was also looked for. The reconstructed candidate Higgs mass is shown in Figure 1.10. Any significant excess corresponding to the Higgs boson signal was not found. A total of 2461pb^{-1} data collected at a center of mass energies between 189 and 209 GeV was used in this search.

The result of the LEP Electroweak Working Group analysis [18] gives the current lower limit for Higgs boson mass which is $m_h > 114.4\text{GeV}/c^2$ as shown in Figure 1.11

Feedback from Indirect Searches

The existence of the Higgs boson has an impact on many electroweak parameters via higher order loop corrections, and it makes the electroweak theory re-normalizable. The one loop diagrams of top quark and the Higgs boson on the W and Z boson mass propagators are shown in Figure 1.12.

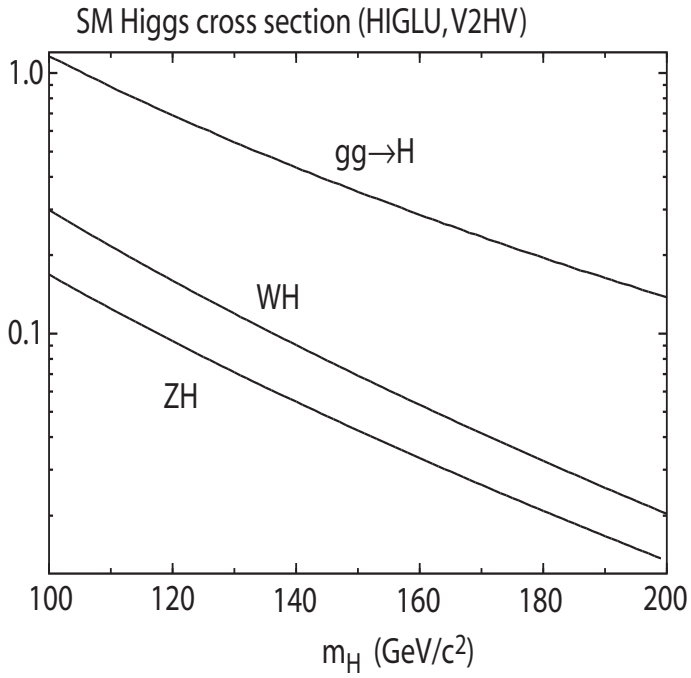

Figure 1.7: The Standard Model Higgs boson production cross section in pb at the Tevatron at a center-of-mass energy 1.96 of TeV.

The parameter ρ relates the W and Z boson masses and the Weinberg angle as follows:

$$\rho = \frac{M_W^2}{M_Z^2}(1 - \sin^2\theta_W) \equiv 1 + \Delta r. \tag{1.52}$$

ρ deviates from unity by radiative corrections Δr which can be expressed in terms of m_t, m_h and m_W. The radiative correction can be written

$$\Delta r = \frac{3G_F}{8\pi^2\sqrt{2}}m_t^2 + \frac{\sqrt{2}G_F}{16\pi^2}m_t^2\left[\frac{11}{3}ln\left(\frac{m_h^2}{m_W^2}\right) + \cdots\right] + \cdots \tag{1.53}$$

One can infer the Higgs boson mass from the precise measurements of the top quark and W boson masses and other Standard Model parameters under the assumption that the Standard Model is the correct theory of nature. The relationship between the masses of the top quark, the W boson and the Higgs boson is shown in Figure 1.13.

Figure 1.14 shows the $\Delta\chi^2$ curve as a function of m_h derived from high precision m_t and m_W measurements [19], performed by LEP, SLD, CDF and D0 and NuTeV. The preferred value for the Higgs boson mass, corresponding to the minimum of the curve, is

$$m_{Higgs} = 76^{+33}_{-24}\ \text{GeV}/c^2$$

The 95% confidence level upper limit estimated from this distribution is

$$m_{Higgs} < 144\ \text{GeV}/c^2$$

The upper limit is shifted to 182 GeV/c^2 if we include the LEP Higgs boson direct search results.

The current allowed region of the Higgs boson mass from these experimental results in 95% confidence level is

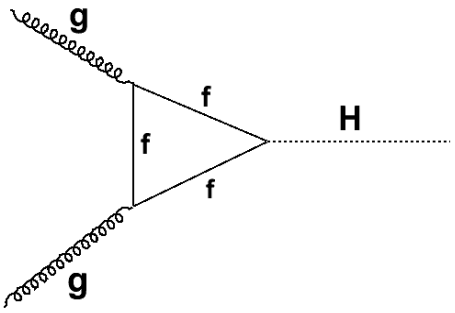

Figure 1.8: The Feynman diagram of Higgs production via gluon-gluon fusion process.

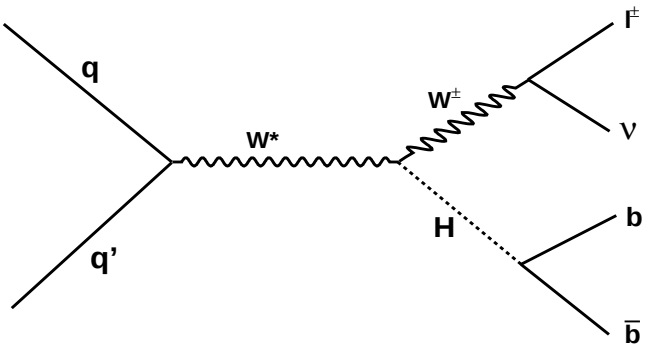

Figure 1.9: Feynman diagram of W+Higgs production.

$$114.4 \text{ GeV}/c^2 < m_{Higgs} < 182 \text{ GeV}/c^2$$

This region corresponds to the most sensitive search region at the Tevatron. We note that the current Standard Model results prefer the low mass Higgs boson.

Former Direct Search at the Tevatron Run II

The Higgs boson search using the $WH \rightarrow l\nu b\bar{b}$ channel was performed in CDF RUN II experiment [20,21]. The previous analysis used the data collected between February 2002 and February 2006, which corresponds to an integrated luminosity of 955 pb^{-1} . The signal events are characterized by one high p_T electron or muon, large missing transverse energy and two high E_T jets in the central region. The jet identified as a b-quark jet is essential for the background reduction. Furthermore, b jet identification (b-tagging) with Neural Network technique is applied to increase the purity of the b-tagging. The dijet mass distributions are shown for different signal purities in Figure 1.15. In the previous analysis the observed distribution is consistent with expected Standard Model background and shows no evidence of Higgs signal.

Figure 1.16 shows the previous upper limit of the production cross section $\sigma(p\bar{p} \rightarrow WH)$ times branching ratio $BR(H \rightarrow b\bar{b})$. The observed upper limit is 20 times higher than the Standard Model expectation. Starting from the previous analysis, we have achieved significant improvements on the event selection, which is applied to about 2 times increased data amount.

Other Higgs search channels have also been studied well. In the previous stage, ZH chan-

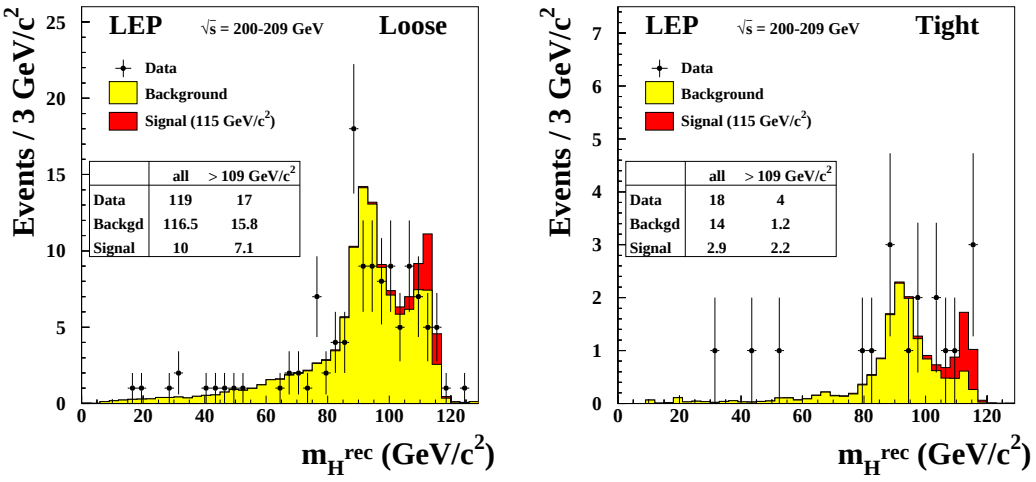

Figure 1.10: Reconstructed candidate Higgs mass distributions for two event categories with different purities.

nel contributed much to the discover sensitivity in the low Higgs mass region in addition to the W+Higgs channel. The Z+Higgs channels included two processes, $ZH \rightarrow \ell\ell b\bar{b}$ [22] and $ZH \rightarrow \nu\nu b\bar{b}$ [23]. $H \rightarrow W^+W^- \rightarrow \ell^+\nu\ell^-\nu$ [24] channel was also searched for the Higgs boson in the high mass region. The summary of CDF results is shown in Figure 1.17. After combining CDF results [25], we did not see any evidence of Higgs boson. Typical cross section times branching ratio is still about 10 times higher than the Standard Model expectation.

Another Tevatron experiment D0 has also searched for Higgs boson [26–31]. Thus the CDF results and D0 results are combined to increase the sensitivity to the Higgs boson search [32]. Figure 1.18 shows the contribution of each channel to the Tevatron combined upper limit. The upper limit on the Higgs boson production cross section was 10 times higher in the low Higgs mass region and 5 times higher in the high Higgs mass region.

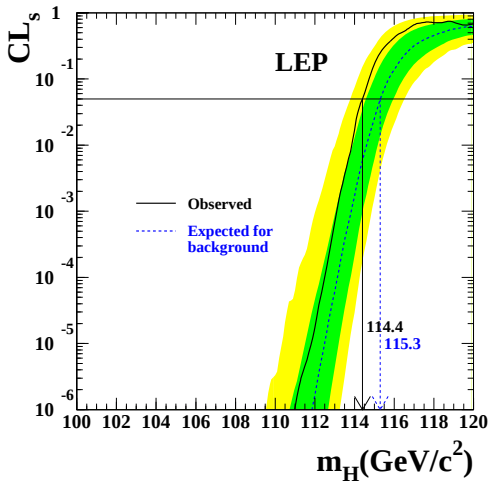

Figure 1.11: The confidence level ratio $CL_s = CL_{s+b}/CL_b$ for the signal plus background hypothesis as a function of the Higgs mass.

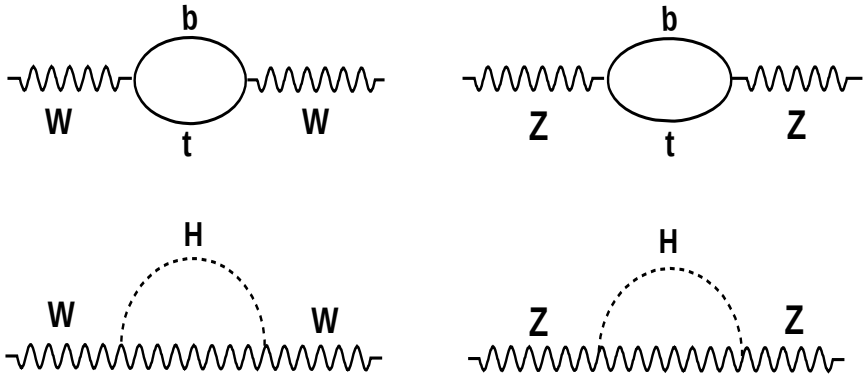

Figure 1.12: The contribution of self-coupling loops to higher order electroweak processes.

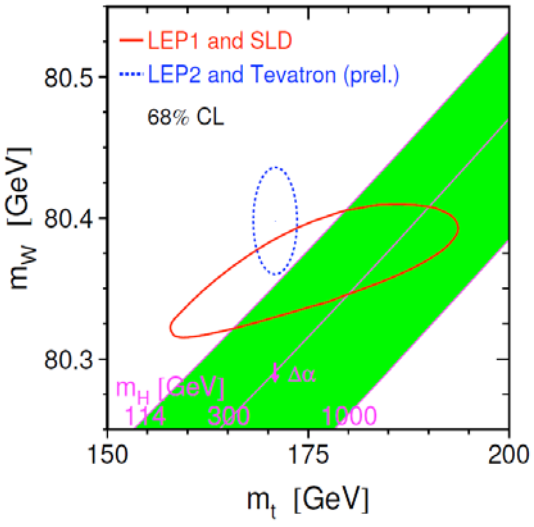

Figure 1.13: The Higgs boson mass predicted from precision m_W and m_t measurements. The dashed circle corresponds to one standard deviation region. The arrow labeled $\Delta\alpha$ shows the variation of the Higgs mass if $\alpha(m_Z^2)$ is changed by one standard deviation. This variation gives an additional uncertainty to the Standard Model band.

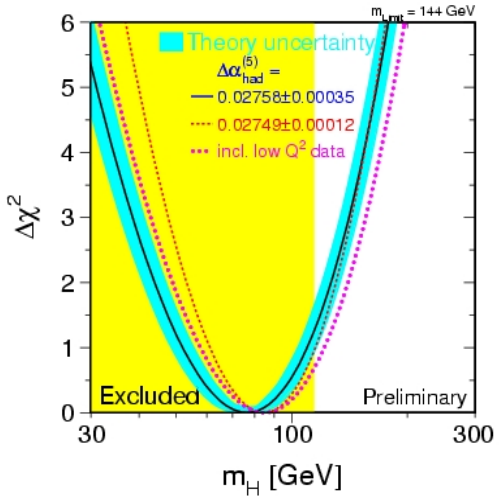

Figure 1.14: The $\Delta\chi^2$ distribution as a function of Higgs boson mass. The electroweak global fit is based on LEP, SLD, CDF, D0 and NuTeV results.

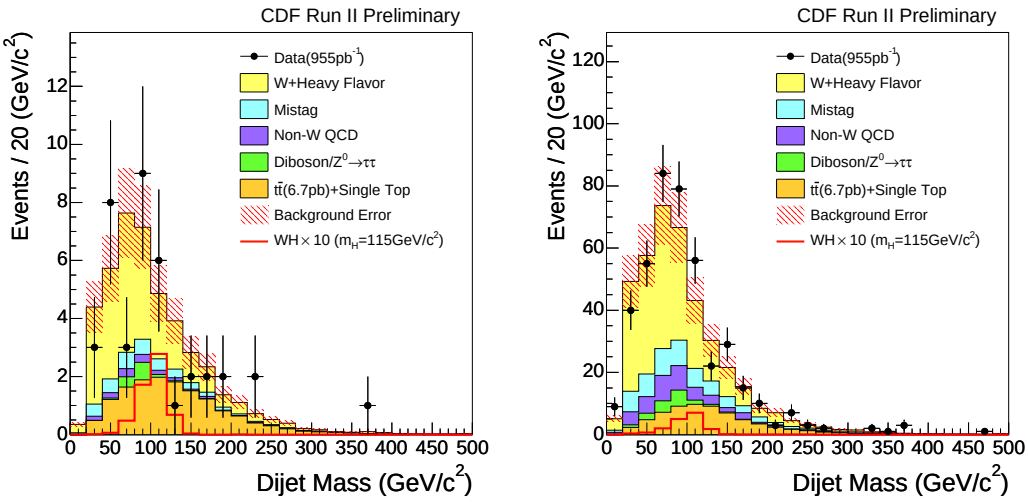

Figure 1.15: Dijet mass distribution for two different event selections. The event selection in the left plot is tighter to achieve higher purity. The different event selection depends on the b jet identification.

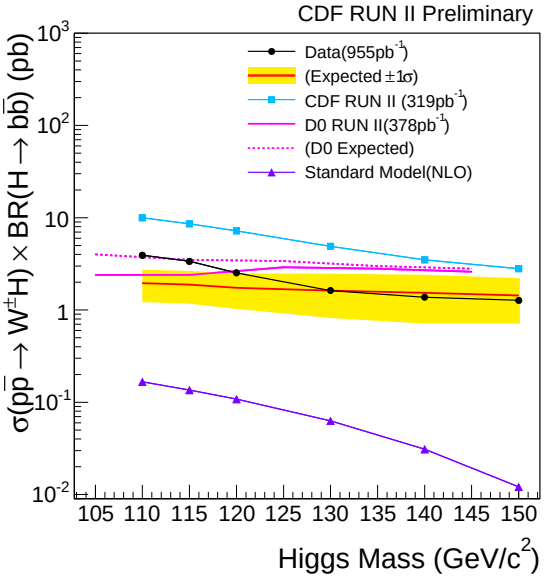

Figure 1.16: Upper limit on $\sigma(p\bar{p} \to WH) \times BR(H \to b\bar{b})$ obtained for an integrated luminosity of 955 pb^{-1}.

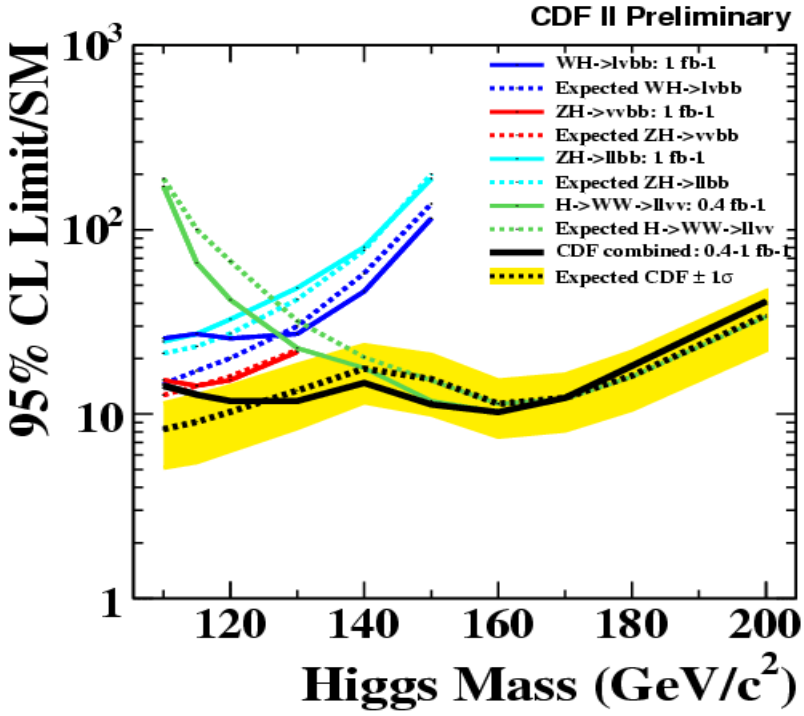

Figure 1.17: The summary of the CDF combined 95% upper limit on the Higgs boson production cross section times branching ratio normalized by the Standard Model expectation. The contributions of various channels are shown in different colors.

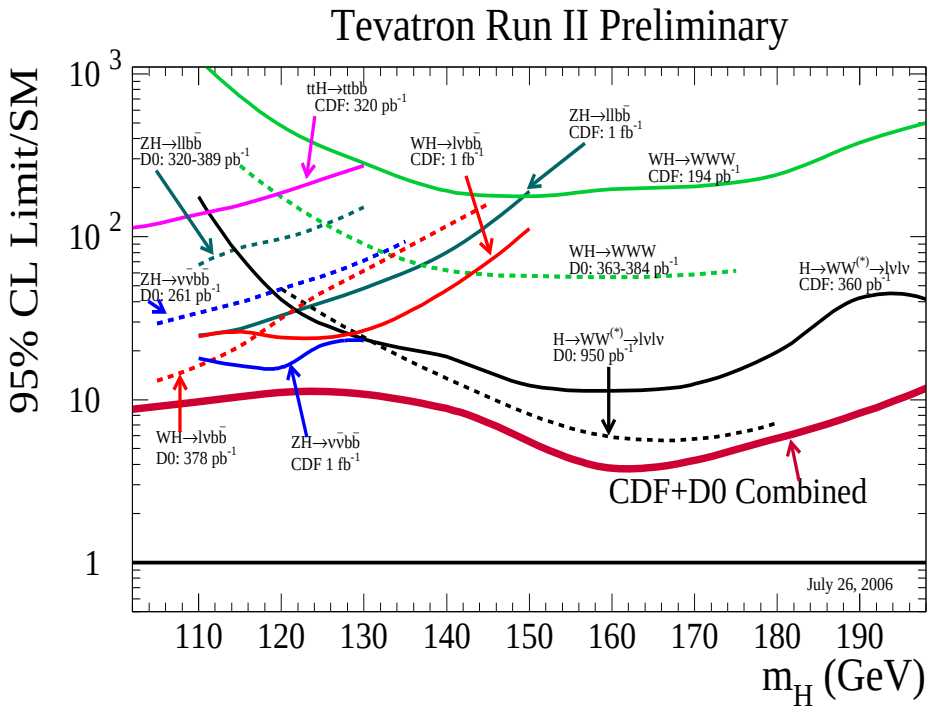

Figure 1.18: The summary of the Tevatron (CDF+D0) combined 95% upper limit on the higgs boson production cross section times branching ratio normalized by the Standard Model expectation. The used dataset is 300 pb^{-1} - 1fb^{-1} depending on channel.

Chapter 2

Experimental Apparatus

2.1 The Tevatron Collider and the Fermilab Accelerator Complex

The Fermilab Tevatron Collider represents the high energy frontier accelerator in particle physics. It is a proton-antiproton storage ring system located at Fermilab in Batavia, Illinois (USA). With a center-of-mas energy of $\sqrt{s}$ = 1.96 TeV it is currently providing highest energy proton-antiproton ($p\bar{p}$) collisions and the only apparatus capable of probing the Higgs boson directly. The collisions occur at two points in a underground ring, which has a radius of about 1km. At these collision points there are two detectors: CDF and D0. The 2 km diameter storage ring is the last step of a complex chain of accelerators that produce and accelerate the proton and antiproton. Each step of this production and acceleration is described in the following section. Figure 2.1 shows the air and schematic views of Fermilab accelerator complex.

2.1.1 Proton Production and Boosting

The Cockcroft-Walton pre-accelerator provides the first stage of acceleration. It consists of a source housed in an electrically charged dome. The source converts hydrogen gas to ionized hydrogen gas (H^-). The dome is charged to a potential of -750 kV. The ionized gas is allowed to accelerate through a column from the charged dome to the grounded wall to an energy of 750 KeV every 66 ms (15 Hz).

After beam exits the accelerating column, it travels through a transfer line called the 750 KeV line and then enters a linear accelerator (Linac). The Linac is approximately 150 m long which is the next level of acceleration for the negatively charged hydrogen ions. It takes the ions with an energy of 750 KeV and accelerates them to an energy of 400 MeV. The acceleration in the Linac is done by a series of "kicks" from Radio Frequency (RF) cavities. The Linac can accelerate beam once every 66 ms (15 Hz).

The 400 MeV negative hydrogen ions from Linac are injected into the Booster. The Booster strips the electrons off, which leaves only the proton. It then accelerates the protons to 8 GeV. The Booster is the first circular synchrotron in the chain of accelerators. It consists of a series of magnets arranged around a 75-meter radius circle with 18 RF cavities interspersed. The Booster also can accelerate beam once every 66 ms.

2.1.2 Main Injector

The Main Injector (MI) is a circular synchrotron seven times the circumference of the Booster and slightly more than half the circumference of the Tevatron. Main Injector has 18 accelerating

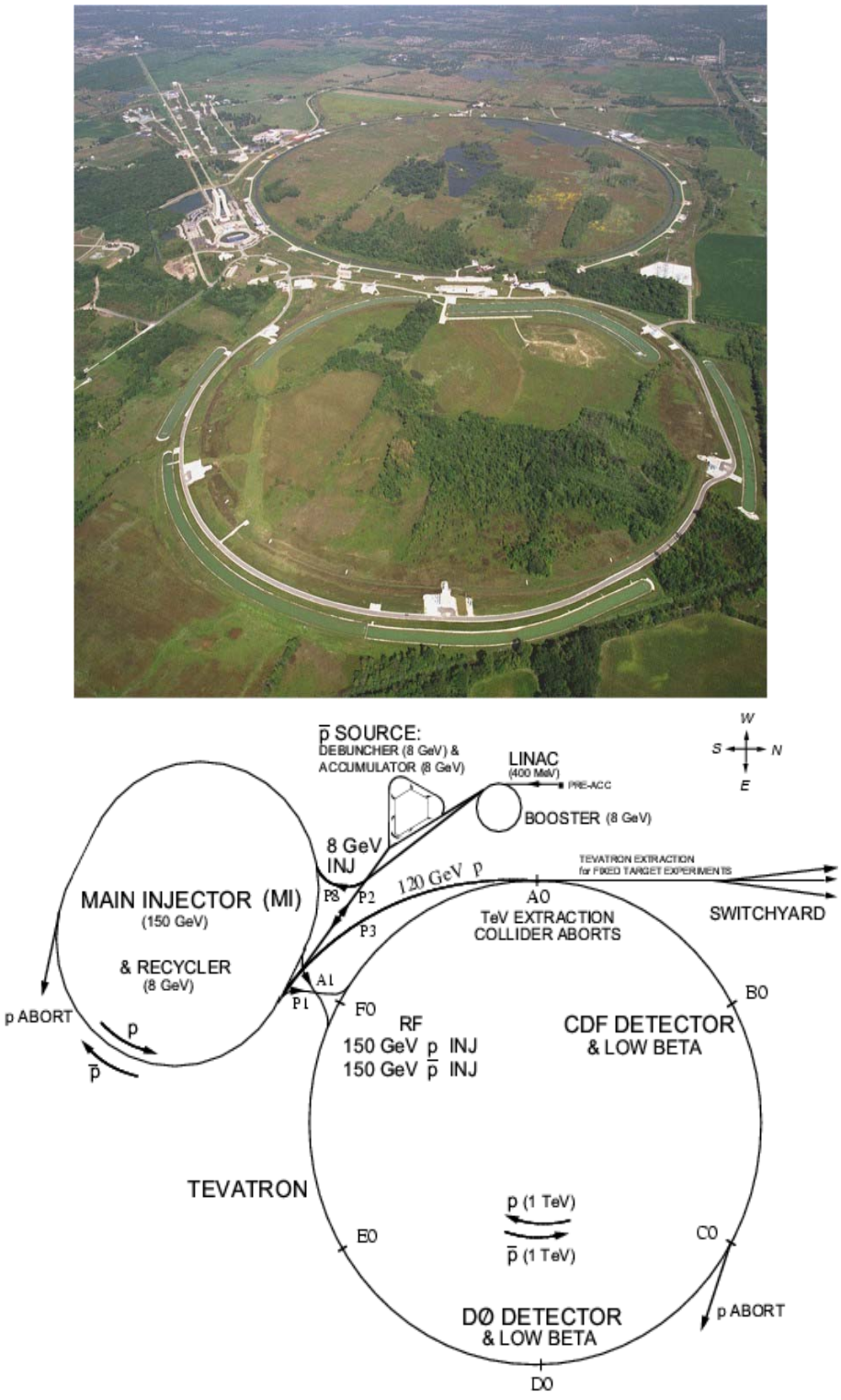

Figure 2.1: Top: Air view of the accelerator. Bottom: Schematic view of the TEVATRON accelerator complex.

RF cavities. It can accelerate 8 GeV protons from the Booster to either 120 GeV or 150 GeV, depending on their destination. When used to stack antiprotons, the final energy is 120 GeV. When used to inject into the Tevatron, the final beam energy is 150 GeV. As well as accepting protons from Booster, the Main Injector can accept antiprotons from the Antiproton Source. The Main Injector can accelerate beam as fast as every 2.2 seconds.

2.1.3 Antiproton Production and Recycler

In order to produce antiprotons, protons at 120 GeV are extracted from the Main Injector and focused into a nickel target. The resulting particle spray contains some antiprotons with a broad momentum distribution, some of which are magnetically selected and transferred to the Debuncher. The Debuncher, a rounded triangular-shaped synchrotron with mean radius of 90 meters, accepts these antiprotons with a broad momentum distributions. It uses a RF manipulation called a bunch rotation to narrow the momentum distribution of the antiprotons at the expense of broadening their time distribution. After the bunch rotation, the antiproton beams is transferred to the Accumulator, a second synchrotron and storage ring in the same tunnel as the Debuncher.

This antiproton production is inherently an inefficient process. Only a small fraction of the protons incident on the nickel target produce antiprotons, and only a fraction of these can be usefully retained in the storage rings. Actually one or two antiprotons are produced for every 10^5 protons incident on the nickel target. The number of antiprotons available for collisions in the Tevatron, and the quality of the beam, is one of the chief limiting factors in the overall Tevatron luminosity and the number of Higgs boson that can be produced. Thus a variety of techniques are used to maximize the available number and quality of antiprotons.

Among these techniques is the stochastic cooling, a real time feedback mechanism where the beam can be characterized at one location and that information is carried across the ring where it can be used to apply corrections to the beam. Along with cooling mechanisms, to maximize the number of antiprotons available for collision it is also helpful to have more than one antiproton storage ring. Therefore, while all antiprotons from the accumulator are transferred to the Main Injector, some are kept at 8 GeV and transferred to the Recycler, while others are accelerated to 150 GeV and transferred to the Tevatron.

The Recycler is another antiproton storage ring located in the same tunnel as the Main Injector. Originally the Recycler was conceived as a means to reuse antiprotons that had already been through colliding beam operations. Currently the Recycler is operated as an antiproton storage ring that receives bunches of antiprotons from the Accumulator and maintains a “stash” of antiprotons. The scheme purpose of this is two-fold. First, it enables the Accumulator to produce antiprotons at higher currents as the stacking rate in the Accumulator is reduced at high antiproton intensities. Second, the overall antiproton accumulation capacity is dramatically increased with the Recycler’s ability to successfully store stack size of more than 400 mA.

2.1.4 Tevatron

The Tevatron is the last stage of Fermilab accelerator chain. It is a circular synchrotron with a 1 km radius. It is composed of eight accelerating cavities, quadrupole and dipole focusing magnets. The Tevatron is cryogenically cooled to 4 K, and the acceleration cavities are made of superconducting materials. It is desirable to use superconducting magnets because the very large fields necessary to maintain TeV-scale energies would require currents so large that it is not affordable for ordinary resistive magnets.

The Tevatron is not a perfect circle. These are six sectors from A to F and each one has

five service buildings (0-4). The "0" sections have large straight sections. The A0 is where the Tevatron tunnel connects to the proton injection point. It also contains one of the two beam aborts. At B0 and D0, the colliding beams are focused into very narrow beam lines of oder 32 μm. C0 is the location of the other beam abort. F0 houses the RF stations which "kick" the beam back into position if it has wandered off its axis. It is also where the transfer lines from the Main Injector connect with the Tevatron. It also houses the transfer line to the antiproton source.

The Tevatron receives 150 GeV protons and antiprotons from the Main Injector or the Recycler and accelerates them to 980 GeV. Since the antiprotons and protons are oppositely charged, they circle in opposite directions in the magnetic field, and are housed in the same ring. The Tevatron can sustain both beams over 1 day at once.

2.1.5 Luminosity

The number of collisions per second is proportioned to the "luminosity", $\mathcal{L}$.

$$\mathcal{L} = \frac{f N_B N_p N_{\bar{p}}}{2\pi(\sigma_p^2 + \sigma_{\bar{p}}^2)} F\left(\frac{\sigma_l}{\beta^*}\right)$$

where f is the revolution frequency in Hz, N_B is the number of bunches, $N_{p(\bar{p})}$ is the number of protons (antiprotons) per bunch, and $\sigma_{p(\bar{p})}$ is the RMS of proton (antiproton) RMS beam size at the interaction point. This is multiplied by a form factor, F, that depends on the ratio of the RMS bunch length, σ_l, and the beta function at the interaction point, β^*, the beta function is a measure of the transverse beam width and is proportional to the beam's x and y extent in phase space. Table 2.1 shows the current parameters of the accelerator.

During a collider store, instantaneous luminosity slowly decreases. In the early stage of the store, the most important cause for this decrease is intra-beam scattering, the depletion of antiprotons during collisions becomes more relevant. Actually above equation is not used for luminosity calculation The measurement of the luminosity delivered by the Tevatron to the CDF experiment is described in the following section. Figure 2.2 shows initial instantaneous luminosity and integrated luminosity. Currant peak luminosity is $\sim 3 \times 10^{32}$ cm^{-2}s^{-1}. Delivered luminosity from Tevatron is more than 3.5fb^{-1} and actual recorded luminosity is more than 2.5 fb^{-1} . It is collected between February 2002 and January 2008. The integrated luminosity used in this analysis is about 1.9 fb^{-1} up to May 2007 after requiring that the detector is operating properly.

Parameter	Run II
Number of bunches (N_B)	36
Protons/bunch (N_p)	2.7×10^{11}
Antiprotons/bunch ($N_{\bar{p}}$)	3.0×10^{10}
Total antiprotons	1.1×10^{12}
β^* [cm]	35
Bunch length [m]	0.37
Bunch spacing [ns]	396
Interactions/crossing	2.3

Table 2.1: Accelerator parameters for Run II configuration.

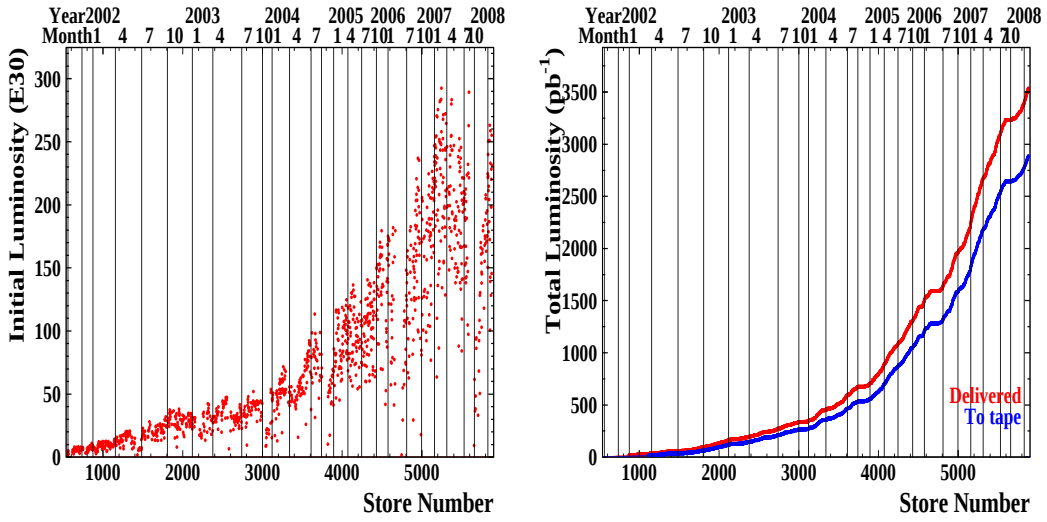

Figure 2.2: Left: CDF initial instantaneous luminosity for each store. The initial luminosity has greatly increased as the accelerator has been upgraded. Right: integrated luminosity as a function of store number. Currently delivered luminosity is over 3.5 fb^{-1} and recorded on tape is over 2.5 fb^{-1} .

2.2 The Collider Detector at Fermilab

The CDF Run II detector, in operation since 2001, is an azimuthally and forward-backward symmetric apparatus designed to study $p\bar{p}$ collisions at the Tevatron. It is a general purpose solenoidal detector which combines precision charged particle tracking with fast projective calorimetry and fine grained muon detection. The detector is shown in a schematic view in Figure 2.3. It is composed of several detectors which play a role in the detection of the particles and the measurement of the physical quantities. The main features of these sub-detectors are described in the following section. The overview of sub-detector is described here.

The inner detector is composed of the Silicon Vertex Detector and the Central Outer Tracker (COT) that surrounds the silicon detector inside a 1.4 T superconducting solenoid magnet. These systems form a tracking system to measure precise trajectories and momenta of charged particles and reconstruct primary and secondary vertices. Figure 2.5 shows the cutaway of tracking system. Segmented electromagnetic and hadronic sampling calorimeters surround the tracking system and measure the energy flow of interacting particles. The muon system resides beyond the calorimetry and detects muons that escape the calorimeters. The beam luminosity is determined by using Cerenkov counters located near beam. A Time Of Flight (TOF) detector located outside the COT. In this thesis, TOF is not used.

2.2.1 The CDF Coordinate System

The following coordinates are used in CDF. We use a standard right-handed coordinate system. Z-axis is defined along the colliding beams as the proton moves in the positive z-direction. The x-axis and y-axis point toward the outside of the Tevatron ring and vertically upward, respectively. It is convenient to work in cylindrical (r, z, ϕ) or polar (r, θ, ϕ) coordinates, where the azimuthal angle ϕ is x-y plane angle around the beam line. It is coordinated from the direction of x-axis and the polar angle θ is measured starting from the z-axis. The polar angle θ is often replaced by

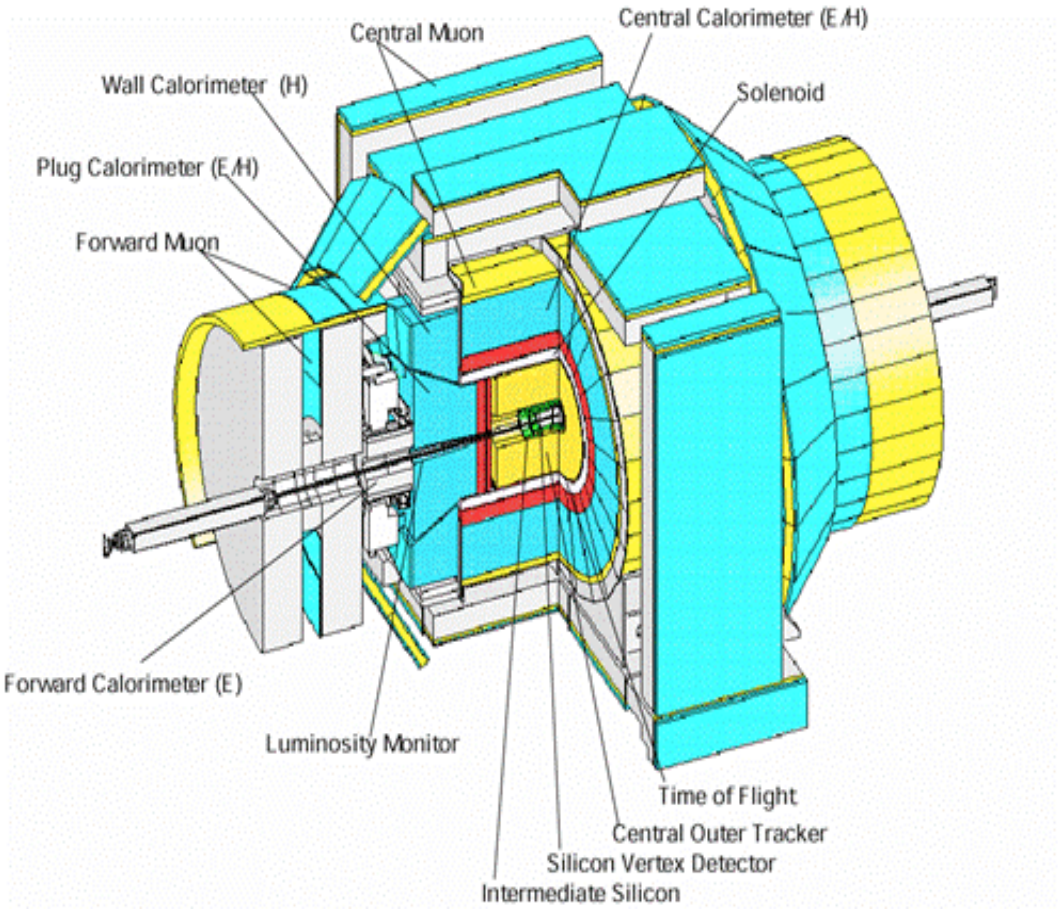

Figure 2.3: Schematic view of CDF Run II detector.

pseudo-rapidity:

$$\eta = -\ln\left(\tan\frac{\theta}{2}\right) \tag{2.1}$$

This pseudo-rapidity is explained as the relativistic or mass less particle approximation of real rapidity

$$y = \frac{1}{2}\ln\left(\frac{E+p_z}{E-p_z}\right) \tag{2.2}$$

At the high energy limit, E $\sim$ p and $p_z = p\cos\theta$, pseudo-rapidity is same as real rapidity.

In hadron-hadron collisions, momentum vector is usually expressed in terms of transverse momentum, pseudo-rapidity and azimuthal angle. The invariant cross section is whiten as

$$E\frac{d^3\sigma}{d^3p} = \frac{d^3\sigma}{d\phi dy p_T dp_T} = \frac{d^3\sigma}{\pi dy dp_T^2} \tag{2.3}$$

The second form is obtained using the identity $dy/p_z = 1/E$, and the third form represents the average over ϕ. The multiplicity of particles in collisions is given by dN/dy and this means that the multiplicity is flat in η.

Many detector components are segmented uniformly in η and ϕ.

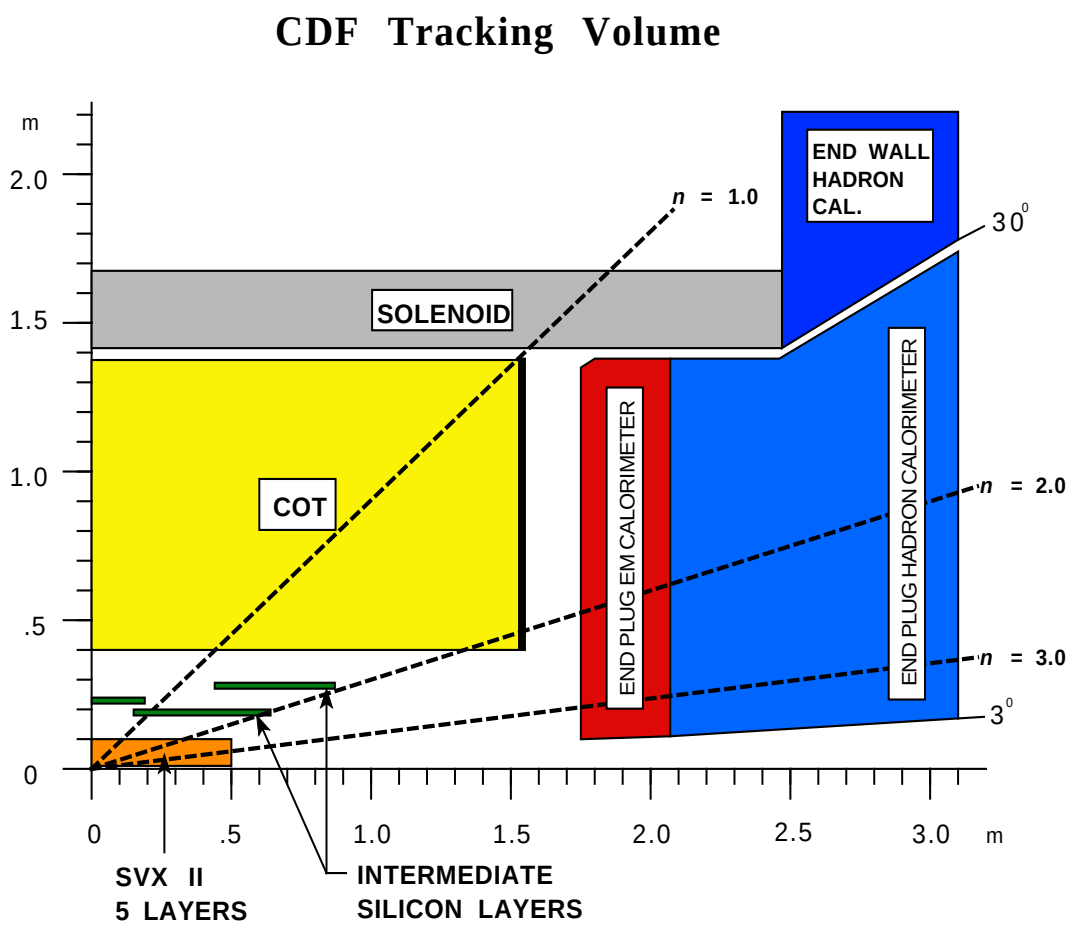

Figure 2.4: Tracking system and endplug calorimetry of the CDF detector.

2.2.2 Tracking System

The detector has a cylindrical tracking system surrounded in a 1.4 T solenoidal magnetic field for measurement of charged-particle momenta. This tracking system consists of three silicon micro strip vertex detector: Layer 00 (L00), the Silicon Vertex Detector (SVX-II), and the Intermediate Silicon Layers (ISL), and Central Outer Tracker (COT), a 3.1 m-long cylindrical open-cell drift chamber covering radii from 43.4 to 132.3 cm. In the following section, details are described.

2.2.3 The Silicon Vertex Detector

The Silicon tracking detectors are used to obtain precise positions of the charged particle path and provide excellent impact parameter, azimuthal angle and z. Figure 2.5 shows the transverse and vertical view of the Silicon Vertex Detector.

The SVX-II located outside of L00 consists of five concentric layers of double-sided silicon sensors. One side of each sensor measures r-ϕ position with axial microstrips; the other side provides z position information with stereo angle strips. SVX-II extends radially from 2.1 to 17.3 cm, and along z up to 45 cm on either side of the interaction point. The detector coverage is $|\eta| < 2.0$ as shown in Figure 2.5. The typical spacial resolution of the SVX-II is ~ 20 μm.

The ISL is located outside of SVX-II consisting of double-side silicon sensor similar to those

for SVX-II [36]. One layer is placed at a radius of 22 cm in the central region ($|\eta| < 1.0$), and two forward layers ($1 < |\eta| < 2$) at radii 20 and 28 cm from the beam line. The ISL together with SVX-II makes it possible to reconstruct tracks in the forward region where COT tracking efficiency is degraded (see Figure 2.5).

The L00 is the most recent addition to the CDF II tracker. It is a radiation-hard, single-sided silicon detector installed directly onto the beryllium vacuum beam pipe, placed at radii between 1.35 and 1.62 cm from the beam center. Being so close to the interaction, L00 improves noticeably the impact point with a special resolution of 15 μm.

The coverage of the silicon detector subsystem is $|\eta| < 2.8$ where silicon stand-alone tracking is possible. However in CDF, tracking in the region, $|\eta| < 2.0$, covered with both COT and silicon detector is well studied.

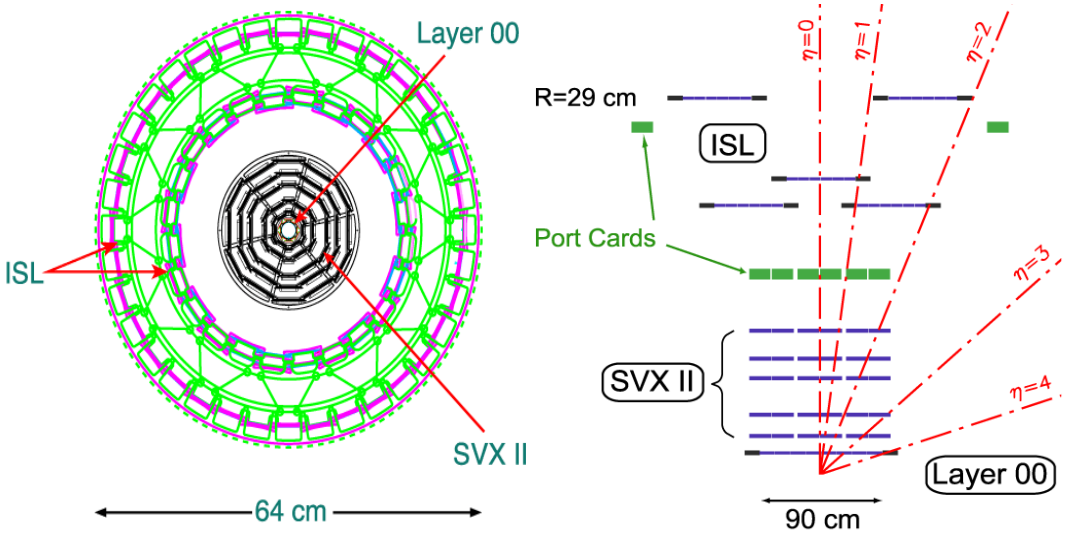

Figure 2.5: Left:CDF silicon detector in r-ϕ plane. Right: in r-z plane.

2.2.4 The Central Outer Tracker

The COT is a multi-wire drift chamber and covers a radial span beginning at 40 cm and ending 137cm. The chamber is 310 cm long. The COT contains 96 sense wire layers, which are radially grouped into eight "superlayers", as inferred from the end plate section shown in Figure 2.7. Four superlayers which works as axial superlayers provide accurate measurement in $r - \phi$, while remaining four layers provide 3° stereo measurements. Particles originating from the interaction point and having $|\eta| < 1.0$. They pass through all 8 superlayers of the COT, and those having $|\eta| < 1.3$ pass through 4 or more superlayers.

The supercell layout is shown in Figure 2.6 for superlayer 2. It consists of a wire plane containing sense, potential and shaper wires and a field sheet on either side. Both the sense and potential wires are 40 μm diameter gold plated Tungsten. The field sheet is 6.35μm thick Mylar with vapor-deposited gold on both sides. Each field sheet is shared with the neighboring supercell. Each cell is tilted by 35° with respect to the radial direction.

A mixture gas (∼50:∼50 Argon-Ethane) is filled in COT. It is chosen to have a constant drift velocity across the cell width. This allows a maximum drift time of 177 ns. This prevents pile up of events from the previous interactions. O_2 and Isopropyl alcohol are also filled at very

small portions. O_2 is added to prevent the growth of wrong hydrocarbon creation on the sense wires. Isopropyl alcohol is added to prevent the growth of SiO2 on the sense wires and acts as a "quencher" to prevent glow discharge.

The COT provides accurate position information in $r-\phi$ plane giving superior measurement of transverse momentum, p_T , and substantially less accurate information in the $r-z$ plane for the measurement of the z component of the momentum, p_z. The hit position resolution of COT is about 140 μm. The transverse momentum resolution has

$$\frac{\sigma_{p_T}}{p_T^2} = 0.0015[\text{GeV/c}]^{-1} \tag{2.4}$$

More details of COT performance are described in [35].

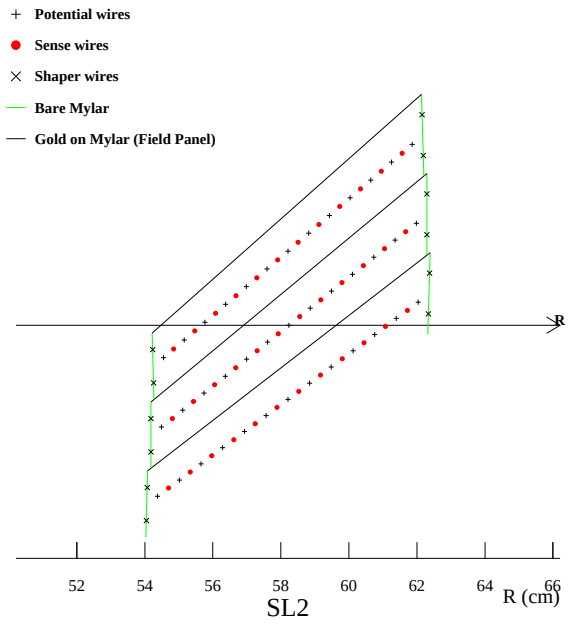

Figure 2.6: Nominal cell layout for Super Layer 2 (SL2).

2.2.5 The Solenoid

The CDF superconducting solenoid provides nearly uniform magnetic field of 1.4 T along the beam line. It has a cylindrical fiducial volume 3.5 m long and 2.8 m in diameter. The coil itself is 4.8 m long and 25 cm thick. This solenoid is built of an Al-stabilized NbTi superconductor. It is able to withstand currents up to 5000 A operated at liquid helium temperature. Usually the magnet is operated at 4650 A, corresponding to a current density of 1115 A/m.

2.2.6 The Calorimetry

The CDF calorimeters are based on scintillator sampling. It is sandwich construction of absorbing material and scintillator. The light produced by incoming particles are guided to photomultipliers

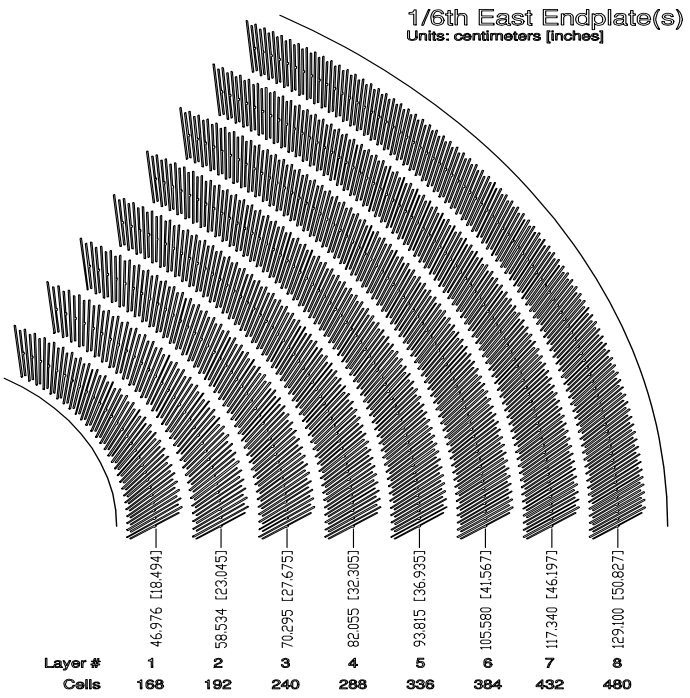

Figure 2.7: 1/6th view of COT East end-plate.

via wavelength shifting fibers or shifting bars. The calorimeter consists of two sections, electromagnetic (large thick in radiation lengths X_0 with fiber sampling for photon and electron identification and energy measurement) and hadronic (large thick in interaction lengths λ for hadron energy measurement).

The calorimeter system is mechanically divided in some regions depending on η. The central region is covered by Central ElectroMagnetic (CEM) and Central Hadronic (CHA) calorimeters in $|\eta| < 1.1$ and $|\eta| < 0.9$, respectively. The plug region is covered by Plug ElectroMagnetic (PEM) and Plug HAdronic (PHA) calorimeters in $1.1 < |\eta| < 3.6$ and $1.3 < |\eta| < 3.6$, respectively. To fill the gap between CHA and PHA, there is the Wall HAdronic Calorimeter (WHA) in $0.7 < |\eta| < 1.3$ region. Table 2.2 shows calorimeter segmentation in each region. This calorimetry covers almost all 4π region. This is important to measure transverse energy component of neutrinos by looking for the imbalance in the event transverse energy. The detail of each calorimeter is described below.

η range	$\Delta\phi$	$\Delta\eta$
0 - 1.1 (1.2 for Had)	15°	0.1
1.1 (1.2 for Had)	7.5°	0.1
1.8 - 2.1	7.5°	0.16
2.1 - 3.6	15°	0.2-0.6

Table 2.2: The calorimeter segmentation in each η region.

The CEM is a sampling device made of 5 mm thick layers of polystyrene scintillator, alternated with 3.18 mm thick layers of Al-clad lead. In order to maintain a constant number of radiation

lengths as a function of θ, some lead layers are replaced by acrylic (Plexiglass), so that the actual number of absorber layers varies from 30 near the center to 20 at $\eta \sim 1.1$. The CEM is divided into four arches (North-West, South-West, North-East, South-East) made of identical 15° modules, each of them being segmented into 10 projective towers in η (The two most forward towers of one of the CEM and CHA modules are not instrumented, in order to provide access for cryogenics to the solenoid.), thus each tower covers 0.1 by 15° in $\eta \times \phi$ space. The blue light emitted by the scintillators is collected on each side of the tower by acrylic wavelength shifters that convert it into green light and guide the light toward two photomultiplier tubes (PMT's Hamamatsu R580) outside the CHA. Figure 2.8 shows the wedge of CEM. The CEM energy resolution for an electron going through the center of a tower is found to be

$$\frac{\sigma_E}{E} = \frac{13.5\%}{\sqrt{E(\text{GeV})}} \oplus 2\%$$

where $\oplus$ symbol means that the constant term is added in quadrature to the resolution.

The central electron strip chamber (CES) is used to determine shower position and transverse shower development. They are located between the 8th lead layer and the 9th scintillator layer, which is the expected position of shower maximum ($\sim 6X_0$ including tracking and solenoid material). In each CEM module, a CES module is a multi-wire proportional chamber with 64 anode wires parallel to the beam axis, spaced 0.73 cm apart and split at $|z| = 121$ cm. The spatial resolution achieved is ~ 2 mm.

The CEM is also equipped with a pre-shower detector (CPR). useful in discriminating between hadrons and photons/electrons. The CPR is a set of multi-wire proportional chambers with wires parallel to the beam providing transverse measurements and strip cathodes providing z information, with a resolution of the order of a few millimeters.

The CHA is a sampling hadronic calorimeter surrounding the CEM, following the same segmentation (0.1 by 15° in $\eta \times \phi$ space). The WHA extends the CHA coverage using the same technology as the CHA. Altogether a wedge contains 12 towers, 6 of which are fully in the CHA, 3 in the WHA and 3 are shared between the two. The number of interaction lengths is constant through the entire range of η being equal to 4.5. The CHA is made of 32 layers of 2.5 cm thick steel absorber and 1.0 cm thick scintillator. The WHA is made of 15 layers of 5.0 cm thick steel absorber and 1.0 cm thick scintillator. Two PMT's per tower are linked to the scintillators by a wavelength shifter and a light guide. Some regions have low calorimetry response (called "crack") at the junction between East and West modules near η = 0 and around the "chimney" for the cryostat near the azimuthal boundaries. The CHA and WHA energy resolution are, respectively,

$$\frac{\sigma_E}{E} = \frac{50.0\%}{\sqrt{E(\text{GeV})}} \oplus 3\%$$

and

$$\frac{\sigma_E}{E} = \frac{75.0\%}{\sqrt{E(\text{GeV})}} \oplus 4\%$$

.

The plug calorimeter covers the η region between 1.1 and 3.6, corresponding to polar angles between 3° and 30 ° as shown in Figure 2.9. It was designed and built to replace CDF I calorimeters to cope with the Run II requirements.

The Plug Calorimeter consists of PEM and PHA calorimeter with the same projection segmentation. The calorimeter is divided in 12 concentric η regions, which are further azimuthally segmented in 48 in $\eta < 2.11$ and 24 in $\eta > 2.11$.

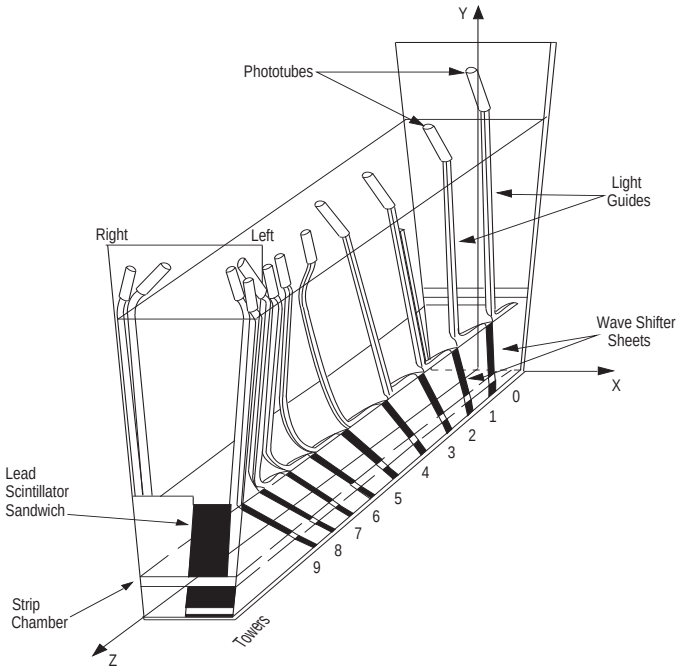

Figure 2.8: A isometric view of wedge of the Central Electromagnetic Calorimeter.

System	Region	Energy resolution (%)	Thickness	Absorber
CEM	$\|\eta\| < 1.1$	$13.5/\sqrt{E_T} \oplus 2$	18 X_0	3.18 mm lead
PEM	$1.1 < \|\eta\| < 3.6$	$16.0/\sqrt{E_T} \oplus 1$	21 X_0	4.5 mm lead
CHA	$\|\eta\| < 0.9$	$50.0/\sqrt{E_T} \oplus 3$	4.5 λ	2.5 cm iron
WHA	$0.7 < \|\eta\| < 1.3$	$75.0/\sqrt{E_T} \oplus 4$	4.5 λ	5.0 cm iron
PHA	$1.3 < \|\eta\| < 3.6$	$80.0/\sqrt{E_T} \oplus 5$	7.0 λ	5.08 cm iron

Table 2.3: The calorimeter properties.

The PEM is made of 22 layers of 4.5 mm lead and 4 mm thick scintillator tiles. The scintillator tiles in a tower are read by a single PMT. In front of the 22 sampling layers is a 1 cm thick scintillator tile read out by a multi-anode photomultiplier (MAPMT), which is used as a pre-shower detector. The PEM energy resolution is

$$\frac{\sigma_E}{E} = \frac{16.0\%}{\sqrt{E(\text{GeV})}} \oplus 1\%$$

The plug shower maximum detector (PES) is made of two sets scintillation strips that provide precise two dimensional shower position measurement (resolution $\sim$ 1 mm). The PHA is made of 23 layers of 5.08 cm thick steel absorber and 6mm thick scintillator. Its resolution is

$$\frac{\sigma_E}{E} = \frac{80.0\%}{\sqrt{E(\text{GeV})}} \oplus 5\%$$

In Table 2.3, the calorimeter property is summarized.

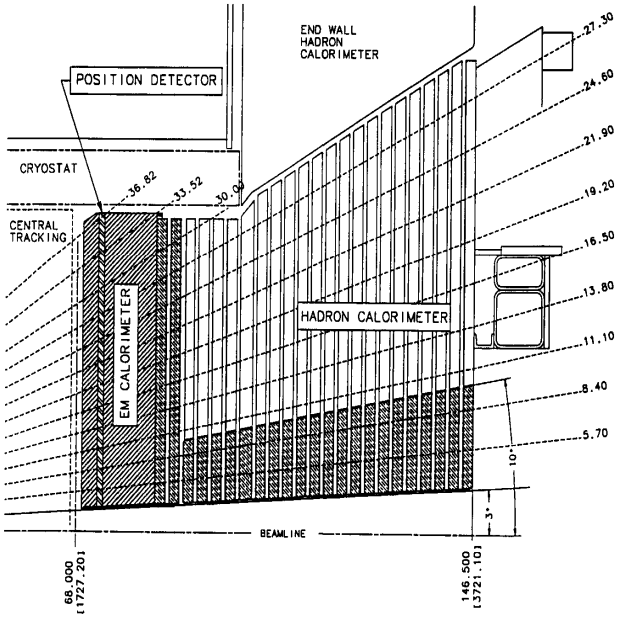

Figure 2.9: Cross section of the Plug calorimeter (PEM and PHA).

2.2.7 The Muon System

Muons are particles which mainly interact with matter by ionization. For energies relevant to this experiment, they do not cause showers in the electromagnetic or hadronic calorimeters. As a result, if a muon is created in the collision and has enough momentum, it will pass through the calorimeter with minimal interaction with the calorimeter material. Therefore, the calorimeter can be considered as a filter for muons which absorbs particles that develop a shower when interacting with matter. Muon detection system is placed radially outside the calorimeters.

The muon system consists of some subsystems that cover specific η, ϕ regions. The muon detector is composed of single wire drift chambers and scintillation counters for fast timing. The subsystems of drift chambers are named the Central MUon (CMU), the Central Muon uPgrage (CMP), the Central Muon eXtension (CMX) and the Barrel Muon Upgrade (BMU). For scintillator, the subsystems are named the Central Scintillator uPgrade (CSP), the Central Scintillator eXtension (CSX), the Toroid Scintillator Upgrade (TSU), the Barrel Scintillator Upgrade (BSU). In this analysis, CMU, CMP and CMX detectors are used for muon detection and TSU, BMU and BSU subsystems are not available.

The CMU is located outside the CHA and made up of muon drift cells with seven wires. It has the same segmentation as the CHA in ϕ. However, there is a 2.5° gap between the drift cell arrays leading to an overall ϕ coverage of 84%. Each wedge is further segmented in r-ϕ plane into three 4.2° modules. Each module consists of four layers of four rectangular drift cells. The smallest unit in the CMU, called a "stack", covers about 1.2° and includes four drift cells, one from each layer. Using the timing information from the drift cells, track segments are reconstructed. A second set of muon drift chambers, called the CMP, is located behind an additional 60 cm of absorber steeel (3.5 pion interaction lengths). The chamers are 640 cm long and arranged axially to form a box around the central detector. CMP are comprised of rectangular (2.5 cm $\times$ 15 cm), single wire drift

chambers configured in four layers with alternate half-cell staggering. The muon which registers a stub in both the CMU and CMP is called CMUP muon, which is considered the purest type of muons at CDF.

The CMX detector is composed of conical section drift chambers and scintillation counters, Each 15° wedge is made up to eight layers of drift chambers with six chambers in each layer. The CMX drift chamber has the same rectangular cross section as the CMP drift chamber. However, the detector arrangement of CMX chambers is unique due to detector geometry. In CMX detector, top two wedges in the west side are called keystone and bottom 6 wedges are called miniskirt from their shape. Table 2.4 shows the properties of the muon subsystem. Figure 2.10 and 2.11 show muon coverage and location of special detector in CMX region.

Muon subsystem	CMU	CMP/CSP	CMX/CSX	BMU/BSU
Coverage	$\|\eta\| < 0.6$	$\|\eta\| < 0.6$	$0.6 < \|\eta\| < 1.0$	$1.0\|\eta\| < 1.5$
p_T threshold [GeV]	1.4	2.2	1.4	1.4-2.0
λ	5.5	7.8	6.2	6.2-20
		Drift chamber		
Thickness [cm]	2.68	2.5	2.5	2.5
Width [cm]	6.35	15	15	8.4
Length [cm]	226	640	180	363
Max drift time [μs]	0.8	1.4	1.4	0.8
Number of chambers	2304	1076	2208	1728
		Scintillator		
Thickness [cm]	N/A	2.5	1.5	2.5
Width [cm]	N/A	30	30-40	17
Length [cm]	N/A	320	180	256

Table 2.4: The muon detector properties.

2.2.8 Luminosity Counter

The beam luminosity is determined by using gas Cerenkov Luminosity Counters (CLC) [37, 38] located in the $3.7 < |\eta| < 4.7$ region. The detector, located in the 3° gap between the plug calorimeter and the beam pipe as shown in Figure 2.12 is made of two identical CLC modules, (see Figure 2.13). They are installed inside Plug calorimeter, on each side of the interaction point. Each module is composed of 48 thin, long, conical gaseous Cerenkov counters. An empty bunch crossing is observed if there are fewer than two counters with signal above threshold in either module. As the number of $p\bar{p}$ interactions in a bunch crossing follows Poisson statistics the luminosity is determined by the inelastic cross section ($\sigma_{in} \sim 60$ mb) and the measured fraction of empty bunch crossings. The systematic error on the luminosity is estimated to be 6% with major contributions from the CLC acceptance precision evaluated with of the detector simulation and the event generator (4.4%) and the calculation of the inelastic cross section.

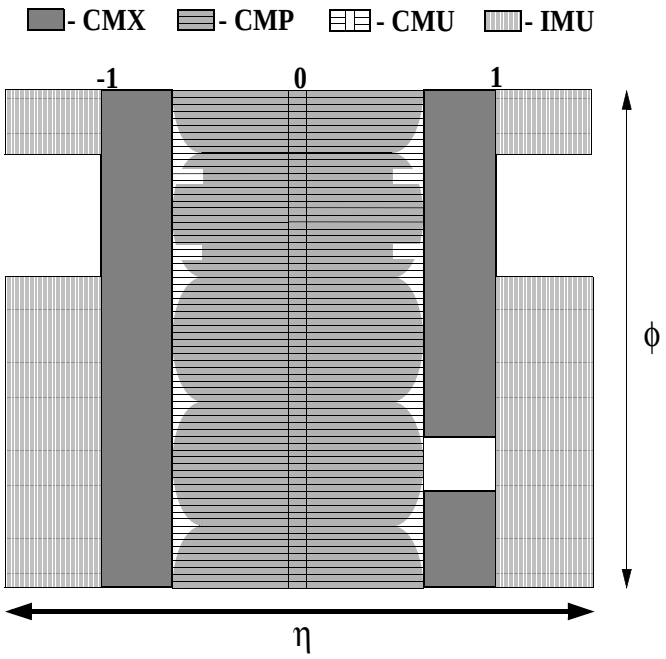

Figure 2.10: CDF Run II muon system coverage in η-ϕ plane.

2.3 Data Acquisition and Trigger

2.3.1 The Trigger System

A trigger system at CDF is necessary because it is not possible to store all collision data. Actually a collision happens roughly at a rate of 1.7 MHz and the readout of the full detector produces an event size of 200 KB. Therefore it is not practical to record data fast enough and analyze all data later. The trigger system is thus a pre-filter, which reduces the data rates and volumes to a manageable level. Figure 2.14 shows the trigger schematic design.

The CDF trigger system consists of separate three levels. Data is accepted or discarded in each level, reducing the event rate such that it can be handled by the next level. It means that a trigger has more restrictive selection criteria as advancing to the next level. To make a decision for every single event before the event information is lost, it is necessary to be fast and operate dead-timeless. In order to decide accepting or rejection in time, the Level 1 and Level 2 triggers are based on hardware with custom electronics. While the Level 3 trigger is implemented as a software trigger using a PC farm with more than 500 CPU's to decide event more specifically.

At Level 1, the event occurring at the Tevatron crossing rate, 396 ns, is moved up one slot in the pipeline. By the time it reached the end of the pipeline, the trigger must reaches a decision whether to accept or reject this event. If the event is accepted, its information will be sent to the higher level of trigger. Figure 2.15 shows the trigger path from the Level 1 trigger to the Level 2 trigger. Level 1 trigger operates to find physics objects based on a subset of the detector information that includes charged tracks, calorimeter and muon information. Track reconstruction is done by eXtremely Fast Tracker (XFT) [39]. The track found by the XFT is passed to the Extrapolation System (XTRP) which processes and distributes the tracking information to other trigger elements. Tracks are matched with calorimeter clusters to identify electrons and with stubs

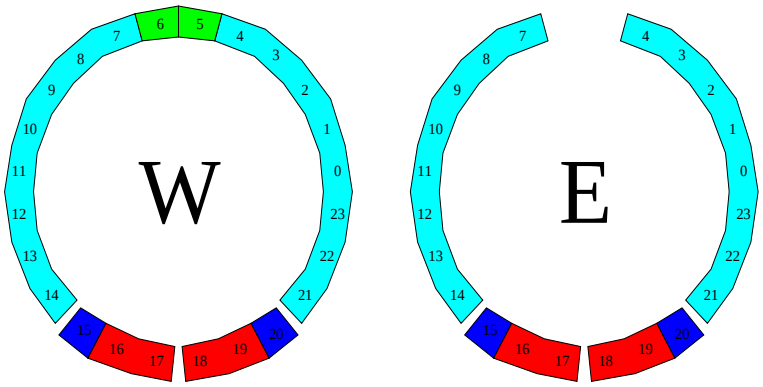

Figure 2.11: CMX wedge layout in r-ϕ plane. 5th and 6th wedges in the west side are called keystone and 15-20th wedges are called miniskirt. On the east side, top two wedges are missing due to space for the cryogenic utilities for the solenoid.

found in the muon detectors to identify muons. Finally Level 1 trigger accept rate is less than 50 kHz: average rate of the order of 25 kHz is common.

The Level 2 trigger also operates with hardware and reduces $\sim$ 25 kHz from L1 accepted rate $\sim$ 500 Hz. At level 2, the information from the silicon detector and the calorimeter shower maximum detectors is available. The information from shower maximum detector (CES) improves the electron identification. it is incorporated in order to perform the precise matching between the electron track and the calorimeter cluster. This matching drastically reduces the electron fake rate.

The Level 3 trigger is performed using software [40]. Every CPU in the farm provides a processing slot for one event. With roughly 500 CPU's an input rate of roughly 500 Hz is coming, allocating approximately 1 second for event reconstruction before reaching trigger decision. The Level 3 selection criteria is somehow complicated. With additional information and improved resolution provided by the full event reconstruction, the Level 3 confirmation of the Level 1 and Level 2 selection quantities significantly reduces background. Level 3 accept rate is $\sim$ 100 Hz and events which passed the Level 3 trigger are sent to the consumer-server logger (CSL) through the switch.

Data analyzed in this analysis is collected triggering on a high p_T lepton (electron or muon). The lepton from the W boson decay gives a clear signature for WH production. The triggers used in this analysis is described below.

- High-p_T Electron Trigger
  In this trigger, electron candidates with high-p_T are triggered. At the Level 1 trigger, events are required to have a tower of electromagnetic calorimeter with $E_T > 8$ GeV and the ratio of hadronic to electromagnetic energy (Had/EM) with less than 0.125 in this tower. Additionally, this tower has to match to a track with $p_T > 8$ GeV from the XFT information. The XFT (extremely fast tracker) is one of the Level 1 trigger decisions provided by the COT.
  At Level 2, calorimeter energy reconstruction is performed using a more sophisticated clustering algorithm for electromagnetic objects. This improves energy resolution and allows a higher threshold of energy ($E_T > 16$ GeV).
  At Level 3, the lateral shower profile, L_{shr}, and the distance between CES z and the z-position of the extrapolated track, CES(Δz), are used. The L_{shr} variable quantifies the difference between the measured energy distribution in η among the towers neighboring the electron candidate in and the expected distribution which was determined from electron

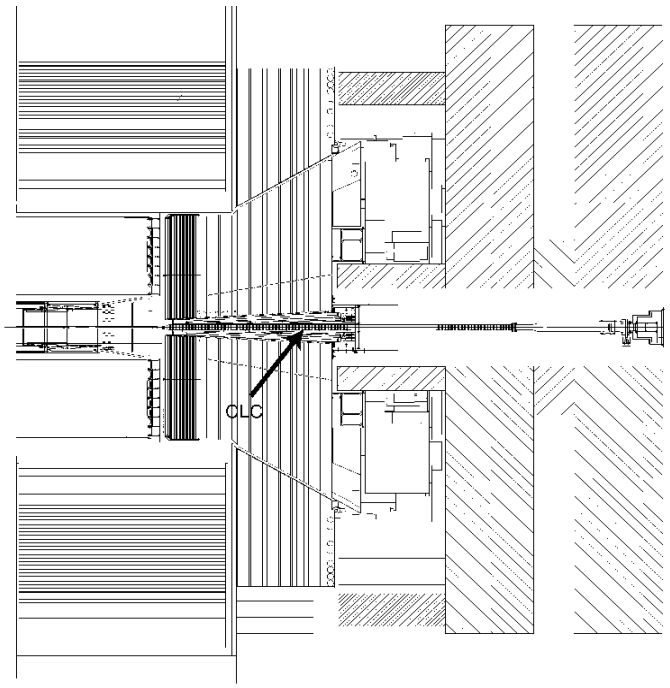

Figure 2.12: The Location of the CDF Cerenkov Luminosity Counter in the 3° gap between plug calorimeter and the beam pipe.

test beam data. The electromagnetic $E_T > 18$ GeV and the track $p_T > 9$ GeV are finally required.

- High-p_T Muon Triggers
  In this trigger, muon candidates with high-p_T are triggered. At Level 1 trigger, muon reconstruction start with a p_T estimate within the CMU and CMX chambers from the relative timing of the hits in different layers. The CMU track is combined with the reconstructed CMP track. The successful track is treated as "CMUP" muon candidate. For the majority of the data, CMX candidates also require local CSX hits consistent with particles originating from the collision. We require $p_T > 6$ GeV if CMU or CMX matched to a XFT track, $p_T > 4.09$ GeV for CMUP or $p_T > 8.34$ GeV for CMX.
  At level 2, the XFT track requirement for CMUP and CMX is raised to $p_T > 14.77$ GeV and the stereo confirmation in the COT is also added. For CMX, additionally, one jet with $E_T > 10$ GeV is required to reduce the trigger rate in high luminosity.
  At level 3, matching of a fully reconstructed track to "stub" of muon detector is required, $|\Delta x|_{CMU} < 10$ cm and $|\Delta x|_{CMP} < 20$ cm for CMUP muon and $|\Delta x|_{CMX} < 10$ cm for CMX. The needs to have $p_T > 18$ GeV for both muon types.

2.3.2 Consumer-Server/Logger Upgrade

The Consumer-Server/Logger [41] is located in the downstream in the CDF Data Acquisition chain before data is archived to tape. The CSL buffers the data in separate data stream, records file meta information into a database and sends a fraction of events to online processors for real time monitoring of data quality. Recently the CSL was upgraded because the Tevatron improvement has lead to beam stores, one cycle from injecting beam to aborting beam, with higher luminosity

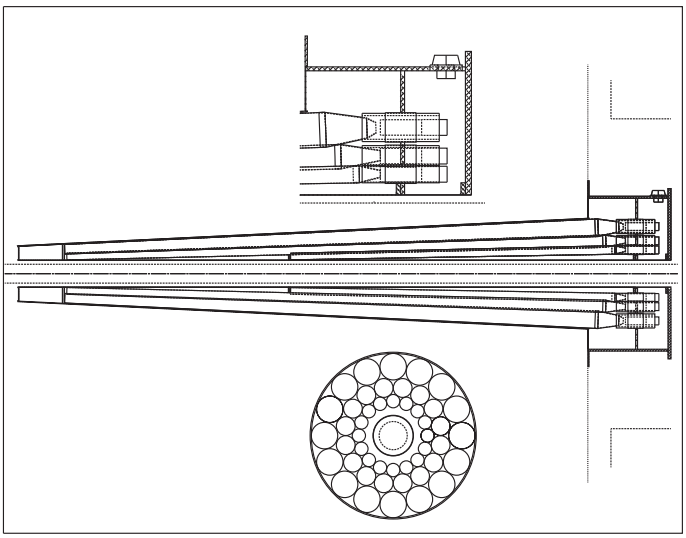

Figure 2.13: The CDF Cerenkov Luminosity Counter.

and the DAQ needed to handle the associated higher data logging rates. The upgrade needs to sustain the data logging rate of 65 MB/s (250 Hz from L3 output). In order to allow sufficient headroom, a design target for the CSL upgrade was set to 80 MB/s. The design incorporates an over-capacity of bandwidth, disk buffering and processing power to allow any failed component to be bypassed without preventing data logging. An overview of the upgraded CSL system is shown in Figure 2.16. The events from L3 are sent to the receiver node through a gigabit Ethernet switch. The receiver node distributes them to each logger depending on data stream. The data disk consists of two disk arrays, which are connected to the logger node via a FC network. The data disk capacity is 24 TB. It sustains to buffering data for three days while running at the full design specification of 80 MB/s.

The upgraded CSL system was designed to achieve high reliability and redundancy in each component. The network link from L3 to the receiver node and the receiver node output is configured “bonding”, which is aggregated two links and works like one double bandwidth. If one link is down, the remaining link works without interrupting the data taking. Figure 2.17 shows the total bandwidth between receiver and logger nodes. Thanks to bonding, the total bandwidth over 200MB/s was accomplished which is sufficient for the original design. The link between logger node and disk array also has two links. If one disk is down, data taking is able to continue using another disk. Furthermore, some spare nodes are prepared. When a node is down, the network is switched to another node automatically using software. The buffered data is sent to tape in certain interval. This CSL system was tested using the actual software and hardware. A total throughput of 100MB/s was obtained, satisfying the design value.

The CSL system is designed to automatically address a large set of problems, thereby minimizing the need for user intervention. For this design, the CSL has some monitor for maintenance. An overview of the flow of monitoring information is shown in Figure 2.18. CSLmon receives the status information from receiver, logger and RTserver. These information on the overall performance is displayed on a dedicated Java based monitor. Besides some history plots of status are able to be checked via Web. This information helps quick notification of the CSL problem for quick recovery by experts.

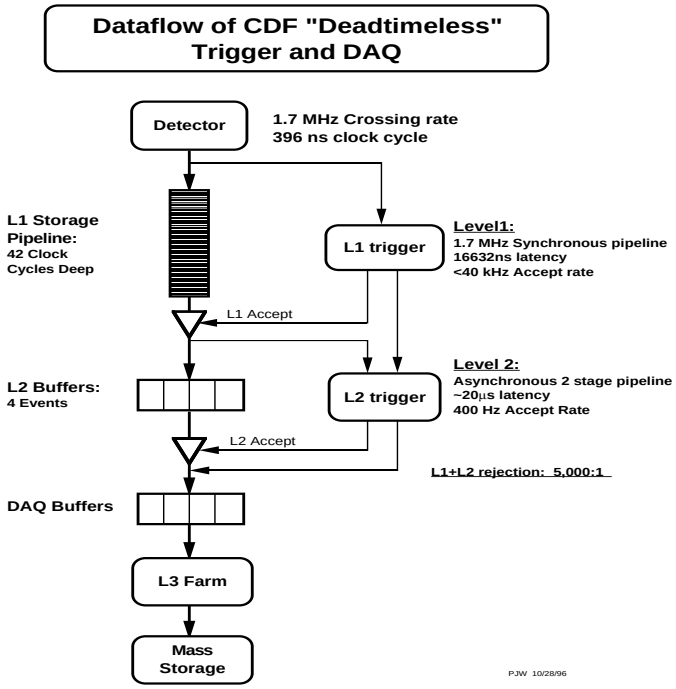

Figure 2.14: The schematic view of CDF trigger and data acquisition system.

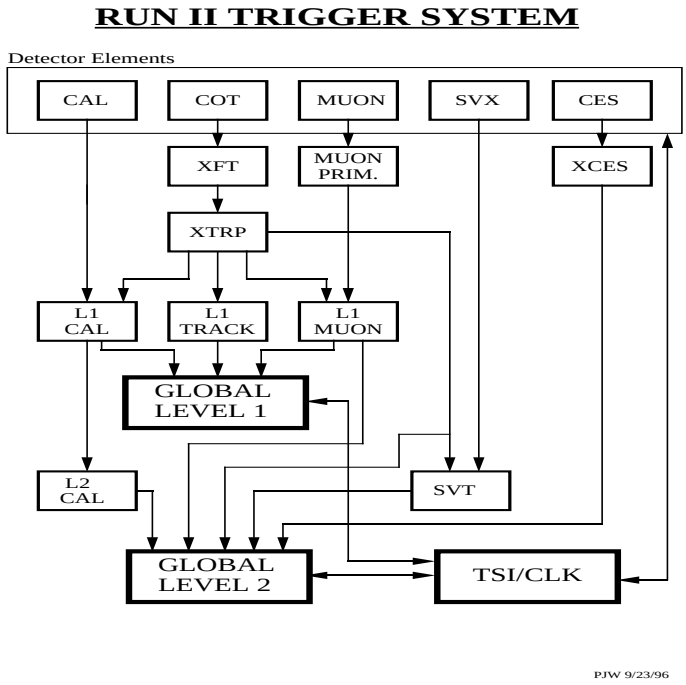

Figure 2.15: The block diagram of the Level 1 and Level 2 trigger path from each CDF detector component.

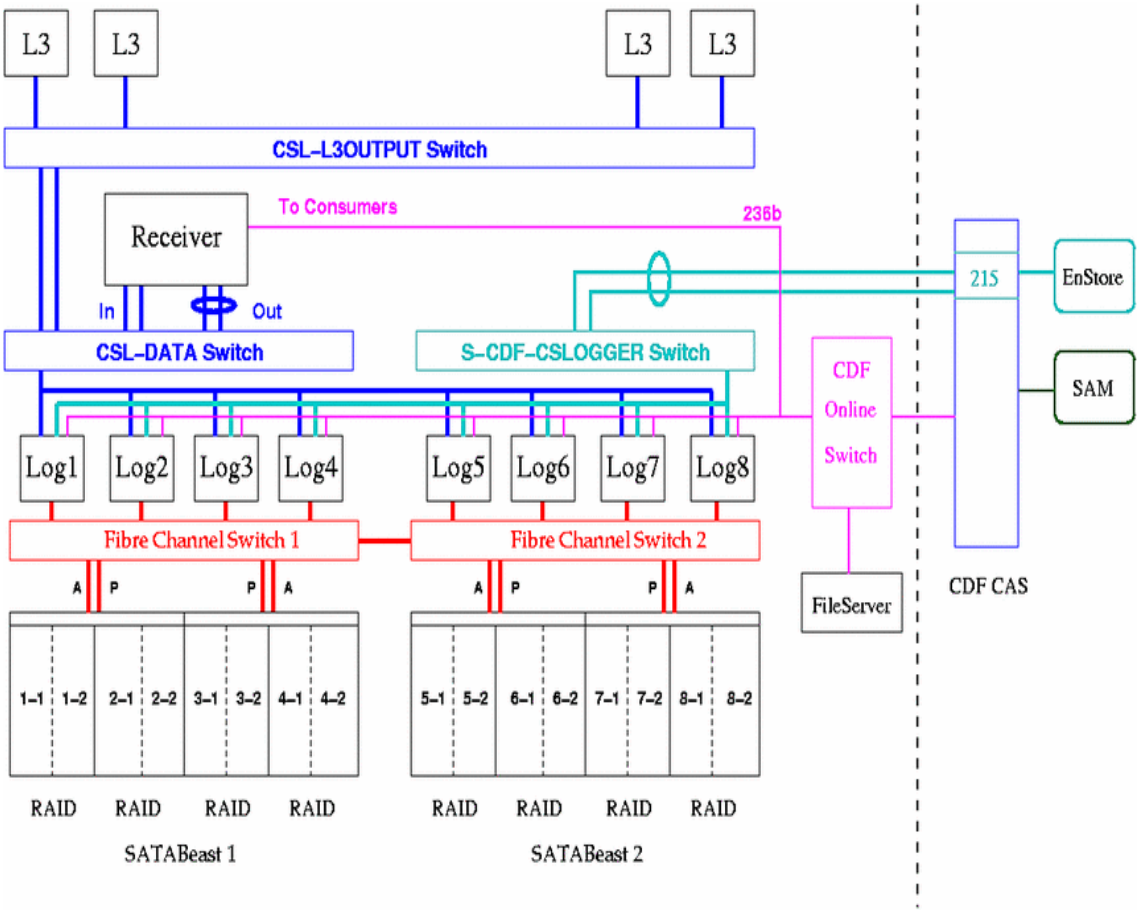

Figure 2.16: The schematic view of new CSL system architecture.

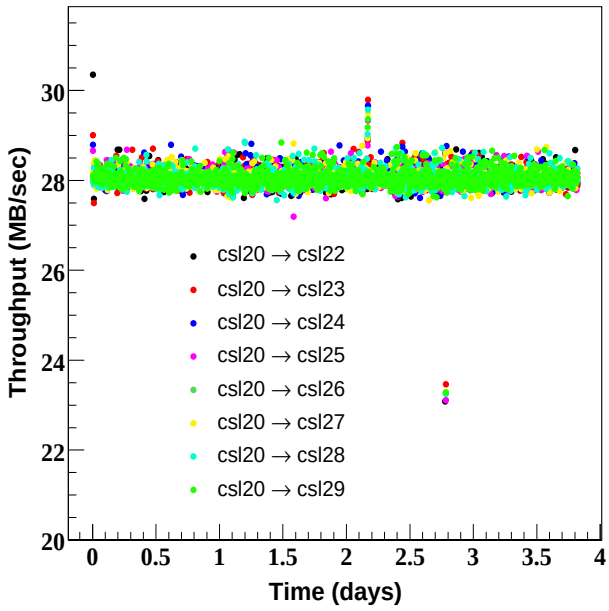

Figure 2.17: The throughput from receiver node to each logger. The receiver send data to each node simultaneously. Observed total throughput is over 200MB/s averaged for 4 days. One bump (at 2.2 days) and one dip (at 2.8 days) resulted from restarting the network.

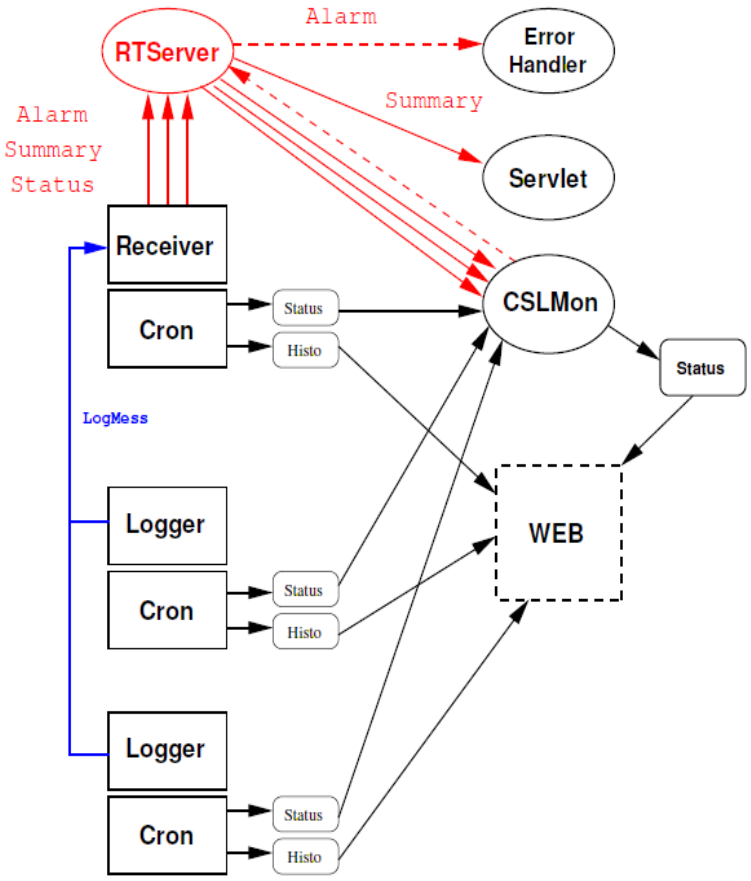

Figure 2.18: An overview of the flow of information used to monitor the CSL.

Chapter 3

Particle Identification

In this chapter, we describe the particle identification of objects detected at CDF. WH channel has one lepton, the missing transverse energy from neutrino and two b-jets. To identify the signal events, we first describe the track reconstruction at CDF and then the electron and the muon identification are described. Jet reconstruction and correction and measurement of missing transverse energy are described.

3.1 Track Reconstruction

In this section, we describe the tracking reconstruction algorithm at CDF tracking system. The precise tracking measurement is needed to identify trajectory of charged particles such as electron and muon.

The tracking reconstruction is accomplished via several steps. The first step is to find segments at COT. The segment sets of three hits consistent with a straight line trajectory. This straight line is decided by the method of least squares. These segmentson COT are used to reconstruct the track. The track is first reconstructed with axial superlayers only. Two reconstruction algorithm are performed in parallel in order to increase the reconstruction efficiency.

First method is called the "Segment Linking" algorithm first reconstructs the track using the segments in the outer two axial superlayers and then link segments from inner two superlayers to the tracks or to unlinked segments from outer superlayers. Second method is called the "Histogram Linking" which starts with a segment position and the beam position, and the histogram has ± 1 cm of distance, equal to the distance from the nominal track position and the bin size to 200 μm. If the bin contains at least 10 hits, a track is made by these hits. All hits from other axial superlayers are added to the track if their positions are within ~ 750 μm of the nominal track position at that superlayer, where the nominal position is defined by the histogram bin with the most hits.

After reconstruction of tracking with axial superlayer, the stereo segment linking algorithm is performed for its every track. These linking is attempted from outer stereo superlayer to inner and then the track is refitted.

Once a track is reconstructed in the COT, it is extrapolated into the SVX detectors by adding hits to the track and recalculating the track parameters. In this "Outside-In" procedure, $r - \phi$ hits clusters are first added and then hits with stereo information are added to track. At the end of a series of procedure, one track is determined in based on the number of silicon hits and on the χ^2 of the fit. At the CDF, there is the tracking algorithm extrapolated from SVX to COT to increase tracking efficiency in the forward region. Its "Inside-Out" tracking procedure and further descriptions and performance of the tracking can be found in [43, 44].

3.2 Electron Identification

The electron identification is based on the tracking and the calorimeter. Electrons have a characteristic signature in the calorimeter since an electromagnetic shower is almost entirely contained in the EM calorimeter. The energy attributed to the electron is the total energy of the EM cluster. The EM cluster needs to be associated with a track. As for the momentum we take the track with highest p_T associated with the cluster. The direction of this track is used to the compute the electron transverse energy $E_T = E \sin\theta$. The electron selection criteria depend on the detector region which the electron candidate passes through. Central electron (CEM) criteria shown in Table 3.1 are applied for selecting electrons and rejecting the background using the following variables.

- Large transverse energy deposit (E_T) in the calorimeter
- Large transverse momentum (p_T) measured from the track with COT hit coming from luminous region ($|z_0| < 60$ cm)
- Energy deposit in EM cluster E_{EM} is much higher than energy deposit in Hadron cluster E_{HAD}
- Matching between the calorimeter cluster and track
- EM shower shape characterized in a variable, L_{shr}
  L_{shr} is defined as

  $$L_{shr} = 0.14 \times \sum_k \frac{M_k - P_k}{\sqrt{0.14^2 E_{cluster} + \sum(\Delta P_k)^2}}$$

  where the sum is over the towers adjacent to the seed tower in the cluster, M_k is a measured energy on the adjacent tower k, P_k is the same quantity predicted from a test beam at the impact point in z measured by the strip chamber.
- Removal of charged hadron which mimics the electron using CES and COT. The track is required to match a CES cluster in both axial ($|\Delta z| < 3.0$cm) and azimuthal (-1.5cm $< Q \cdot \Delta x <$ 3cm, where Q is the charge of the electron) directions. In the azimuthal direction, the shower asymmetry caused by the electron bremsstrahlung is taken into account. The shape of the CES cluster is required to be similar to the one evaluated from test beam data based on a χ^2 test.
- Isolation
  E_T^{cone}/E_T, where E_T^{cone} is the transverse energy sum within $\Delta R < 0.4$ cone around the cluster excluding the electron cluster itself.

Table 3.1 shows the summary of selection criteria. The photon is possible to fake the electron candidate if the photon converts to an electron-positron pair as it goes through material. Such a photon (Photon conversion) is identified by looking for pairs of COT tracks satisfying:

- The two tracks have oppositely charged
- $|\Delta(xy)| < 2.0$ mm
- $|\Delta(cot\theta)| < 0.04$

where $\Delta(xy)$ is the distance between the tracks in the transverse plane and $\cot\theta$ is the difference between the polar angle cotangents of the tracks

Variables	cut value
Fiducial	Requirement to be in the active region of the CES and CEM
E_T	$>$ 20 GeV
p_T	$>$ 10 GeV/c
$\|z_0\|$	$<$ 60 cm
COT axial superlayer segments	$\geq$ 3 (COT hits $\geq$ 5)
COT axial superlayer segments	$\geq$ 2 (COT hits $\geq$ 5)
E/p	$<$ 2.0
E_{HAD}/E_{EM}	$<$ 0.055 + 0.00045$\times E$
L_{shr}	$<$ 0.2
$\|\Delta z\|$	$<$ 3.0 cm
$Q \times \Delta x$	$\geq$ -1.5 cm and $\leq$ 3.0 cm
CES χ^2	$\leq$ 10 cm
Isolation	$<$ 0.1

Table 3.1: CEM electron selection criteria.

3.3 Muon Identification

Muons do not leave much energy in the EM calorimeter because they do not initiate EM shower due to their large mass. Also muons do not interact strongly in hadron calorimeter. As a result, muons with a energy of a few GeV or more pass through the calorimeter with leaving small energy deposits due to minimum ionization. As discussed in the previous chapter, muons are identified by matching hits in the muon chambers with a reconstructed track and requiring that the small energy left in the calorimeter on the trajectory of the particle. In each muon subsystem, the 4 layer structure allows to reconstruct a track segment called "stub". A muon is reconstructed if such a stub is detected in one of the muon systems.

Muons can be mimicked by hadrons that shower unusually late or passed through the detector ("punch-through") without hadron interaction. Another source of background is muons from cosmic rays. This background is removed by using the timing information from COT and the muon chamber and by the impact parameter.

Muons are separated in two categories depending on the detector region. One is a muon called CMUP in the most central region within $|\eta| < 0.6$ and another is a muon called CMX in the region $0.6 < |\eta| < 1.0$. For each muon, the following selection criteria are applied.

- The track requirement is the same as for the electron. The track should come from the luminous region ($|Z_0| < 60$ cm)
- High transverse momenta (p_T)
- Small energy deposit in the hadron and EM calorimeters
- Isolation
  E_T^{cone}/p_T, where E_T^{cone} is the transverse energy sum in the cone of $\Delta R = 0.4$ around the muon track excluding the tower associated with the track
- For CMX muons, the track is required to go through all COT superlayers.

Variables	cut value
p_T	$>$ 20 GeV/c
$\|z_0\|$	$<$ 60 cm
COT axial superlayer segments	$\geq$ 3 (COT hits $\geq$ 5)
COT axial superlayer segments	$\geq$ 2 (COT hits $\geq$ 5)
$\|d_0\|$ if no Si hits (w/ Si hits)	$<$ 0.2cm (0.02cm)
Radius to exit COT (CMX-only)	$>$ 140 cm
E_{EM}	$<$ max(2,2+0.0115(p-100))
E_{HAD}	$<$ max(6,6+0.0280(p-100))
$\|\Delta x\|_{CMU}$	$<$ 3.0cm
$\|\Delta x\|_{CMP}$	$<$ 5.0cm
$\|\Delta x\|_{CMX}$	$<$ 6.0cm
x_{fid}	$<$ 0cm for CMU,CMP and CMX
z_{fid}	$<$ 0cm(-3cm) for CMU (CMP and CMX)
Isolation	$<$ 0.1

Table 3.2: CMUP and CMX selection criteria. p means GeV/c unit.

- Cosmic ray removal using impact parameter d_0. If hits from the silicon detector are attached to the candidate track, the requirement on the impact parameter is set more strict since the resolution is much improved.
- The track is required to match the muon stub in the axial direction: Δx used in this selection is the distance in the x-y plane between the muon chamber hits and the track extrapolated to the muon chamber. The cut threshold depends on the muon system.
- The fiducial requirement. The fiducial distances of the tracks in the transverse plane and the z-direction are represented by x_{fid} and z_{fid}, respectively.

Table 3.2 shows the summary of the muon selection criteria.

3.4 Jet Reconstruction

Quarks and gluons produced in the collisions undergo fragmentation as they travel away from the interaction point. This results in stream of energetic colorless particles propagating in relatively narrow cone around the original parton direction. The jet consists of a bunch of neutral and charged light mesons and baryons mainly and its energy is measured as the sum of energy depositions in the calorimeter. Jet clustering is the procedure whereby the energy depositions are associated with the original parton, while the energy deposited in remote calorimeters is not associated.

The jet clustering starts with the most energetic calorimeter tower , called a seed tower, and computes the energy sum in cone of a given $\Delta R = \sqrt{\Delta\eta^2 + \Delta\phi^2}$. This analysis uses the cone size of ΔR = 0.4. After a cluster is formed around the seed tower, the position of E_T -weighted centroid is computed as:

$$\eta_{centroid} = \frac{\sum_i E_T^i \eta^i}{\sum_i E_T}, \quad \phi_{centroid} = \frac{\sum_i E_T^i \phi^i}{\sum_i E_T} \tag{3.1}$$

The centroid position defines the new cluster center and the new clustering cone is drawn around it. The processes are repeated until the cluster remains unchanged. In some situations the

overlap of clusters are merged if the overlap is more than 75% or left unchanged. A jet "raw" four-momentum is then detemined based on the energy of the cluster and the position of the centroid. There are a lot of effects both from physics and detector effects that contribute to the deviation of the jet four-momentum constructed as outlined above and the four-momentum of the original parton. At CDF several corrections are applied for raw jet $p_{T,jet}^{measured}$ and corrected jet p_T^{parton} is represented as

$$p_T^{parton} = [p_{T,jet}^{measured} \times f_{rel} - p_T^{MI} \times N_{vtx}] \times f_{abs} - p_T^{UE} + p_T^{OOC} \tag{3.2}$$

The CDF jet energy correction is done to several levels and users choose the level appropriate to their analysis. Each factor of Eq.3.2 corresponds to each level, where $p_{T,jet}^{measured}$ means a jet p_T measured in the calorimeter and with the jet cone algorithm. The correction for each step is :

- Level 1 : relative correction: f_{rel} is a scale factor to make the jet response uniform with η
- Level 2 : time-dependent correction, compensates for calorimeter deterioration over time, for example, aging of the photo-tubes
- Level 3 : raw energy scale, account for non-linearities in single-particle response
- Level 4 : multiple interactions: p_T^{MI} is from additional interactions in the same bunch crossing. It is subtracted depending on the number of reconstructed primary vertices N_{vtx} in an event
- Level 5 : absolute energy correction: f_{abs}, determined by matching particle jets with calorimeter jets to correct for calorimeter response.
- Level 6 : underlying event: the contribution of p_T^{UE} coming from spectator parton is subtracted.
- Level 7 : out-of-cone correction: the effect of p_T^{OOC} is added, which is the energy of the parent parton emitted outside the jet cone due to final state gluon radiation.

Level 2 and 3 are not used presently because Level 2 correction is already included in raw level jets and Level 3 correction is covered by other uncertainties. The estimate of the systematic uncertainties and the calibration are performed using the generic jet sample [45, 46]. The CDF jet energy correction is applied to obtain the jet energy at hadron level up to Level 5 and at parton level using up to Level 7. Jet energy correction up to Level 5 is applied before the event selection.

3.5 Missing Transverse Energy Measurement

The neutrino escapes from the CDF detector without any response. However as the transverse momenta of initial proton and antiproton are null, the vector sum of the total transverse momentum of all objects should be null due to the conservation of momentum. Thus the high p_T neutrino causes an imbalance in the vector sum of transverse momenta. This imbalance is measured by combining the information from all calorimeter towers and it is defined as the missing transverse energy.

$$\not\!\!\boldsymbol{E}_T = -\sum_{i=towers} \boldsymbol{E}_T^i$$

where $\not\!\!E_T$ is a two dimensional vector in a transverse plane. This missing transverse energy is measured from the raw calorimeter response. It needs to be corrected as the jet energy correction is applied and the momentum of muons escaped from the calorimeter.

Muons deposit only small minimum ionization energy and escape from the calorimeter. The muon momentum effect is taken into account by adding muon momentum measured from the tracking and subtracting the energy deposit in the calorimeter.

The calorimeter object identified as a jet is corrected by jet energy correction as described above. The corrected energy is taken into account for the $\not\!\!E_T$ correction. The missing E_T resolution is affected by various objects, with the jet resolution being dominant. The best $\not\!\!E_T$ resolution is achieved with jet correction of Level 5.

Chapter 4

b-Tagging Algorithm

4.1 Introduction

The ability to identify jets originating from heavy flavor quark (bottom or charm) production is crucial for this analysis. For the Higgs mass range $m_h < \sim$135 GeV/c^2, the Standard Model Higgs is predicted to decay predominantly to b quark pair as shown in the preceding chapter. The most dominant background in this analysis is W + 2 jets production which does not contain heavy flavor quarks in the final state. Thus identifying b jets to reduce the background is a key of search for the Higgs boson. We call the b jet identification "b-tagging".

Several ways to identify b-jets have been developed by utilizing properties of b-jet. There are characteristics of b-jets that are different from light flavor jets

- the long lifetime of the b hadron
- the large mass of b hadron
- the energetic semileptonic decay of b hadron

One technique is to look for a low momentum electron or muon coming from the semileptonic decay of b hadron, Soft Lepton b-Tagging (SLT). This method is limited by the small semileptonic decay branching ratio ($\sim 11\%$) and by the difficulty of reconstructing relatively low momentum leptons in a jet. Another method is "Secondary Vertex b-tagger (SECVTX b-tag)" making use of large decay length of b hadron and displaced vertex. This method is most widely used in CDF. The detail algorithm of SECVTX b-tag is described in the following section. Another method is "Jet Probability b-tagging" utilizing the difference between impact parameter of tracks coming from secondary vertex and prompt tracks coming from the primary vertex. The algorithm of Jet Probability b-tagging is described in the following section. In this analysis, two b-tagging algorithms, SECVTX and Jet Probability b-tagging are applied to reduce the large W + jets background.

Additionally, flavor separation method with Neural Network (NN) is developed to increase purity of b tagged jets with SECVTX algorithm. This method is applied to reduce the background events. The detail of NN flavor separation is described in the following section.

4.2 Primary Vertex Finding

Before reconstructing the secondary vertex in b-tagging, precise knowledge of the collision point is needed. In this section, event-by-event primary vertex finding algorithm is described.

To find an event by event primary vertex, we first identify the vertex of the identified high-momentum electron or muon. For other data sets without high-momentum leptons, we use the vertex which has the highest total scalar sum of transverse momentum of associated tracks. The position of the primary vertex is then determined by fitting together the tracks within a ± 1 cm window in z around this vertex using CTVMFT [47]. It then calculates the χ^2 to this vertex of tracks with $p_T > 0.5$ GeV, $|d_0|$ <1.0 cm and $|d_0/\sigma_{d_0}| < 4.0$ with respect to the beam line. Here $|d_0/\sigma_{d_0}|$ includes the uncertainty on both the track and the beam line positions. The transverse profile of the beam line is also used as the original z vertex in the fit. A pruning stage removes tracks which contribute $\chi^2 > 10$ to the fit. After initial pruning, repeat the fit using remaining tracks until no tracks have $\chi^2 > 10$ relative to the vertex. If no tracks survive the pruning stage then the beam line profile is used for the primary vertex position estimate. In the event sample used in this analysis the uncertainty in the fitted transverse position ranged from 10-32μm depending on the number of reconstructed tracks.

4.3 Secondary Vertex b-Tagging

The most widely used method is the secondary vertex b-tagger, which takes advantage of the long lifetime of the b hadrons. The b-quark hadronizes almost immediately (on the order of 10^{-24} s) to form a jet of particles; included in this jet are a b meson ($B^0, B^{\pm}$...) or a b baryon (Λ_b). The b hadron usually carries off most of the original b-quark momentum and has a relatively long lifetime (of order several ps). Given their long lifetime and large relativistic boost, b hadrons created in this way travel a significant distance before decaying into several charged and neutral particles. The distance is given by L = $\beta c\tau'$, where β is the velocity and τ' is the proper lifetime ($\tau' = \tau\gamma$). For example, the typical transverse energy of a b hadron jet from the Higgs decay is 40 GeV. Neutral b mesons of the mass 5.28 GeV/c^2 have a boost $\beta\gamma = 7.6$ and a lifetime $c\tau = 458.7\mu$m. Therefore the average decay length is $\sim$ 3.5 mm. b hadrons decay into multiple particles, producing a secondary vertex displaced from the primary vertex. These tracks from the secondary vertex are reconstructed with the silicon microstrip detector.

4.3.1 Secondary Vertex Reconstruction Algorithm

Secondary vertex b-tagging operates on a per-jet basis, where only tracks with the jet cone radius $\Delta R = 0.4$ in $\eta - \phi$ plane are considered for each jet in the event. A set of cuts involving the transverse momentum, the number of silicon hits attached to the tracks, the quality of those hits, and the χ^2/ndf of the final track fit are applied to reject poorly reconstructed tracks. Only jets with at least two of these good tracks can produce a displaced vertex; a jet is defined as "taggable" jet if it has two good tracks. Displaced tracks in the jet are selected based on the significance of their impact parameter with respect to the primary vertex and are used as input to the SECVTX algorithm. SECVTX uses a two-pass approach to find the secondary vertices.

- Pass 1:
  The first pass requires at least three tracks with $p_T > 0.5$ GeV/c and $|d_0/\sigma_{d_0}| > 2.0$, and then attempts to reconstruct a secondary vertex. At least one of the tracks used to reconstruct the secondary vertex must satisfy $p_T > 1.0$ GeV/c.

- Pass 2:
  If the first pass is unsuccessful, it performs a second pass which makes tighter track requirements ($p_T > 1.0$ GeV/c and $|d_0/\sigma_{d_0}| > 3.5$) and attempts to reconstruct two-track vertex. At least One of tracks have to satisfy $p_T > 1.5$ GeV/c.

Once a secondary vertices are found in a jet, the two-dimensional decay length of the secondary vertex L_{xy} is calculated as the projection onto the jet axis, in the x-y view only, of the vector pointing from the primary vertex to the secondary vertex. The sign of L_{xy} is defined relative to the jet direction, specifically by the angle α between the jet axis and the secondary vertex vector (positive for $\alpha < \pi/2$, negative for $\alpha > \pi/2$). Figure 4.1 shows a schematic view for a positive and a negative L_{xy}. Secondary vertices corresponding to the decay of b and c hadrons are expected to have a large positive L_{xy}, while the secondary vertices from random mis-measured tracks are expected to be less displaced with respect to primary vertex.

To reduce the background from the false secondary vertices, a good secondary vertex is required to have $L_{xy}/\sigma_{L_{xy}} > 7.5$ for positive tag and $L_{xy}/\sigma_{L_{xy}} < -7.5$ for negative tag, where $\sigma_{L_{xy}}$ is the total estimated uncertainty on L_{xy} including the primary and secondary vertices. Additionally, in order to reject secondary vertices due to material interaction, we converged on not allowing any vertices with exactly two Pass 1 tracks where the vertex is found 1.2 and 2.5 cm with respect to the center of SVX detector. All vertices with a radius greater than 2.5 cm with respect to the center of the SVX are vetoed. Besides decays from K_s, Λ are removed by reconstructed invariant mass from tracks. These vertices are vetoed if the mass is in K_s, Λ mass region.

There are looser operation points in SECVTX b-tagging algorithm. In this loose selection, some requirements such as a vertex fit χ^2 are looser. Finally a good looser secondary vertex is required to have $L_{xy}/\sigma_{L_{xy}} > 6.0$ for positive tag and $L_{xy}/\sigma_{L_{xy}} < -6.0$.

The negative tag defined above is useful for calculating the false positive tag rate. Because the L_{xy} distribution from light flavor jet represents track reconstruction resolution. This distribution is expected to be symmetric. The following section describes more details about the mistag.

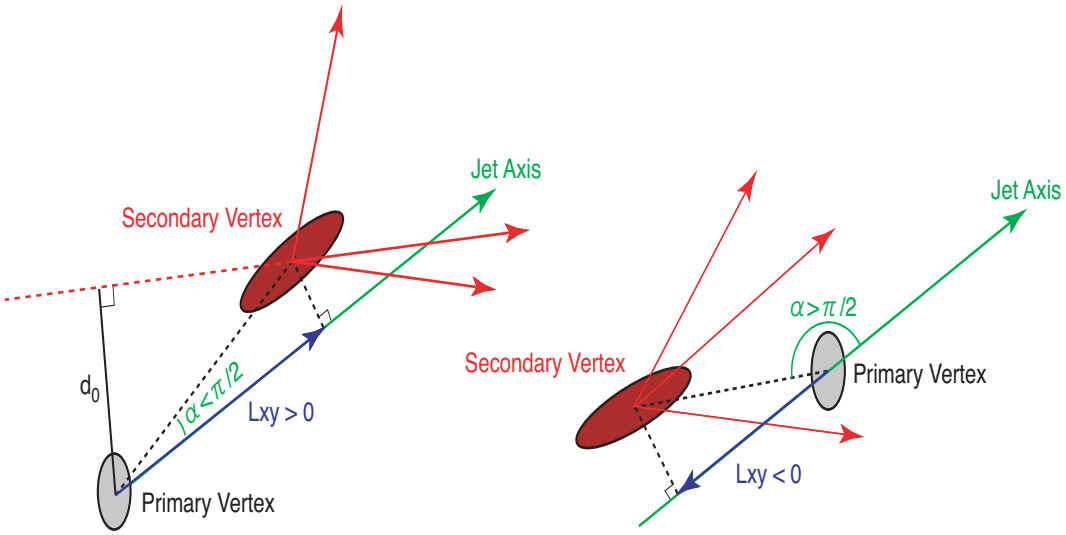

Figure 4.1: Schematic view in x-y plane of a positive secondary vertex (Left) and a negative secondary vertex (Right).

4.3.2 Secondary Vertex b-Tagging Performance

4.3.3 b-tagging Efficiency and Scale Factor

The efficiency of the SECVTX b-tagging algorithm is defined as a fraction of b jets in the fiducial volume of the COT and calorimetry that possess a positive SECVTX b-tag. Measuring the

b-tagging efficiency is straightforward in Monte Carlo events; one has the luxury of complete knowledge of the particles within each jet, and thus it is straightforward to identify the fiducial jets that come from b quark production and the fraction which are tagged. But this is not to say that the efficiency measurement in Monte Carlo jets is accurate. Reliable modeling of b-tagging in the Monte Carlo requires precise understanding of the charge deposition in the silicon detectors, accurate simulation of the tracking, and realistic b hadron production and decay models. Since none of these effects are perfectly modeled in the Monte Carlo, it is imperative to measure the b-tagging efficiency in the data.

The b-tagging efficiency measurement in data at CDF relies on constructing a pure sample of b jets within the large dijet sample. Two methods [48], currently in use at CDF utilize high p_T leptons matched to jets to identify jet pairs consistent with heavy flavor. The SECVTX tagging efficiency depends strongly on jet kinematics (E_T and η); these jet properties will clearly vary depending on the physics process one considers. Besides the tagging efficiency is used to assess the signal acceptance, which is typically done in signal Monte Carlo samples. As discussed above, Monte Carlo b-jets are not guaranteed to perfectly match data with the b jets. Therefore it is necessary to estimate a data-to-MC scale factor for the tagging efficiency, which corrects the discrepancies between MC and data. Using the same method [48] to calculate the tagging efficiency for MC, we obtained a scale factor of 0.95$\pm$0.05. The major source of systematic uncertainties is the jet E_T dependence. The tagging efficiency multiplied by this scale factor is shown in Figure 4.2 for the MC b jets from top decay.

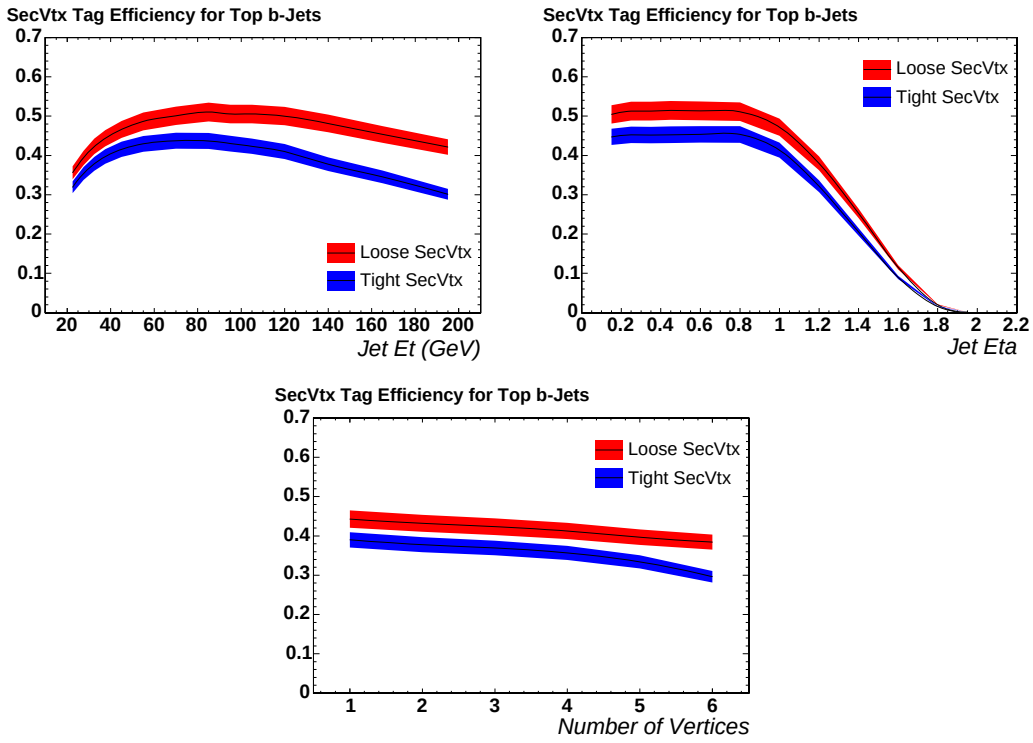

Figure 4.2: Tagging efficiency for b jets in top decay as a function of jet E_T , η and number of vertices for loose and tight SECVTX's.

One can see that the tagging efficiency decreases slightly as jet E_T increases. This is due to in part the collimation of tracks in high E_T jets which makes vertexing difficult. The removal

of vertices from the material interaction also contributes to the decrease in efficiency at high jet E_T . The efficiency reduction for $|\eta| > 1.0$ is due to the degraded tracking efficiency and silicon coverage in the forward region.

4.3.4 False Positive Tag Rate

False positive tag (mistag) in SECVTX comes from the spurious identification of a secondary vertex in a non-b jet. Jets from light flavor production should be consistent with zero lifetime. However tracks within a light flavor jet can still have a large impact parameter and hence satisfy the secondary vertex requirements. Sources of such spurious large impact parameter tracks include:

- incomplete tracking detector resolution
- long-lived light particle decays (Λ, K_s)
- material interactions

Mistags resulting from the detector resolution are expected to be symmetric in the signed L_{xy} . Therefore the negative tagged jets ($L_{xy} < 0$) is used for estimating the light flavor jet contribution in the positive tag sample.

Actually the mistag rate is calculated from the inclusive jet samples. The probability for a given jet to have a mistag is determined from the probability that the jet has a negative tag. This probability is parametrized by six variables:

- E_T of jet
- η of jet
- track multiplicity
- $\sum E_T^{jet}$
- number of vertices
- Z position of primary vertex

The parametrization is built from the inclusive jet samples and then is used to predict the number of mistags in the data samples since it is considered on a jet-by-jet basis. Finally the probability of each jet to have a negative tag is extracted from the six-variable parameterization. These predictions have been shown to be valid within 6.6% systematic uncertainties, which is dominated by the choice of calibration sample used to make the mistag parameterization.

There are other sources of mistag other than the resolution effect. Simply assuming that all mistagged jets are symmetric about the origin in L_{xy} will lead to an underestimate in the rate of false positive tag because the other contribution tends to mimic positive L_{xy} . These contributions are corrected by a scale factor after estimating the mistag from the resolution effect. With this prescription, the predicted mistag rate matches better the true rate of positive tags in the sample of non-heavy flavor sources. It also takes into account the contribution to the negative tagged sample from real heavy flavor jets. The systematics on the asymmetry sources is dominated by the uncertainty in the heavy flavor fraction in the sample.

Figure 4.3 shows mistag rate with six dimensional parametrization and asymmetry correction as a function of jet E_T and η. Energetic jets have more energetic charged particle tracks that can pass the p_T requirements for the SECVTX algorithm. That is why the mistag rate increase with jet E_T . In chapter 7, the method to estimate the mistag background with mistag matrix is described.

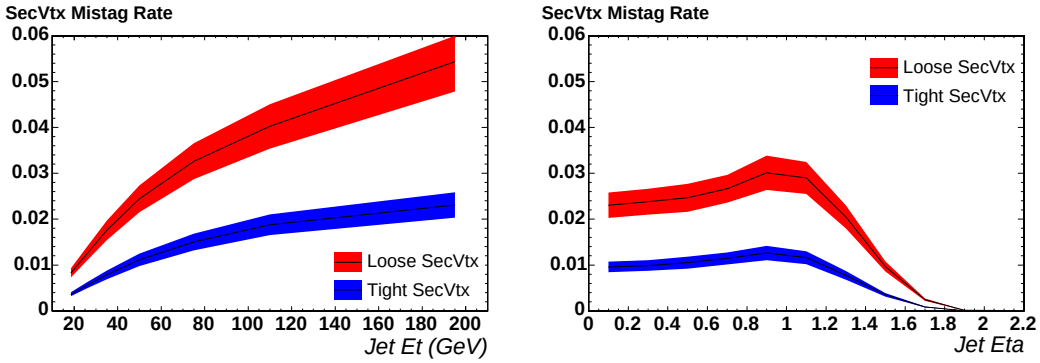

Figure 4.3: Mistag rate in inclusive jet data as a function of E_T and η for loose and tight SECVTX.

4.4 Jet Probability b-Tagging

Figure 4.4 (Left) illustrates a jet consisting of two tracks and their impact parameters. One can give a sign to the impact parameter according to the angle ϕ between the jet axis and the direction to the track closest point from the primary vertex. The sign is defined as

- sign = positive if $\cos\phi > 0$
- sign = negative if $\cos\phi < 0$

Another way of expressing this definition is

- sign = positive if the point of intersection of the track on the jet axis is in the same hemisphere as the jet direction
- sign = negative if the point of intersection of the track on the jet axis is in the opposite hemisphere as the jet direction

For a primary jet, all particles should originate from the primary vertex. Due to the finite tracking resolution, these tracks are reconstructed with a non-zero impact parameter and have an equal probability to be either positive or negative signed as shown in Figure 4.5(left). The width of impact parameter distribution from these tracks is solely due to the tracking resolution and the multiple scattering. A long lived particle as illustrated in Figure 4.4(right) will travel some distance along the jet direction before decaying, and its decay products will preferentially have positive signed impact parameter. The signed impact parameter distribution is shown in Figure 4.5(right).

The tracking resolution can be extracted from the data by fitting the negative side of the signed impact parameter distribution obtained for prompt jets which are dominant in inclusive jet data. Tracks are categorized into 72 different categories (η and p_T of tracks, quality of SVX-II hits) to parametrize their property. To minimize the contribution from badly measured tracks with large reconstructed impact parameters, the distribution of a related quantity, the signed impact parameter significance S_{d_0} (ratio of the impact parameter to its uncertainty) is parametrized at each track category. The impact parameter significance for each track is required to satisfy the quality criteria listed below. The jets with qualified tracks are required $E_T > 7$ GeV and $|\eta| < 2.5$. The event is required to have at least one primary vertex which is the vertex giving highest transverse momentum sum of all tracks.

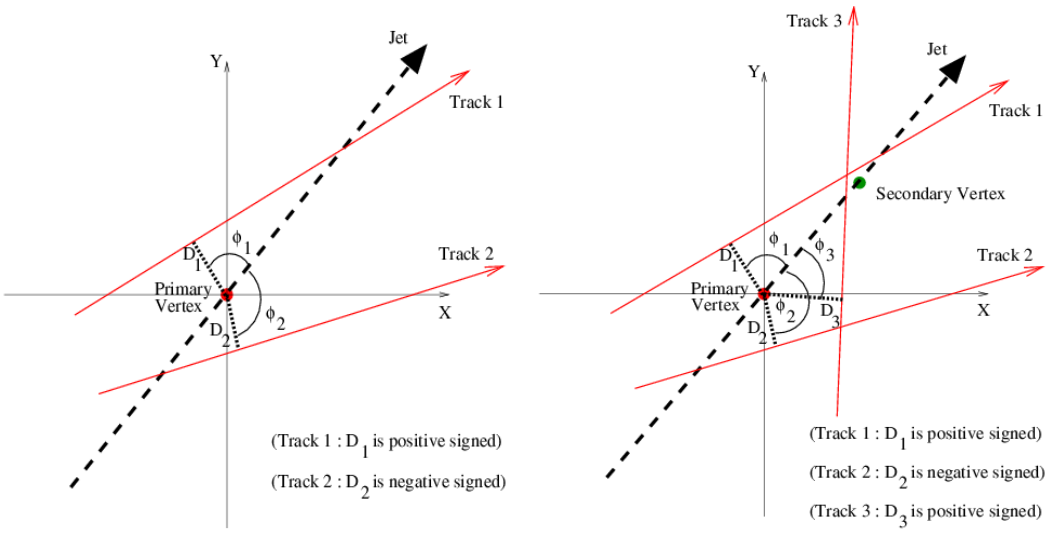

Figure 4.4: (Left) track from a primary vertex. (Right) tracks from a secondary vertex.

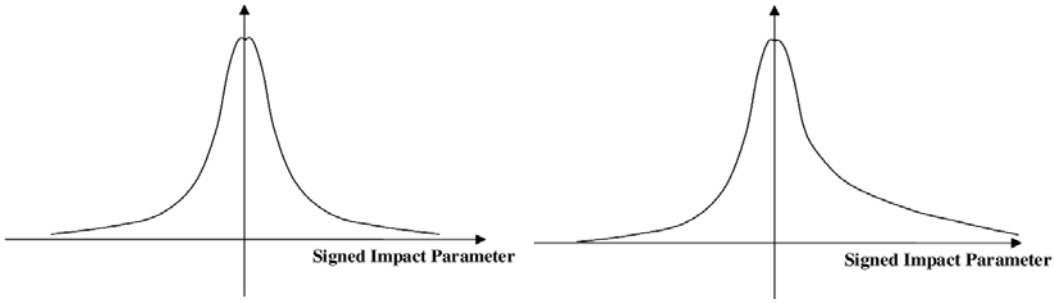

Figure 4.5: (Left) Signed impact parameter distribution for tracks from primary vertex. (Right) Signed impact parameter distribution for tracks from secondary vertex.

- track $p_T > 0.5$ GeV/c
- impact parameter $|d_0| < 0.1$ cm
- $3 < N_{SVXhit} < 5$
- total number of COT axial hits ≥ 20
- total number of COT stereo hits ≥ 17
- $|Z_{track} - Z_{pv}| < 5$cm

4.4.1 Track Probability

The resolution function, $R(t)$ fitted with the negative side of signed impact parameter is used to determine the track probability, $P_{track}(S_{d_0})$ where t and S_{d_0} are signed impact parameter signifi-

cances. This track probability is defined as

$$P_{track}(S_{d_0}) \equiv \int_{-\infty}^{-|S_{d_0}|} R(t)dt$$

The S_{d_0} distributions fall quickly with increasing the absolute value of the impact parameter significance, but the tail can extend further long. In order to have a good fit to the tail we choose to use nonlinear bins, along the X axis, to increase the statistic in the tail. The X axis is transformed to $X = \ln(|S_{d_0}|)$. A resolution function parametrized as the convolution of four Gaussian. After the transformation to a logarithmic axis, the resolution function for all 72 track categories is given by

$$R(X) = N \sum_{i=1}^{4} \frac{p_i}{\sqrt{2\pi}\sigma_i} e^{(X-(e^{2X}/2\sigma_i^2))}$$

where p_i and σ_i are parameters of the fitting function and N is normalization factor.

The track probability should be flat between 0 and 1 for tracks with a negative signed impact parameter because its distribution should be the same as the distribution used for obtaining the fitted function. The track probability has a peak near zero for long-lived particles with large positive signed impact parameter.

4.4.2 Jet Probability

Next, we choose a combined probability of track probabilities in a jet. To see how this probability is constructed, consider a jet with two positive signed impact parameter tracks which have the track probabilities P_1 and P_2, respectively (see Figure 4.6). The curve shows the constant probability $\Pi \equiv P_1 P_2$ and the set of two-track combinations in the area below the curve have a probability less than or equal to Π. The area is defined to be the jet probability. For a two-track jet, the probability is P_{jet} = $\Pi(1 - \ln \Pi)$. In general, one can show inductively that

$$P_{jet} = \Pi \sum_{k=0}^{N-1} \frac{(-\ln \Pi)^k}{k!},$$

where

$$\Pi = P_1 P_2 P_3 \cdots P_N$$

By definition, the jet probability distribution should be flat for jets having only prompt tracks. Tracks with a negative impact parameter are used to define a negative P_{jet}, which is used to check the algorithm and to estimate the misidentification rate. A feature of this algorithm is that the b-tagging is performed using a continuous variable instead of a discrete object like a reconstructed secondary vertex. It therefore provides a variable that allows one to move continuously along the efficiency curve and to select the optimal signal-to-background ratio point for a specific analysis. Figure 4.7 shows the jet probability distribution for jets matched to b, c and light quark. We can apply an arbitrary cut by selecting jets with jet probability less than the cut threshold because a jet originating from a heavy flavor quark has a peak near zero in the jet probability distribution.

4.4.3 Jet Probability b-Tagging Performance

For the jet probability b-tagging, a scale factor is needed to consider the discrepancies between data and MC. To estimate the scale factor, we use the same method as SECVTX tag [49, 50]. The results are shown in Table 4.1. Main source of systematic uncertainties is the jet E_T dependence

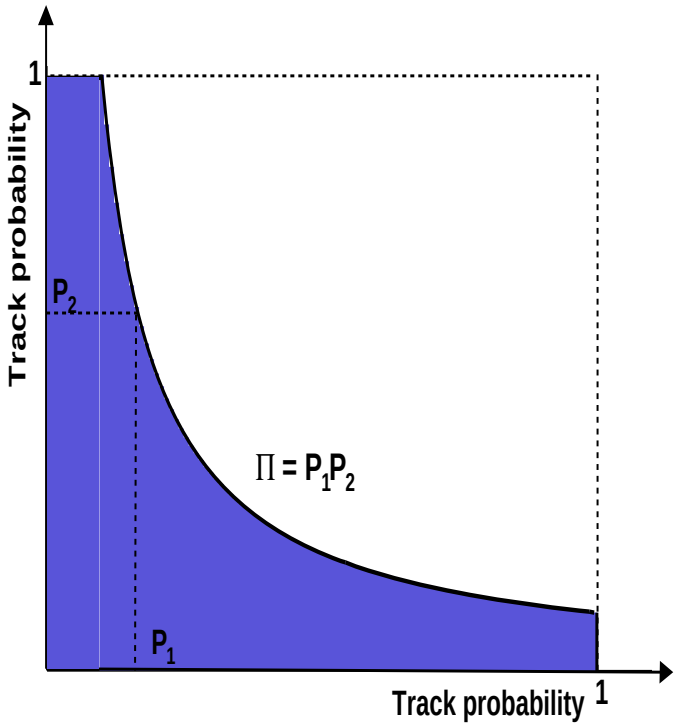

Figure 4.6: The definition of jet probability for two-track jet case. Two tracks have track probabilities P_1 and P_2, respectively. Jet Probability is defined as the shade area.

Cut threshold	JP $< 5\%$	JP $< 1\%$
Scale factor	0.846$\pm$0.017(stat)$\pm$0.066(sys)	0.786$\pm$0.020(stat)$\pm$0.057(sys)

Table 4.1: Scale factor of jet probability for two cut thresholds.

as the SECVTX tagging. Figure 4.8 show the tagging efficiency as a function of E_T and η of jet in Higgs MC.

For false tag estimation of the jet probability tagging, we use the same method as used in the SECVTX tagging. Since the mistag rates have a considerable dependence on the jet kinematics, they are parameterized as a 6 dimensional tag rate matrix of the variables E_T , track multiplicity, $\sum E_T^j$, η, number of vertices and z position of primary vertex. This mistag matrix is constructed from the inclusive jet sample in the same way as SECVTX tagging. In Table 4.2, negative tag rate and its systematic uncertainty are shown. Of course, the jet probability distribution for light flavor is flat. Thus the jet probability cut threshold is almost equivalent to the negative tag rate. The mistag asymmetry of Jet Probability tag is calculated with basically same way as SECVTX.

4.5 Neural Network b-Tagging

The SECVTX b-tagging exploits the long lifetime of b hadrons. c hadrons also have fairly long lifetime and secondary vertices in c-jets are frequently tagged. Therefore jets tagged by SECVTX are contaminated by false tagged light flavor (uds or gluon) jets or c jets. b-tagging with neural

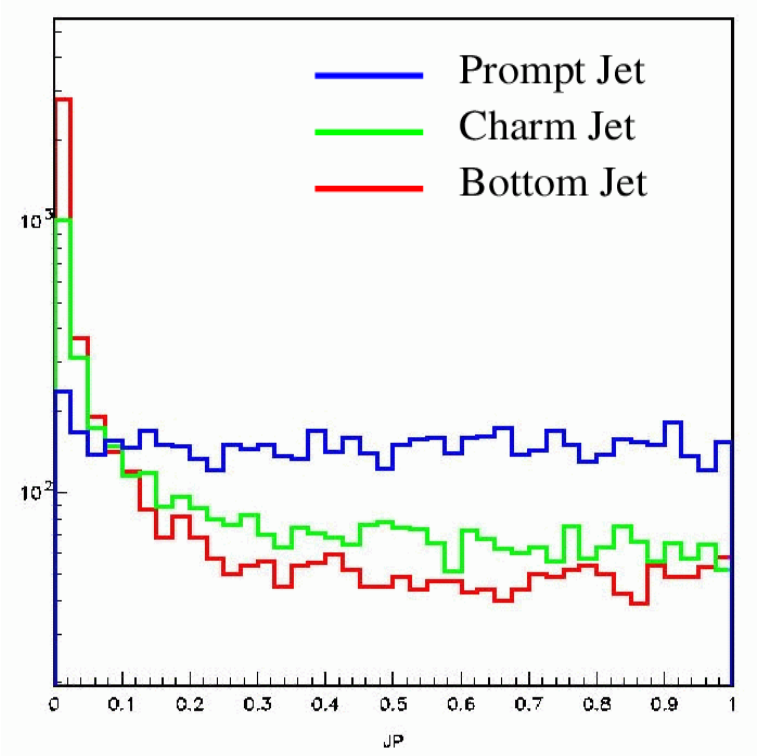

Figure 4.7: Jet Probability distribution for jets matched to b, c and light quarks in Monte Carlo simulated events.

Operation point	$< 5\%$	$< 1\%$
Negative tag rate (%)	5.194$\pm$0.004(stat)	1.218$\pm$0.002(stat)
Systematic uncertainty (%)	2.9	4.9

Table 4.2: Negative tag rate of jet probability for two cut thresholds.

network (NN) is developed to improve the purity of SECVTX b-tagging. The JETNET package [51] is used in this neural network. The detail principle of neural network with JETNET is described in the chapter 6. The NN b-tagging consists of two trained NN. One is trained to optimize the separation between b-jet and l-jet. Another is trained to optimize the separation between b-jet and c-jet. The accepted jets are satisfying the selection criteria of this two NN outputs. The NN b-tagging algorithm is applied to only jets tagged by SECVTX algorithm. The current NN b-tagging is tuned to increase the purity of the SECVTX b-tagged jets, not to increase the tagging efficiency.

The selected input variables are 16 listed in Table 4.3. These variables are chosen based on the properties of b jet that have higher track multiplicity, larger invariant mass, longer lifetime and a harder fragmentation function than c and l jets. The track parameters and L_{xy} significance are good discriminators for b-jets. The vertex p_T and mass of vertex are useful variables for identifying l jets, however c jets have p_T spectra similar to b jets. Pseudo-$c\tau$, the vertex fit χ^2 and jet probability also are the best discriminators. The output of the two neural networks are shown in Figure 4.9.

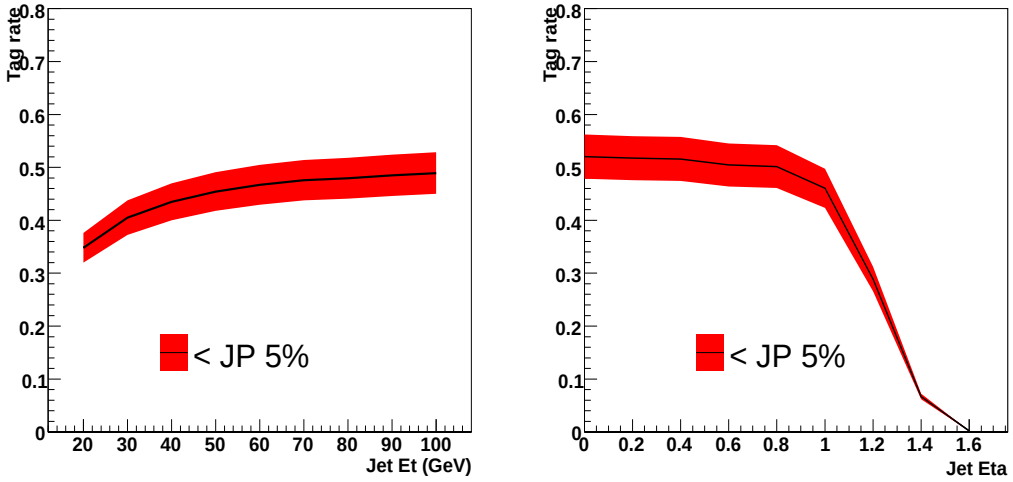

Figure 4.8: The Jet Probability tagging efficiency as a function of E_T (Left), and η (Right) in Higgs Monte Carlo simulated events. The efficiency is obtained by multiplying the tag rate for jet matched to b quarks using $\Delta R < 0.4$. The scale factor is applied and the band represents the systematic uncertainty on the scale factor.

The $b - l$ neural network training is performed with 10 hidden nodes and one output node. The $b - c$ neural network training is performed with 12 hidden nodes and one output node. The 16 input variables are active for both neural network. We tune the selection criteria for 90% b efficiency after SECVTX b-tagging, corresponding to a value of $\mathrm{NN}_{bl} > 0.182$ and $\mathrm{NN}_{bc} > 0.242$. At these cut values, the NN flavor separator rejects 65% of light flavor jets and 50% of the c jets while keeping 90% of b jets tagged by SECVTX algorithm.

The NN b-tagging is validated by comparing the performance on data and MC events. The heavy flavor enriched data with an electron candidate with $E_T > 8$ GeV are compared to MC. Figure 4.10 (left) shows the difference of performance between MC and data. The small difference is reflected as scale factor. The scale factor measured from the electron sample is 0.97$\pm$0.02. This scale factor is additionally applied to SECVTX scale factor because all of the jets under consideration have already been tagged by SECVTX.

The rejection performance is validated using negative tagged events for data and MC. Figure 4.10 (right) shows the comparison between data and MC. The distribution shows the good agreement between data and MC. The rejection factor is calculated from the average of some datasets and MC samples. The difference of each sample is taken into account as systematic uncertainty. The estimated rejection factor is 0.35$\pm$0.05. This value is applied to estimate mistag background. We also measured well-known $t\bar{t}$ cross section using this NN flavor separator [52] and confirmed the the consistent value is obtained compared to other analysis.

SECVTX variables	SECVTX independent variables
Number of tracks in associated with vertex	Number of tracks
Vertex fit χ^2	Jet Probability
Transverse decay length (L_{xy})	Reconstructed mass of pass 1 tracks
L_{xy} significance ($L_{xy}/\sigma_{L_{xy}}$)	Reconstructed mass of pass 2 tracks
Pseudo-$c\tau$ ($L_{xy} \times M_{vtx}/p_T^{vtx}$)	Number of pass 1 tracks
Vertex Mass $\left(\sqrt{(\sum \lvert\boldsymbol{p}_{vtx}\rvert)^2 - (\sum \boldsymbol{p}_{vtx})^2}\right)$	Number of pass 2 tracks
$p_T^{vtx}/(\sum_{tracks} p_T)$	$\sum_{tracks(pass1)} p_T/p_T^{jet}$
Vertex pass number (pass 1 or pass 2)	$\sum_{tracks(pass2)} p_T/p_T^{jet}$

Table 4.3: Input variables in the NN b-tagging. The variables in the first column are properties of the secondary vertex, while the variables in the second column are independent properties for identified secondary vertex.

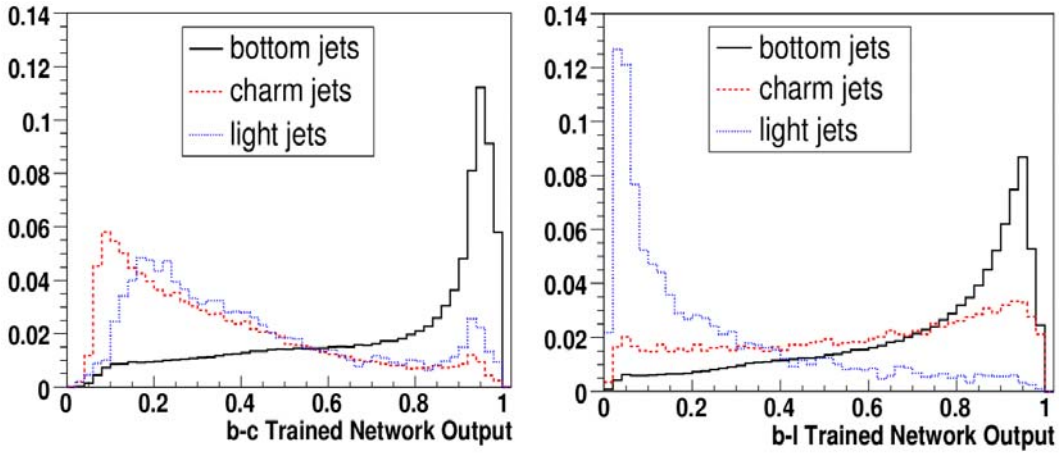

Figure 4.9: Neural network outputs obtained from trainings of bottom vs. charm jets (left) and bottom vs. light jets (right). Output distributions for bottom, charm and light jets are shown in solid, dashed, and dotted lines, respectively.

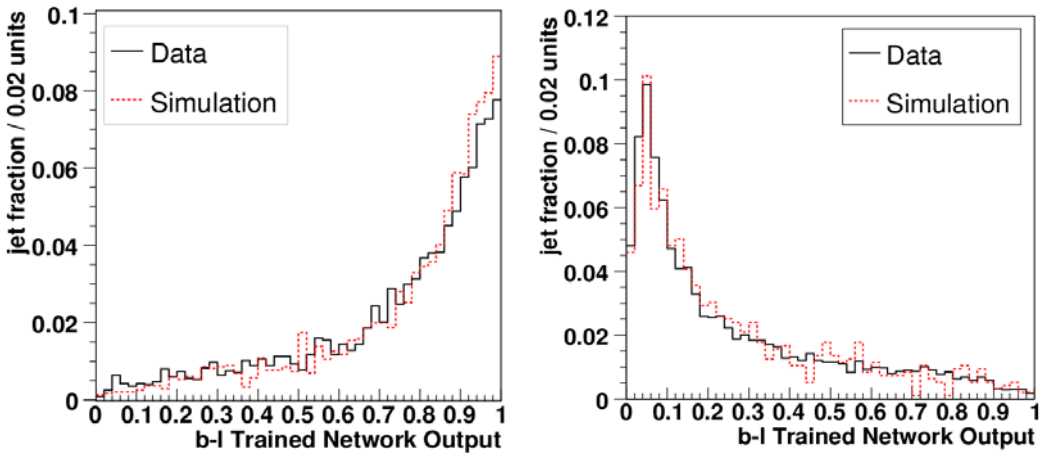

Figure 4.10: Comparisons of NN b-tag output in data (solid line), and Monte Carlo (dashed line) for SECVTX-tagged heavy-flavor-enriched jets (left) and tagged light flavor jets (right).

Chapter 5

Event Selection and Data Set

As discussed in the previous Chapter, Higgs boson production cross section is much smaller than the QCD background. In this Higgs search in the low mass Higgs region, we select $WH \to \ell\nu b\bar{b}$ candidates, not direct production $H \to b\bar{b}$ candidates, to enhance signal to background ratio. The event selection for the Higgs signal is described in this chapter. In the last section, we describe data set and MC samples to simulate the signal and background events.

5.1 Event Reconstruction

The data collected with the CDF detector are reconstructed to obtain the involved physics objects using the tracks from tracking system, the calorimeter energy deposition and the muon chamber stubs. WH production has the following signatures:

- Lepton from the W boson leptonic decay
- Neutrino from the W boson leptonic decay
- b quark jets from the Higgs boson decay

As the lepton from the W boson decay has high p_T, its signature is clean. Hence these signatures are used as the event trigger described in the previous chapter. We first look for an electron or a muon in this events. The signature of neutrino is large missing transverse energy ($\not\!\!E_T$) since the neutrino cannot be detected directly in the CDF detector. The missing transverse energy is estimated from the imbalance of total transverse energy. The reconstructed jets are examined if they pass b-jet criteria.

5.1.1 Offline Selections

Event selection criteria for each physics object (electron, muon, jet and $\not\!\!E_T$) and other selection applied in offline are summarized here.

At first, we require that the detector condition were good. The data taken while any critical sub-detector in this analysis was not working are rejected in this step. The interaction points should be in luminous region, $|z_0| < 60$ cm from the center of detector. The data has to pass the high-p_T lepton trigger described in previous chapter.

There can be multiple some electron and muon candidates in an event which passed the trigger. The lepton identification criteria is applied for these electron (CEM) and muon (CMUP, CMX) candidates. The selected lepton is required to have its z-vertex close to primary z-vertex, $|Z_{prim} -$

$Z_{lepton}| < 5$ cm. The event may include a second lepton which is not required to pass the isolation cut. It can be an electron in the plug region or a muon of CMU, CMP only or stubless. We require exactly one lepton (CEM, CMUP and CMX) passing the identification criteria to reduce dilepton background from top-dilepton events. In the selected events, contamination of Z events still remains. Therefore Z boson veto is applied by requiring that the invariant mass reconstructed from the primary lepton and the second object is not in the Z boson mass region $76 < m_Z < 106$ GeV/c^2. Missing transverse energy greater than 20 GeV is required for the W boson identification. In the next step, jet selections are applied: Observed jets E_T corrected by the jet energy correction be greater than 20 GeV and the absolute value of η be less than 2 in the silicon detector coverage. The events with $W+$ exact two jets are used as signal candidates of $WH \to \ell\nu b\bar{b}$. The other W + njets events (n $\neq$ 2) are analyzed as control samples. Especially W + 1jet events are important to verify and estimate the background. W + 3 or more jets events are also important because they are dominated by $t\bar{t}$ background.

Additionally, the SECVTX b-tagging algorithm as discussed in the previous chapter is applied to jets. At least one jet in an event has to pass the b-tagging and identified as a b-jet. This can reduce the huge W+jets background. The events before applying any b-tagging are called "pretag" events, and are important to verify the W + jets background shape.

5.1.2 b-Tagging Strategy

We use at least one b-tagged events as signal candidates. The double b-tagged events has good signal-to-background ratio though the disadvantage of double b-tagged events is the small event rate due to the b-tagging efficiency. We improve the sensitivity by increasing the double tag acceptance employing both SECVTX and Jet Probability b-tagging. We extract the double b-tagged events from the one SECVTX b-tagged event sample, as Jet Probability b-tagging is less efficient in reducing background than SECVTX b-tagging algorithm.

The rest of one SECVTX tagged events still has large signal acceptance but the signal-to-background ratio is worse than double b-tagged events. Thus we apply NN b-tagging to the rest of one SECVTX tagged events to improve signal-to-background ratio. Finally the following double b-tagged events and one b-tagged events with NN are analyzed:

SECVTX tight + SECVTX tight (ST+ST): Events in this category are required to have both jets tagged by the tight operating point of SECVTX.

SECVTX tight + Jet Probability (ST+JP): Events in this category are required to have jet tagged by the tight operating point of SECVTX and another jet tagged by the jet probability algorithm. To be tagged, the jet must have a jet probability of less than 5%.

One SECVTX tight with NN b-tagging: Events in this category are required to have jet tagged by the tight operating point of SECVTX. To improve signal-to-background ratio, NN b-tagging is applied to the jet tagged by SECVTX.

ST+ST double tag category is the first choice due to the highest purity. If SECVTX b-tagging for the second jet fails, the jet probability b-tagging is applied. The events failed both double tag criteria are candidates of one tag category. We use the events passed NN b-tagging requirement into one SECVTX tagged events.

5.2 Dataset and MC Sample

The dataset used in this analysis were collected from February 2002 to May 2007. The corresponding total integrated luminosity to high p_T electron or muon datasets is

- $1.92\,\mathrm{fb}^{-1}$ for CEM and CMUP leptons,
- $1.88\,\mathrm{fb}^{-1}$ for CMX muons.

The CMX detector was not operated until August 2002 since CMX trigger was disable due to trigger bandwidth limitation at high luminosity. CMX trigger after adding jet requirement is available in any luminosity range. W + Higgs signal and the background kinematics are simulated with Monte Carlo (MC) generator, PYTHIA [53], ALPGEN [55], MADEvent [56], The MC parameters were tuned for CDF experiment [54]. Among these ALPGEN is used to generate W+n parton events. The EvtGen [57] decay tables are interfaced to provide proper modeling of b and c hadron decays.

W+Higgs process is less important in the high mass region ($m_h > 135$ GeV/c^2) where the $gg \to H \to WW$ channel is the main search channel. The current lower limit at 95% confidence level is 114.4 GeV/c^2 obtained at LEP2 [18]. Therefore W+Higgs signal samples are generated for Higgs mass points in the our search region ($m_h = 110 - 150$ GeV/c^2).

Chapter 6

Neural Network Discriminant

6.1 Introduction to Neural Network

To further improve the signal to background discrimination after event selection, we employ an artificial Neural Network (NN) trained on a variety of kinematic variables to distinguish the W+Higgs events from backgrounds. We use JETNET neural network program [51] interface to ROOT [58].

The type of artificial neural network used for this analysis is a feedforward network. It is connected to neuron in laminae and has no feedback from the neuron of output side to the neuron of input side. Figure 6.1 shows a schematic view of feedforward Neural Network structure.

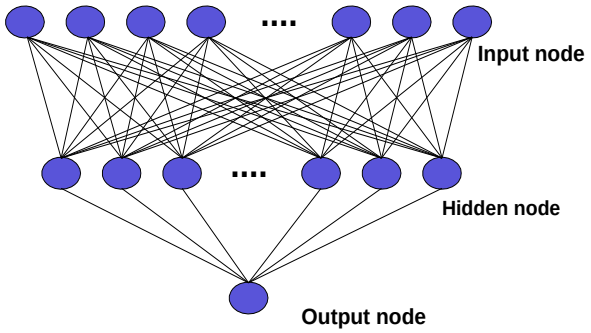

Figure 6.1: The schematic view of Neural Network structure.

This neural network can be multilayer. The nodes of input(output) layer are called input(output) nodes, the nodes of intermediate layers are called hidden nodes. The number of intermediate layers is the arbitrary but normally one hidden layer is enough to optimize physics process. The number of hidden nodes is also arbitrary. This number is optimized in the following section.

In the neural network model each individual node is represented by

$$O_j(i) = f(I_j(i)), \quad j = 1, \cdots, n(i), \quad i = 2, \cdots, l$$

and the j-th input is calculated by

$$I_j(i) = \sum_k w_{kj}(i-1) O_k(i-1) + \theta_j, \quad k = 1, \cdots, n(i-1)$$

where $O_j(i)$ is an output of the j-th nodes of the i-th layer. $I_j(i)$ is an input for the j-th nodes of the i-th layer. w_{kj} is the strength of connection between nodes called weight. θ_i is the threshold and arbitrary parameter, f(x) is the sigmoid function shown in Figure 6.2 defined by

$$f(x) = \frac{1}{1 + \exp(-x)}$$

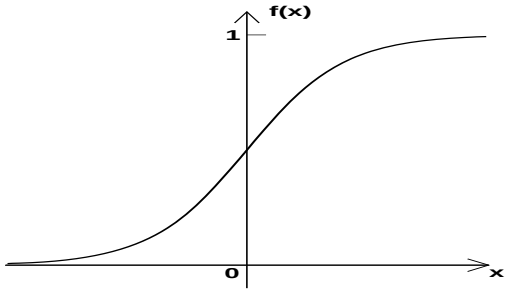

Figure 6.2: The sigmoid function used in artificial neural network.

The weight $w_{kj}(i)$ is changed and optimized during the training process of neural network. The training of the neural network uses several input samples and their desired input/output. When M dataset is given as follows,

$$(x_{id}, s_{jd}), \quad i = 1, \cdots, l, \quad j = 1, \cdots, n(l), \quad l = 1, \cdots, M$$

The output of this neural network, $z_j(l)$, for input x_{id} is optimized by changing weight $w_{kj}(i)$ as the output is closing to desired output s_{jd}. We consider the following error function to do it.

$$E = \frac{1}{2M} \sum_{d=1}^{M} \sum_{j=1}^{n(l)} (z_{jd}(l) - s_{jd})^2$$

The weights $w_{kj}(i)$ are determined by minimizing this error function. There are some learning algorithms to minimize this function. The back-propagation method [59] is applied in this analysis.

6.2 Training and Structure of the Neural Network

To optimize the NN, we use an iterative procedure to determine the configuration which best discriminates signal from the background, and which uses a minimal number of input discriminants [22]. This is done by first determining the best one-variable NN from a list of 76 possible choices considered from two jets, $\not\!\!E_T$ and lepton kinematics and correlation of them. The optimization algorithm keeps this variable as an input and then loops over all other variables to determine the best two-variable NN. The best N-variable network is finally selected once the N+1-variable network shows less than 0.5 percent improvement. The criteria for comparing networks is the testing error defined by how often an NN with a given configuration correctly classifies several thousand signal and background events.

We used the optimal structure of input variables to train separate neural networks for Higgs masses of 110, 115, 120, 130, 140, and 150 GeV/c^2. Re-training networks with the same structure and different signal masses keeps the neural network sensitivity almost constant against the

Higgs mass. We expect that this has increased the sensitivity for these Higgs masses. Further studies could investigate whether other combinations of input variables becomes more powerful at different Higgs masses.

Our final Neural Network configuration has 6 input variables, 11 hidden nodes, and 1 output node. The 6 optimal inputs are,

M_{jj+}**:** This variable is the invariant mass calculated from the two jets using. Furthermore, if there are additional loose jets present ($E_T > 12$ GeV and $|\eta| < 2.4$), the loose jet that is closest to one of the two jets is included in this invariant mass calculation, if the separation between that loose jet and one of the jets is $\Delta R < 0.9$.

$\sum E_T$**(Loose Jets):** This variable is the scalar sum of the loose jet transverse energy.

p_T **Imbalance:** This variable expresses the difference between the scalar sum of the transverse momenta of all measured objects and the $\not\!\!E_T$. Specifically, it is calculated as $P_T(jet_1) + P_T(jet_2) + P_T(lep) - \not\!\!E_T$.

$M_{l\nu j}^{min}$**:** This is the invariant mass of the lepton, $\not\!\!E_T$, and one of the two jets, where the jet is chosen to give the minimum invariant mass. For this quantity, the p_z component of the neutrino is ignored.

ΔR**(lepton-**ν_{max}**):** This is the ΔR separation between the lepton and the neutrino, where the p_z of the neutrino is taken from by choosing the solutions from the quadratic equations for the W mass (80.42 GeV/c^2 [65]) constraint with the largest $|p_z|$.

$P_T(W + H)$**:** This is the total transverse momentum of the W plus two jets system, $P_T(\vec{lep} + \vec{\nu} + \vec{jet}_1 + \vec{jet}_2)$.

6.3 Input Variables and Output Results of Neural Network

Figure 6.3 shows the comparison plots between the NN inputs for signal and background samples where each distribution is normalized to one. Figure 6.4 shows the shape comparison between the NN outputs. The s-channel single top background is not yet applied for this neural network training while it is a relatively large background in double b-tagging categories. These neural network input variables and output variables are validated whether they are well-modeled in the MC samples and in the CDF data control and signal candidates samples.

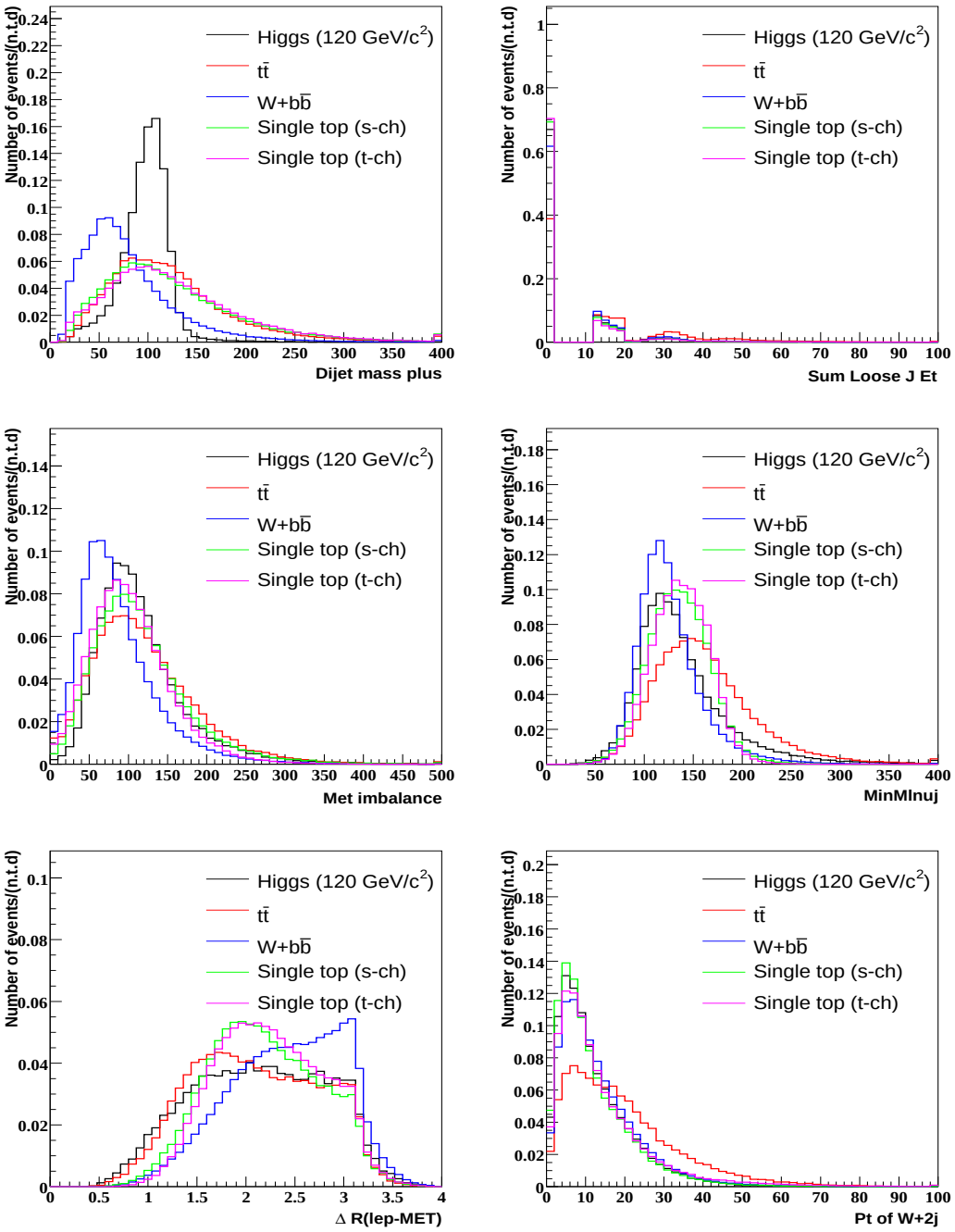

Figure 6.3: Comparison of NN input variable kinematics for signal ($m_h = 120$ GeV/c^2) and major backgrounds. Each histogram is normalized to unit area.

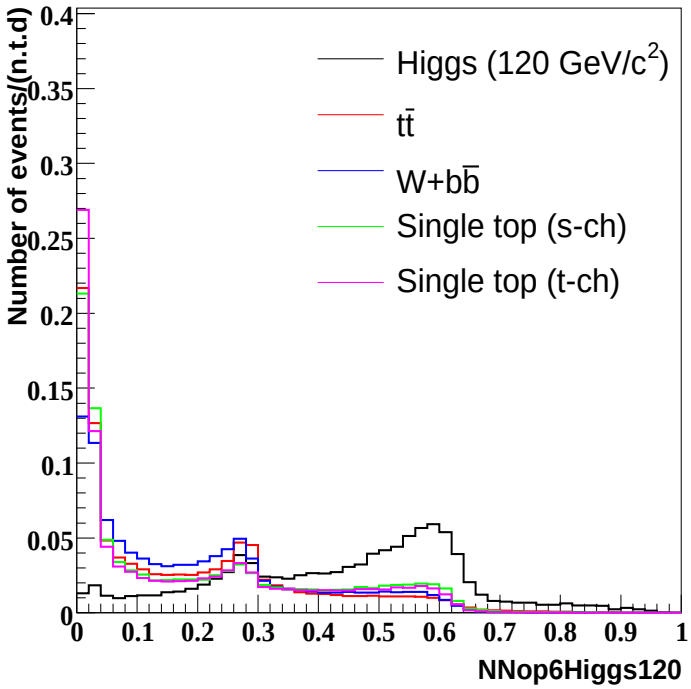

Figure 6.4: Comparison of NN output for signal ($m_h = 120$ GeV/c^2) and major backgrounds. Each histogram is normalized to unit area.

Chapter 7

Background Estimation

In this chapter, our method of the background estimation is discussed in detail. The final state of the $WH \to \ell\nu b\bar{b}$ signal process has one high p_T lepton, large $\not\!\!E_T$ and two jets. This final state is very similar to that of the top quark pair production in W + 3 or more jets. While the signature is different, W + 1 jet events are dominated by QCD and W+jets which may fake the signal. The background estimation is performed for W + n jet ($n \geq 1$) events since other jets events are good control region. The following background sources for the $WH \to \ell\nu b\bar{b}$ signal are considered:

Non-W QCD: a W signature is generated when one jet fakes a high p_T lepton and $\not\!\!E_T$ is generated through jet energy mismeasurement.

W + Mistags: this background occurs when one or more light flavor jets produced in association with a W boson are mistakenly identified as a heavy flavor jet by the b-tagging algorithms. Mistags are resulting from the finite resolution of the tracking, from material interactions, or from long-lived light flavor hadrons (Λ and K_s) that produce displaced vertices.

W+ Heavy Flavor: these processes ($W + b\bar{b}$, $W + c\bar{c}$ and $W + c$) involve the production of actual heavy flavor quarks in association with a W boson.

Top Quark Backgrounds: this background comes both from single top quark production and top quark pair production.

Other EWK Backgrounds: additional small background contributions come from Z + jets production and diboson (WW, WZ, and ZZ) production.

In the following sections, more details are described for each background.

7.1 Non-W (QCD fake) Background

Jet events sometimes mimic the W boson signature when an energetic hadron jet may pass the lepton selection criteria or a heavy flavor hadron can produces the lepton via its semileptonic decay. Similarly the large missing E_T can come from the mismeasurements of energy or the semileptonic decay of a heavy flavor hadron. Such a background source is difficult to estimate since modeling of detector response is unreliable and the heavy flavor content is not well predicted.

Generally, non-W events generate a non-isolated "lepton" and small missing transverse energy. Assuming non-correlation between isolation of lepton and missing $\not\!\!E_T$, side band region events are used to extrapolate the expected non-W background in the signal region. To estimate

such a non-W background, two dimensional plane of the isolation and the $\not\!\!E_T$ is used. We divide the data sample into the following four regions in the $\not\!\!E_T$ vs isolation plane (see Figure 7.1,7.2):

- Region A: Isolation > 0.2 and $\not\!\!E_T < 15$ GeV
- Region B: Isolation < 0.1 and $\not\!\!E_T < 15$ GeV
- Region C: Isolation > 0.2 and $\not\!\!E_T > 20$ GeV
- Region D: Isolation < 0.1 and $\not\!\!E_T > 20$ GeV

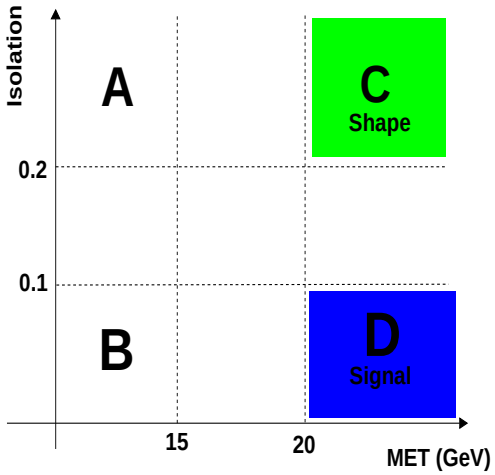

Figure 7.1:$\not\!\!E_T$ and lepton isolation plane.

Here Region D is our signal region. We assume that the lepton isolation is independent of $\not\!\!E_T$, and that the tagging efficiency is the same in Region B and D. Then we define the fraction of non-W events by :

$$f_{\mathrm{non}-W} = \frac{N_B \times N_C}{N_A \times N_D}, \tag{7.1}$$

where N_D is the number of pretag events in the signal region and N_i $(i = A, B, C)$ are the number of pretag events in the corresponding sideband region. To obtain the non-W background for tagged events, we measure the b-tagging efficiency from Region B. For this purpose, we define b-tagging efficiency as

$$r_B = \frac{N_B^{(\text{tagged events})}}{N_B^{(\text{taggable jets})}}, \tag{7.2}$$

where $N_B^{(\text{tagged events})}$ and $N_B^{(\text{taggable jets})}$ are the numbers of tagged events and taggable jets in Region B, respectively. Then we obtain the number of non-W background events in Region D from the relation

$$N_D^{(\mathrm{non}-W)} = f_{\mathrm{non}-W} \times r_B \times N_D^{(\text{taggable jets})}. \tag{7.3}$$

We call this procedure the "Tag Rate Method" since it uses the tag rate in Region B. It is also possible to have an estimate directly from the tagged sample, by using

$$N_D^+ = \frac{N_B^+ \times N_{C'}^+}{N_{A'}^+}, \tag{7.4}$$

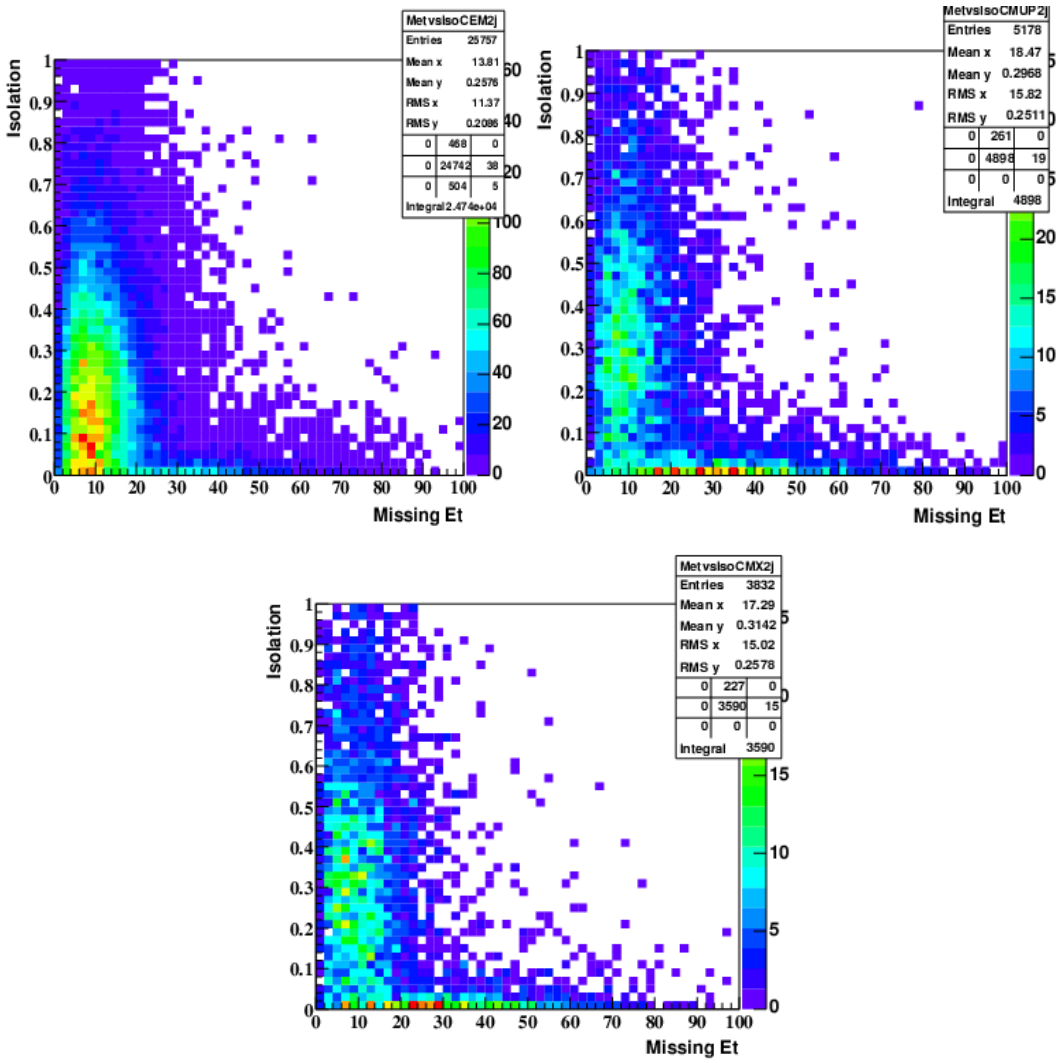

Figure 7.2: Observed data on $\not\!\!E_T$ vs isolation plane for CEM (top left), CMUP (top right) and CMX (bottom). These events have a high p_T lepton and exactly 2 tight jets.

where $+$ denotes positive tagged events, and we call this method as "Tagged Method". Region A and C are extended to A' (Isolation > 0.1 and $\not\!\!E_T < 15$ GeV) and C' (Isolation > 0.1 and $\not\!\!E_T > 20$ GeV) to increase statictics after b-tagging.

These methods are data-based techniques, so the estimates could also contain other background processes. Subtracting the known backgrounds should result in a better non-W QCD estimate. The contributions from $t\bar{t}$ and W+jets events to each sideband region are estimated and subtracted based on the theoretical cross section and the ratio to Region D. The non-W fractions after the correction are shown in Table 7.1. Systematic uncertainty on the non-W fraction of 25% are quoted from the previous analysis [21],

To combine the estimates from the tag rate method and the tagged method, we calculate a weighted average of the sum to obtain the total non-W backgrounds.

The low statistics of the double b-tagged or after applying NN tagging samples prevents us from applying this technique directly. Instead, estimates from at least one b-tagged sample are

Njets	1jet	2 jet	>= 3jet
Electron (CEM)	0.236±0.059	0.251±0.063	0.251±0.065
Muon (CMUP,CMX)	0.056±0.014	0.067±0.017	0.058±0.016

Table 7.1: Non-W fraction in each jet bin. 3 or more jet events are merged into one bin due to statistical limitation. Two muon types are also merged for statistical limitation.

extended into the double b-tagged sample using the ratio of events with at least one tag to events with double tag or after NN tag in Region A' (Isolation > 0.1 and $\not\!\!E_T < 15$ GeV), B, and C' (Isolation > 0.1 and $\not\!\!E_T > 20$ GeV). We take a weighted average of these ratios in each region as the double tag or after NN tag ratio.

7.2 W + Heavy Flavor Production

The $Wb\bar{b}$ and $Wc\bar{c}$ productions are major sources of background in the b-tagged W+jets channel. They are estimated primarily using the leading order Monte Carlo generator, ALPGEN [55]. The contribution from heavy flavor production in W+jets events is determined from the heavy flavor fraction and the tagging efficiency for those events generated by Monte Carlo. The heavy flavor fraction is estimated from the ratio of the number of W + heavy flavor (HF) jet events to the number of W + jets (heavy flavor + light flavor) events after removing the double counting problem which comes from overlapping phase spaces in W + n parton with parton shower and W + n+1 parton samples.

The heavy flavor fractions estimated in ALPGEN have been calibrated using W + 1 jet events from real data. The scale factor (k-factor) to explain the difference between data and MC is measured. Unit k-factor is ideal, however it is larger than 1 due to incorrect modeling of gluon splitting in the Monte Carlo and higher order effects. The k-factor (KF) is defined by

$$KF \equiv \frac{F^b_{j,data}}{F^b_{j,MC}}$$

where $F^b_{j,data}$ and $F^b_{j,MC}$ are the W+b-jets fractions in data and MC, respectively. To calibrate this k-factor, we convert it to

$$KF = \frac{F^b_{tag,data} \times F^{tag}_{j,data}}{F^{btag}_{j,MC} \times SF}$$

where SF is b-tagging scale factor and $F^{btag}_{j,MC}$ is the fraction of the tagged b jets in the MC sample and $F^{tag}_{j,data}$ is the one in W + 1 jet events of data. $F^b_{tag,data}$ is the fraction of tagged real b-jet in all tagged jets in W + 1 jet data events. This last fraction can be extracted by fitting a sum of the b, c and light flavor jet templates from Monte Carlo to W + 1 jet data with the vertex mass distribution reconstructed from tracks in the jet and Karlsruhe neural network flavor separator [60]. This method is capable of calculation of fraction by considering each fraction as free parameter. Other two fractions are obtained from MC and data, respectively. The uncertainties in these factors are taken conservatively to be 40% by considering the difference between b and c, their E_T and the number of jets depencences and the difference vertex mass and NN output fitting. The k-factor was found to be 1.4 ± 0.4. After adding this k-factor into account, heavy flavor fractions are corrected as shown in Table 7.2.

Table 7.3 and 7.4 show the heavy flavor tagging efficiency results in these b-tagging categories. The tagging efficiency is estimated using W+jets MC samples. The heavy flavor fractions and tagging efficiencies are multiplied by the number of pre-tagged events in data, after the number of pre-tagged events has been corrected for the non-W and other background contributions.

$$N_{W+HF} = f_{HF} \cdot \epsilon_{\rm tag} \cdot [N_{\rm pretag} \cdot (1 - f_{\rm non-}W) - N_{\rm EWK}] \,, \tag{7.5}$$

where f_{HF} is the heavy flavor fraction, $\epsilon_{\rm tag}$ is the tagging efficiency, $f_{\rm non-}W$ is the non-W fraction discussed in the previous section, and $N_{\rm EWK}$ is the expected number of $t\bar{t}$ and electroweak background events.

	1 jet	2 jet	3 jet	>=4 jet
$Wb\bar{b}$ (1b)	1.0±0.4	2.0±0.8	3.4±1.4	4.6±2.0
$Wb\bar{b}$ (2b)		1.3±0.6	2.5±1.0	3.1±1.8
$Wc\bar{c}$ (1c)	7.7±2.4	12.2±4.5	16.4±5.3	18.6±6.9
$Wc\bar{c}$ (2c)		2.0±0.8	4.6±1.8	8.4±3.4

Table 7.2: Heavy flavor fraction in unit of %. The uncertainty includes systematics which is dominated by Q^2 variation in MC generation and k-factor 1.4 ± 0.4, where 1b (1c) means that one of the observed jets match to true b (c) hadron and 2b (2c) means two observed jets match to true b (c) hadrons.

One SECVTX w/ NN tag	1 jet	2 jet	3 jet	>=4 jet
$Wb\bar{b}$ (1b)	27.5 ± 1.5	28.1 ± 1.3	26.7 ± 1.4	26.9 ± 3.7
$Wb\bar{b}$ (2b)		26.2 ± 1.2	24.1 ± 1.2	22.6 ± 1.3
$Wc\bar{c}$ (1c)	4.2 ± 0.2	4.6 ± 0.3	4.9 ± 0.3	5.2 ± 0.7
$Wc\bar{c}$ (2c)		6.3 ± 0.4	6.6 ± 0.4	6.9 ± 0.6

Table 7.3: Heavy flavor tagging efficiency (%) calculated from ALPGEN W+jets MC for one SECVTX w/ NN tag. Here 1b, 1c means one of the observed jets matches to true b or c hadron and 2b, 2c means two observed jets match to true b or c hadron.

Double SECVTX	2 jet	3 jet	>=4 jet
$Wb\bar{b}$ (2b)	16±2	19±2	19±3
$Wc\bar{c}$ (2c)	1±0	2±0	2±1
SECVTX + Jet Probability(5%)	2 jet	3 jet	>=4 jet
$Wb\bar{b}$ (2b)	10.1±1.2	11.1±1.3	12.4±1.5
$Wc\bar{c}$ (2c)	1.6±0.2	2.3±0.3	3.2±0.4

Table 7.4: Heavy flavor tagging efficiency (%) calculated from ALPGEN W+jets MC for double tagging categories. Here 1b, 1c means one of the observed jets matches to true b or c hadron and 2b, 2c means two observed jets match to true b or c hadron.

7.3 W + Light Flavor/Gluon Jets (Mistags)

A light flavor/gluon jet can be misidentified as a b jet by the b-tagging algorithm. It is called "mistag". The mistag is caused by a random overlap of tracks which are displaced from the primary vertex due to finite tracking resolution and the contribution of long lived light flavor, K_S, Λ decay, and the material interaction. It is unreliable to simulate with the MC. This background is measured directly from jet data samples.

This background effect is estimated from the mistag matrix parameterized as discussed in Chapter 4. The mistag probability per jet can be calculated from the mistag matrix. The mistag probability per event is obtained as a sum of the mistag probabilities per jet over jets in an event. This sum is performed for all jets which have a tagability ($\geq$ 2 silicon tracks). Finally the number of mistag background events is estimated by summing up the mistag probability per event for all events.

$$N_{mistag} = \sum_{n=event} \sum_{j=jet(n)} \mathcal{P}_j^{mistag}$$

This calculation of at least one mistag event is performed with respect to the events before applying the b-tagging. The mistag calculation in double tag categories is performed with respect to exactly one SECVTX tagged W+jet events. For W+jets events this corresponds to estimate one b-tag plus at least one mistag events. It also includes double mistag events if one b-tagged jet is tagged falsely. Figure 7.3 illustrates our mistag background calculation scheme.

The systematic uncertainty of mistag matrix is coming from the sample dependence, having $\sum E_T$ bias and trigger bias. The deviation from the predicted mistag rate independent samples are taken as the systematic uncertainties. After considering run dependence, we obtained total 6.6% error for mistag matrix. This procedure is based on the formar analysis [61]. We obtain the uncertainties of mistag background after taking the uncertainties of mistag asymmety into account.

For jet probability (ST+JP) categories, mistag matrix [62] is applied like SECVTX tag. The uncertainty is calculated in same procedure as SECVTX tag [63]. The estimated total uncertainty from Jet probability mistag matrix is 2.9%.

These mistag matrix and asymmetric factor are calibrated in $t\bar{t}$ cross section measurement [61,62]. For the mistag background after applying neural network, the rejection factor (0.35$\pm$0.05) is applied to one SECVTX mistag background as discussed in chapter 4.

7.4 Other Backgrounds

The normalizations of the diboson, $t\bar{t}$ and single top backgrounds are based on the theoretical cross sections (listed in Table 7.5). The acceptance and the b-tagging efficiency are derived from the MC. The MC acceptance is corrected for lepton identification efficiency, the trigger efficiency and the z vertex cut efficiency. The b-tagging efficiency is scaled by the MC/data scale factor. The expected number of events is obtained by the equation

$$N = \int \mathcal{L}dt \times \epsilon \times \sigma, \tag{7.6}$$

where ϵ is the total detection efficiency corrected by all of the scale factors, σ is the cross section and $\int \mathcal{L}dt$ is the integrated luminosity.

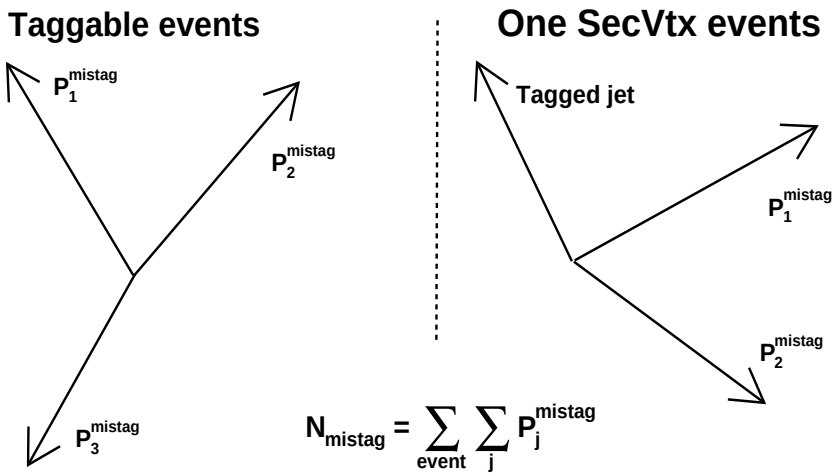

Figure 7.3: The schematic figure of mistag calculation using mistag probability in each tag. The one arrow means one jet. P mean the mistag probability assigned from mistag matrix estimation for each jet.

Theoretical Cross Sections	
WW	12.4 $\pm$ 0.25 pb
WZ	3.96 $\pm$ 0.06 pb
ZZ	1.58 $\pm$ 0.05 pb
Single Top s-channel	0.88 $\pm$ 0.11 pb
Single Top t-channel	1.98 $\pm$ 0.25 pb
$Z \rightarrow \tau\tau$	265 $\pm$ 30.0 pb
$t\bar{t}$	6.7 $^{+0.7}_{-0.9}$ pb

Table 7.5: Theoretical cross sections and errors for the electroweak and single top backgrounds, along with the theoretical cross section for $t\bar{t}$ at ($m_t = 175$ GeV/c^2). The cross section for $Z^0 \rightarrow \tau\tau$ is obtained from the direct CDF measurement [64].

7.5 Summary of Background Estimation

We have described the contributions of the individual background sources to the total background. We summarize the background estimates for one SECVTX w/ NN tag category, double SECVTX tag category (ST+ST) and one SECVTX tag + Jet probability tag category (ST+JP) in Tables 7.6, 7.7 and 7.8. The number of expected background events and the number of observed events in data as a function of jet multiplicity for three categories of one SECVTX w/ NN tag, double SECVTX tag (ST+ST) and one SECVTX tag + Jet probability (ST+JP) are shown in Figures 7.4,7.5 and 7.6, respectively.

Njet	1jet	2jet	3jet	>=4jet
Pretag Events	196160	32242	5496	1494
Mistag	236.7±19.36	107.1±9.38	41.84±3.84	20.97±1.91
$Wb\bar{b}$	431.7±182.4	215.6±92.34	61.78±24.68	26.14±10.43
$Wc\bar{c}$	514.4±154.7	167.0±62.14	45.40±15.31	17.71±6.86
$t\bar{t}$(6.7pb)	11.85±1.82	60.68±9.30	111.0±17.03	122.4±18.76
Single top(s-ch)	7.09±1.03	14.38±2.09	3.91±0.57	0.97±0.14
Single top(t-ch)	23.31±3.41	29.57±4.33	6.24±0.91	1.11±0.16
WW	7.21±0.89	15.45±1.91	4.61±0.57	1.03±0.13
WZ	5.52±0.59	7.59±0.81	1.76±0.19	0.48±0.05
ZZ	0.17±0.02	0.31±0.03	0.14±0.01	0.07±0.01
$Z \rightarrow \tau\tau$	14.58±2.25	7.27±1.12	2.39±0.37	0.71±0.11
nonW QCD	465±83.21	184.7±33.04	44.83±8.57	17.03±3.67
Total Bkg	1717.6±347.9	809.61±159.38	323.92±45.5	208.57±26.24
WH signal (120 GeV)	Control region	1.82±0.15	Control region	Control region
Observed Events	1812	805	306	215

Table 7.6: Background summary table of one SECVTX tag w/ NN tag category.

Njet	2jet	3jet	>=4jet
Pretag Events	32242	5496	1494
Mistag	3.88±0.35	2.41±0.24	1.62± 0.14
$Wb\bar{b}$	37.93±16.92	14.05±5.49	7.39± 2.93
$Wc\bar{c}$	2.88±1.25	1.52±0.61	1.15± 0.47
$t\bar{t}$(6.7pb)	19.05±2.92	54.67±8.38	94.93± 14.56
Single top(s-ch)	6.90±1.00	2.28±0.33	0.61± 0.09
Single top(t-ch)	1.60±0.23	1.43±0.21	0.50± 0.07
WW	0.17±0.02	0.15±0.02	0.16± 0.02
WZ	2.41±0.26	0.68±0.07	0.16± 0.02
ZZ	0.06±0.01	0.06±0.01	0.02±0.001
$Z \rightarrow \tau\tau$	0.25±0.04	0.19±0.03	0.06±0.01
nonW QCD	5.50±1.00	2.56±0.48	1.02± 0.22
Total Bkg	80.62±18.75	79.99±10.92	107.63± 15.15
WH signal (120 GeV)	0.94±0.11	Control region	Control region
Observed Events	83	88	118

Table 7.7: Background summary table of double SECVTX tag category.

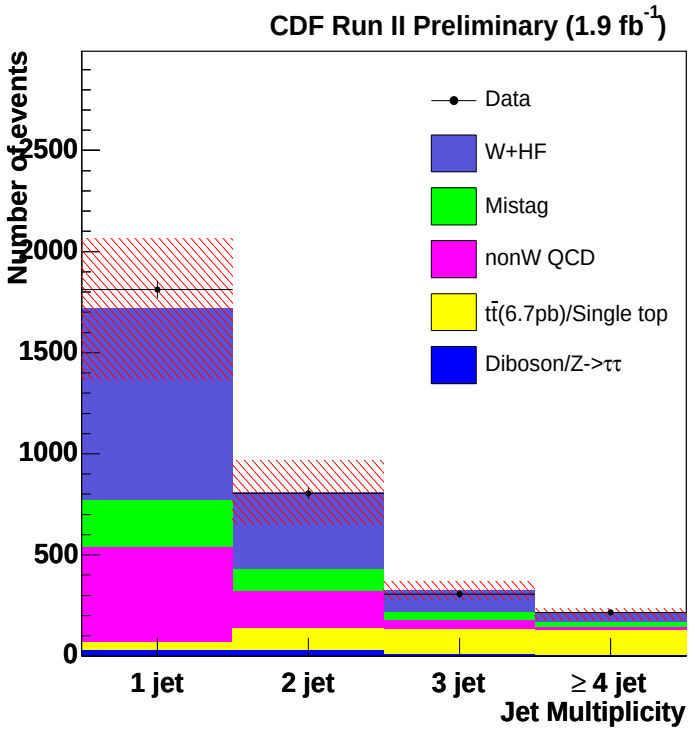

Figure 7.4: The numbers of observed one SECVTX tag w/ NN tag events and backgrounds as a function of jet multiplicity. Black points show observed events and each color means each estimated background. Red hash means background uncertainties.

Njet	2jet	3jet	>=4jet
Pretag Events	32242	5496	1494
Mistag	11.73±0.92	8.11±0.64	8.39±0.58
$Wb\bar{b}$	31.15±14.03	11.47±4.55	6.55±2.63
$Wc\bar{c}$	7.87±3.43	4.38±1.76	3.09±1.27
$t\bar{t}$(6.7pb)	15.56±2.39	47.48±7.28	79.81±12.24
Single top(s-ch)	5.14±0.75	1.90±0.27	0.53±0.07
Single top(t-ch)	1.87±0.27	1.49±0.22	0.44±0.06
WW	0.93±0.11	0.63±0.08	0.47±0.06
WZ	1.84±0.20	0.59±0.06	0.19±0.02
ZZ	0.08±0.01	0.04±0.003	0.02±0.002
$Z \rightarrow \tau\tau$	1.29±0.20	0.53±0.08	0.20±0.03
nonW QCD	9.55±1.73	4.87±0.93	1.80±0.40
Total Bkg	86.99±17.99	81.46±10.22	101.49±13.08
WH signal (120 GeV)	0.74±0.09	Control region	Control region
Observed Events	90	80	106

Table 7.8: Background summary table of one SECVTX tag + Jet probability tag category.

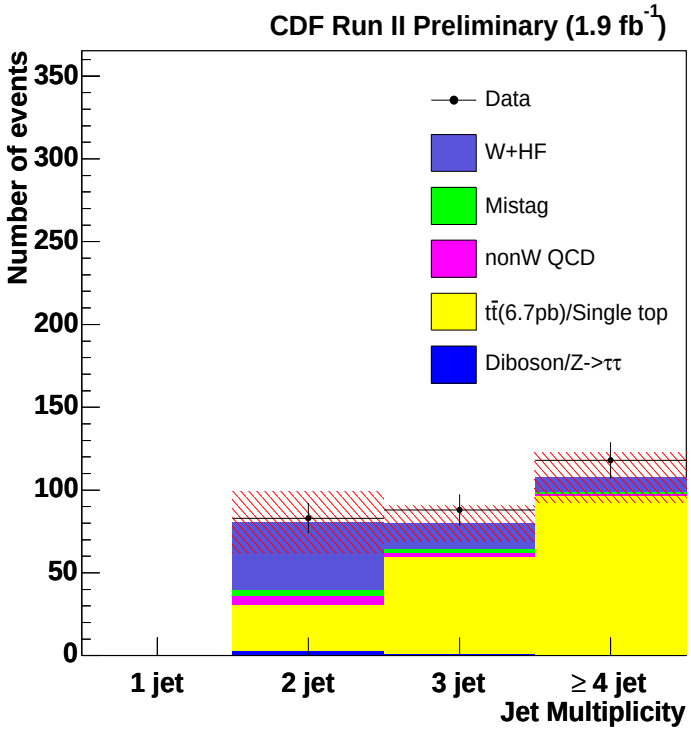

Figure 7.5: The numbers of observed double SECVTX tagged events and backgrounds as a function of jet multiplicity. Black points show observed events and each color means each estimated background. Red hash means background uncertainties.

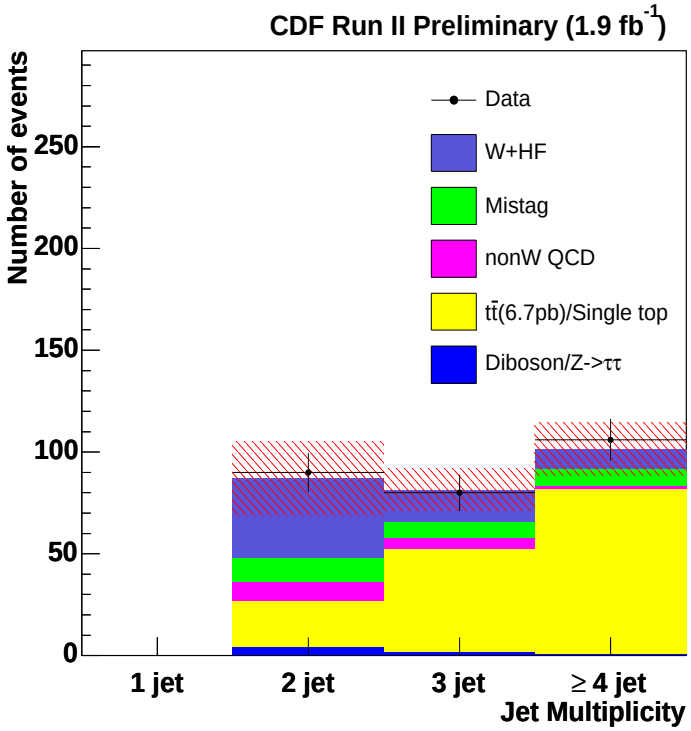

Figure 7.6: The numbers of observed one SECVTX and one Jet probability tagged events and backgrounds as a function of jet multiplicity. Black points show observed events and each color means each estimated background. Red hash means background uncertainties.

Chapter 8

Search for Higgs Boson Production in Association with a W Boson

In this chapter the signal acceptance and its systematic uncertainty on signal acceptance are estimated first. Secondly the expected number of signal events in the current dataset is estimated for each b-tagging category. Various kinematic shape distributions for each b-tagging category are examined whether the Standard Model background estimation is reasonable. Finally NN output distributions are checked to see the excess from the Standard Model background.

8.1 Higgs Signal Acceptance

The evaluation of the expected number of Higgs boson signal events is based on the leading order theoretical cross section and the branching ratio. Its dynamics is well defined within the Standard Model. The kinematics and the experimental effect are simulated using Monte Carlo generators, PYTHIA [53]. This search is evaluated as a function of Higgs mass. As discussed in the previous section, the search range is 110 - 150 GeV/c^2. The number of expected signal events is calculated from

$$N_{WH\to\ell\nu b\bar{b}} = \epsilon_{WH\to\ell\nu b\bar{b}} \cdot \int \mathcal{L}dt \times \sigma(p\bar{p} \to WH) \times BR(H \to b\bar{b})$$

where $\epsilon_{WH\to\ell\nu b\bar{b}}$ is the event detection efficiency, $\int \mathcal{L}dt$ is the integrated luminosity, $\sigma(p\bar{p} \to WH)$ and $BR(H \to b\bar{b})$ are the production cross section and the branching ratio, respectively. The integrated luminosity is described in section 4.2. The production cross section and the branching ratio of WH signal was shown in chapter 1 as a function of the Higgs mass. The value of WH production cross section and the branching ratio are shown in Table 8.1. $\epsilon_{WH\to\ell\nu b\bar{b}}$ is estimated using the Monte Carlo simulation. The detection efficiency (acceptance) for signal events is defined as:

$$\epsilon_{WH\to\ell\nu b\bar{b}} = \epsilon_{Z0} \cdot \epsilon_{trig} \cdot \epsilon_{leptonid} \cdot \epsilon_{btag} \cdot \epsilon^{MC}_{WH\to\ell\nu b\bar{b}} \cdot \left(\sum_{l'=e,\mu,\tau} BR(W \to \ell'\nu) \right), \qquad (8.1)$$

where $\epsilon^{MC}_{WH\to\ell\nu b\bar{b}}$ is the fraction of signal events (with $|z_0| < 60$ cm) corresponding to the data selection) which pass the kinematic and b-tagging requirements. $\epsilon^{MC}_{WH\to\ell\nu b\bar{b}}$ does not include experimental effect and the detector response completely. Therefore a scale factor is required to take into account the difference between the observed data and the MC simulation. $\epsilon_{leptonid}$ and ϵ_{btag} are the scale factor.

	110 GeV	115 GeV	120 GeV	130 GeV	140 GeV	150 GeV
Cross section (pb)	0.21	0.18	0.15	0.12	0.09	0.07
Branching ratio (%)	0.77	0.73	0.68	0.52	0.34	0.17

Table 8.1: The production cross section ($p\bar{p} \to WH$) in Tevatron beam energy and branching ratio ($H \to b\bar{b}$) for several Higgs masses.

b-tagging category	110 GeV	115 GeV	120 GeV	130 GeV	140 GeV	150 GeV
Pretag	3.04±0.08	3.15±0.08	3.25±0.08	3.34±0.08	3.45±0.09	3.48±0.09
One tag w/ NN tag	0.91±0.05	0.93±0.05	0.93±0.05	0.97±0.05	1.01±0.06	1.01±0.06
ST + ST	0.42±0.04	0.44±0.05	0.48±0.05	0.51±0.05	0.51±0.05	0.51±0.05
ST + JP	0.36±0.04	0.38±0.04	0.38±0.04	0.42±0.04	0.43±0.05	0.43±0.05

Table 8.2: WH signal acceptance (%) in W+2jet events for each tag category and Higgs masses. Systematic error is included in uncertainties. One SECVTX tag w/ NN tag, double SECVTX tag (ST+ST) and SECVTX tag + jet probability (ST+JP) categories are exclusive to each other.

b-tagging category	110 GeV	115 GeV	120 GeV	130 GeV	140 GeV	150 GeV
Pretag	9.41±0.61	7.92±0.52	6.35±0.41	3.99±0.26	2.02±0.13	0.78±0.05
One tag w/ NN tag	2.81±0.23	2.35±0.19	1.82±0.15	1.15±0.09	0.59±0.05	0.23±0.02
ST + ST	1.31±0.16	1.11±0.14	0.94±0.11	0.61±0.07	0.30±0.04	0.11±0.01
ST + JP	1.11±0.13	0.94±0.11	0.74±0.09	0.50±0.06	0.25±0.03	0.10±0.01

Table 8.3: The number of expected WH signal events calculated for integrated luminosity 1.9 fb^{-1} in each tag category. Systematic error is included in uncertainties. One SECVTX tag w/ NN tag, double SECVTX tag (ST+ST) and SECVTX tag + jet probability (ST+JP) categories are exclusive to each other.

The quantity ϵ_{Z0} is the efficiency of the $|z_0| < 60$ cm cut, and is measured in observed data. The difference between data and MC is taken into account. The trigger efficiencies for high p_T leptons, ϵ_{trig}, are also measured in data using back-up triggers with relaxed requirements [67]. The lepton identification and reconstruction efficiencies measured in Monte Carlo are corrected by scale factors, $\epsilon_{leptonid}$ derived from the observed $Z \to \ell^+\ell^-$ data [68, 69]. The scale factor for b-tagging, ϵ_{btag}, was derived as described in chapter 4. Finally, $BR(W \to \ell\nu)$ is the branching ratio for leptonic (e, μ, τ) W decay, $W \to e\nu$, $W \to \mu\nu$ and $W \to \tau\nu$. This branching ratio is take from PDG [65].

Finally, we obtain the final acceptance. Figure 8.1 shows the overall acceptance for each b-tagging condition including all systematic effects as a function of Higgs mass. The acceptances for the SECVTX double-tag selection range from 0.42±0.04% to 0.51±0.05%. For the one SECVTX tag plus Jet probability tag category, the acceptance increases from 0.36±0.04% to 0.43±0.05%. For the one SECVTX with NN tag category, the acceptance increase from 0.91±0.05% to 1.01±0.06%. These three b-tagging categories are exclusive to each other. category. Table 8.2 shows the acceptances for various Higgs masses and the various tagging categories. Systematic uncertainties are discussed in detail in the following subsection.

The expected number of WH signal events is estimated from the calculated acceptance as shown in Table 8.3.

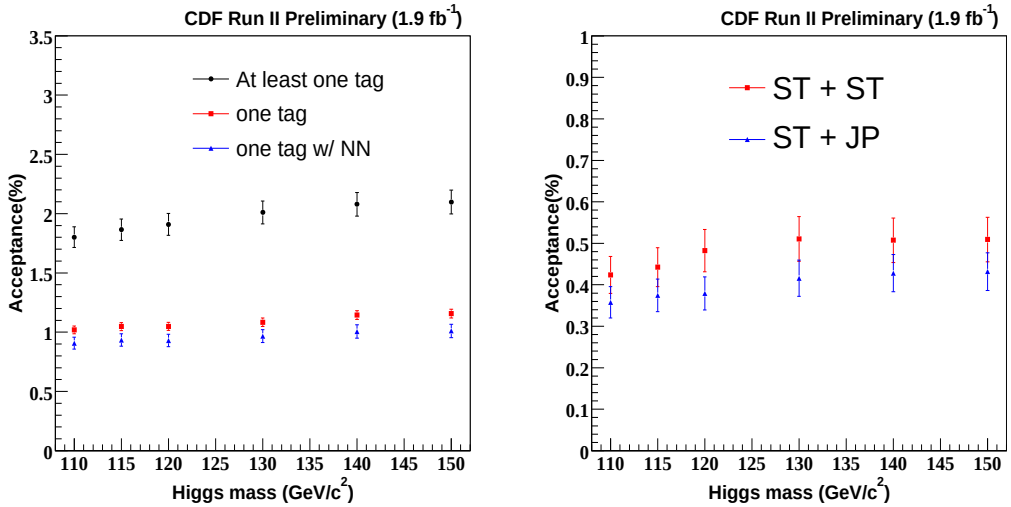

Figure 8.1: Signal acceptance as a function of Higgs mass in each tag category.

8.1.1 Systematic Uncertainties on Acceptance

The systematic uncertainties on the acceptance include uncertainties on the jet energy scale, the initial and final state radiation, the lepton identification and the trigger efficiencies and the b-tagging scale factors.

- Lepton identification:
  Systematic uncertainties are evaluated by comparing the CDF data sample of Z events with the PYHITA Z sample. These uncertainties are estimated for each lepton type (CEM, CMUP and CMX). The systematic uncertainty is at a $\sim$ 2% level depending on the lepton type.

- Trigger:
  This systematic uncertainty is measured from the backup trigger. This uncertainty depends on trigger type (CEM, CMUP and CMX). But it has only a small contribution ($< 1\%$ level).

- Initial and Final State Radiation (ISR/FSR)
  ISR and FSR systematic uncertainties are estimated by changing the parameters related to ISR and FSR from default values to half or double. Half of difference between the two samples is taken as the systematic uncertainty. The estimated ISR/FSR total systematic uncertainties in the ST+ST, the ST+JP and one SECVTX w/ NN tag categories are 5.2%, 4.0% and 2.3%, respectively.

- Parton Distribution Function (PDF):
  To estimate uncertainty in the incoming parton energy in proton and antiproton, CTEQ5L is used as the nominal PDF, which is a leading order (LO) calculation. CTEQ PDF is parametrized with 20 eigen vectors. An NLO version of PDF CTEQ6M provides a 90% confidence interval of each eigen vector. Setting the value of each eigen vector at 90% edge of the confidence interval, nominal PDF is reweighted and the corresponding acceptance is calculated. The differences between the nominal and reweighted acceptances are added in a quadrature, which is assigned as the systematic uncertainty.

b-tagging category	LeptonID	Trigger	ISR/FSR	JES	PDF	b-tagging	Total
One tag w/ NNtag	$\sim 2\%$	$< 1\%$	2.9%	2.3%	1.2%	3.5%	5.6%
ST + ST	$\sim 2\%$	$< 1\%$	5.2%	2.5%	2.1%	8.4%	10.6%
ST + JP	$\sim 2\%$	$< 1\%$	4.0%	2.8%	1.5%	9.1%	10.5%

Table 8.4: Systematic uncertainties for each tagging category.

- Jet Energy Scale (JES):
  To obtain the systematic uncertainty coming from the jet energy scale [66], we use the W+Higgs MC sample for a Higgs mass of 120 GeV/c^2, assuming that the Higgs mass dependence is negligibly small. Shifting the jet energies in the WH MC samples by $\pm 1\sigma$ we calculate the acceptance and take the deviation of this acceptance from the nominal acceptance as the systematic uncertainty. The estimated uncertainty in the ST+ST, the ST+JP and one SECVTX w/ NN tag categories is 2.5%, 2.8% and 1.2%, respectively.

- b-tagging
  The systematic coming from the b-tagging scale factor uncertainties was discussed in Chapter 4.

Total systematic uncertainties are listed in Table 8.4 for each b-tagging category. Luminosity uncertainties of 6% are also included in calculating the number of the expected Higgs signal events.

8.2 Kinematic Distributions

We check the kinematics for each b-tagging category to make sure that the background compositions are well understood. Especially the dijet mass distribution is characteristic and interesting variables for the Higgs search as it gives a resonance peak of the Higgs signal. If Higgs signal exists, the excess in dijet mass distribution would be expected. In this section, some kinematic distributions in addition to the dijet mass distribution are shown to validate whether the expected standard background shape is well modeled for each tagging category by comparing the observed data shapes. The concerned physics objects are lepton, neutrino and two jets. Checking these kinematic variables are important to verify including E_T , η and ϕ distributions for lepton and both jets. It is also important to check the E_T and the direction of jet. For missing transverse energy, the scale of $\not\!\!E_T$ and ϕ distributions are shown because z-component is unknown. In addition, it is important to check the following correlations among objects; (1) Ht is defined as a scalar sum of E_T of jet, lepton and $\not\!\!E_T$. (2) The transverse mass of W boson defined as

$$M_T = \sqrt{(E_T^l + \not\!\!E_T)^2 - (\boldsymbol{p}_T^l + \not\!\!\boldsymbol{E}_T)^2}$$

. (3) The angles between objects. (4) Six neural network input variables defined by in chapter 6. Finally the NN output distribution is shown for each selection category.

In this section, the above kinematic distributions are shown for pretag events as control sample and for ST+ST, ST+JP and one SECVTX w/ NN tag events as signal samples. The kinematic distributions for control sample has small discrepancy between observed data and expected background. This discrepancy results from the incomplete modeling of non-W shape. Alternative modeling of non-W shape is check and the effect for final results is discussed in appendix.

8.2.1 Kinematic Distributions of Pretag Events

Figures 8.2-8.10 show the observed and expected shapes of the above variables in the pretag W+2jets sample. In the pretag samples, the background shape is shown by normalizing to the number of W+jet background events observed in the data to visualize contribution. All of these plots show good agreement between the data and the background prediction. We also show the signal shape which is multiplied by 100.

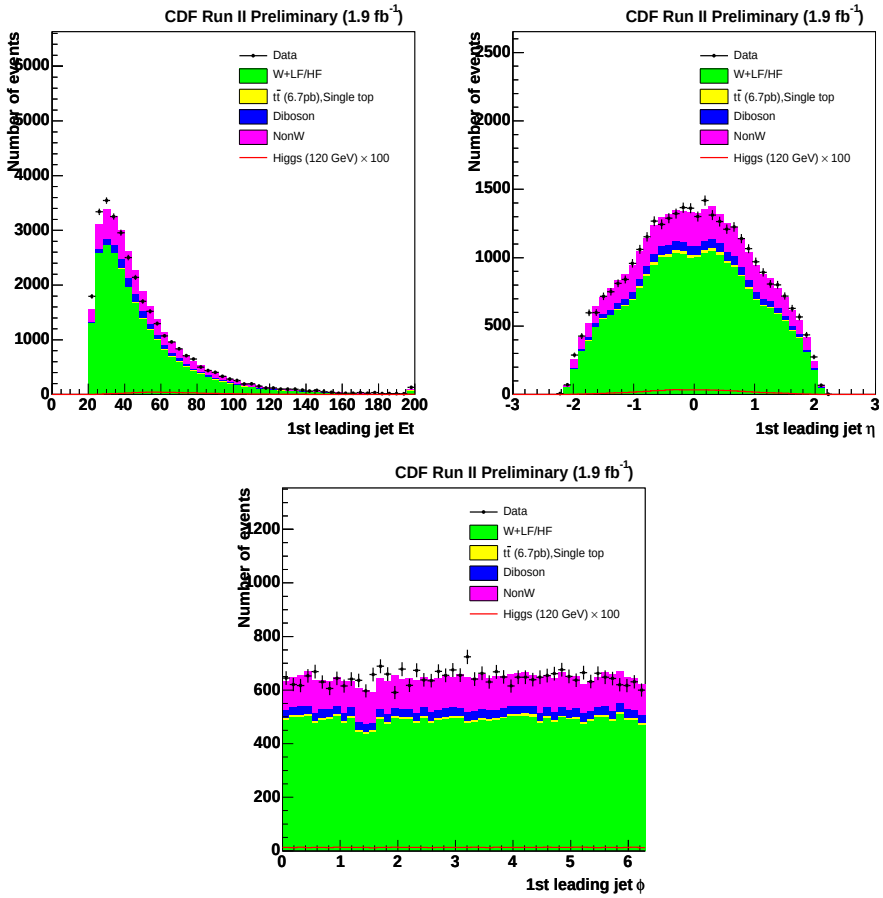

Figure 8.2: The first leading jet E_T, η and ϕ kinematic distributions in the pretag sample. The total background is normalized to data using W+jets background. Other background components are fixed.

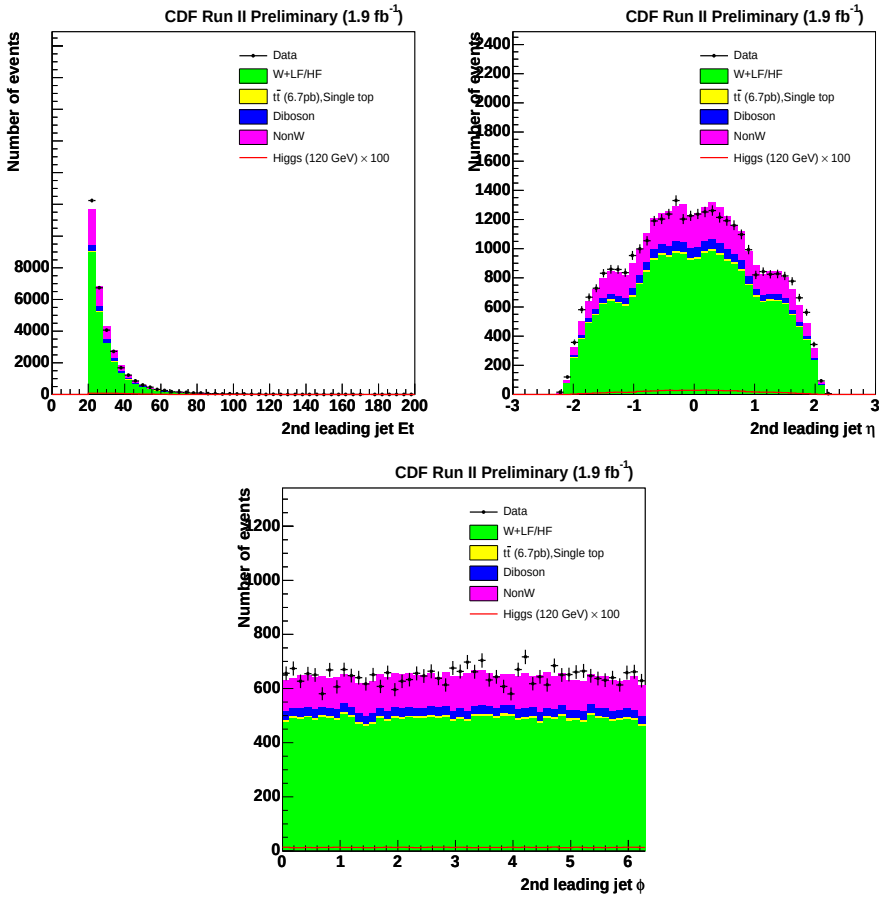

Figure 8.3: The second leading jet E_T, η and ϕ kinematic distributions in the pretag sample. The total background is normalized to data using W+jets background. Other background components are fixed.

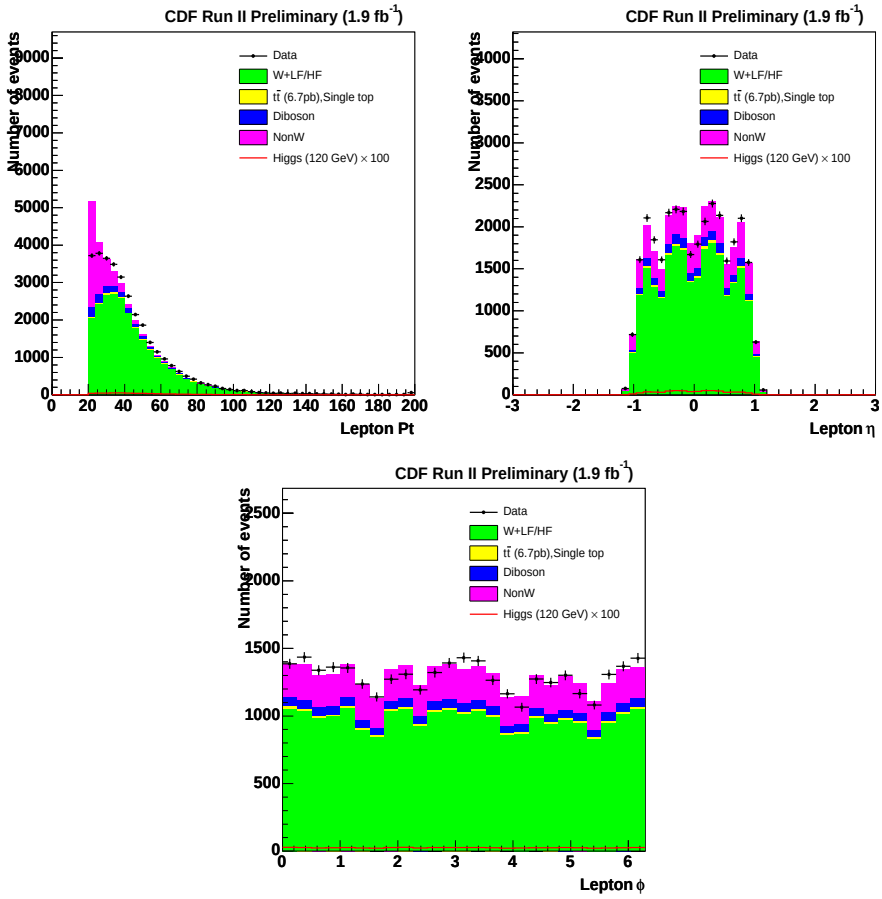

Figure 8.4: The lepton p_T, η and ϕ kinematic distributions in the pretag sample. The total background is normalized to data using W+jets background. Other background components are fixed.

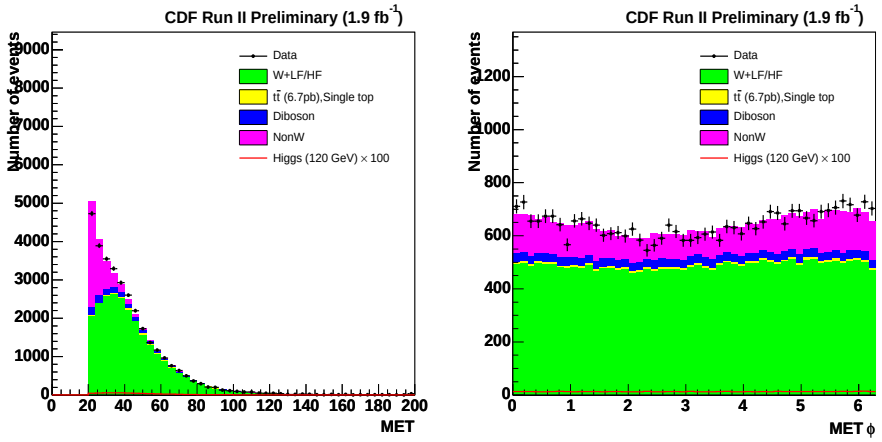

Figure 8.5: The $\not\!\!E_T$ and its ϕ kinematic distributions in the pretag sample. The total background is normalized to data using W+jets background. Other background components are fixed.

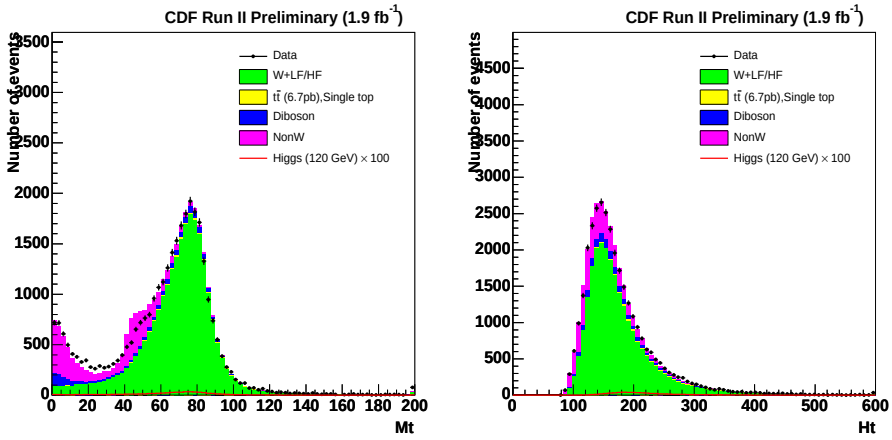

Figure 8.6: The reconstructed W transverse mass and Ht distributions in the pretag sample. The total background is normalized to data using W+jets background. Other background components are fixed.

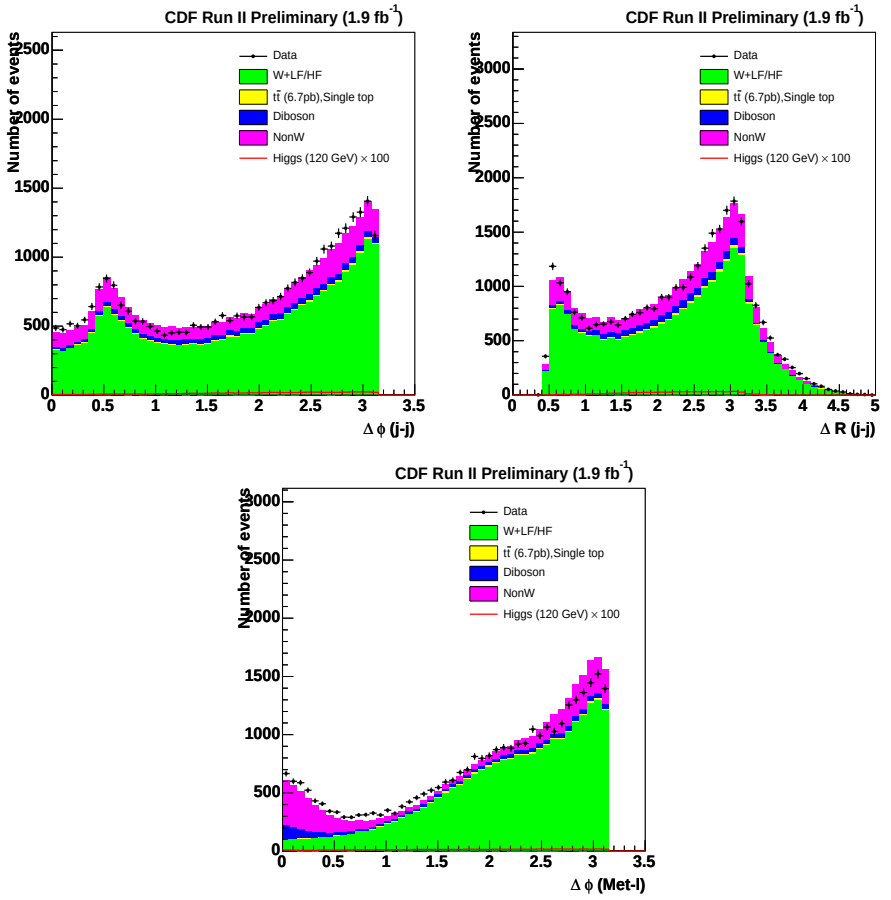

Figure 8.7: The observed and expected $\Delta\phi$ and ΔR between dijet and $\Delta\phi$ between $\not\!\!E_T$ and lepton in the pretag sample. The total background is normalized to data using W+jets background. Other background components are fixed.

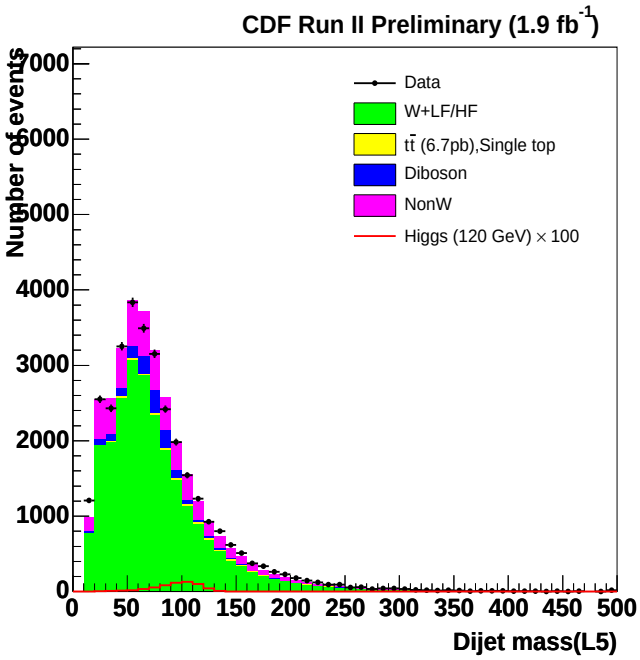

Figure 8.8: The reconstructed invariant mass of 2 jets system in the pretag sample. The total background is normalized to data using W+jets background. Other background components are fixed.

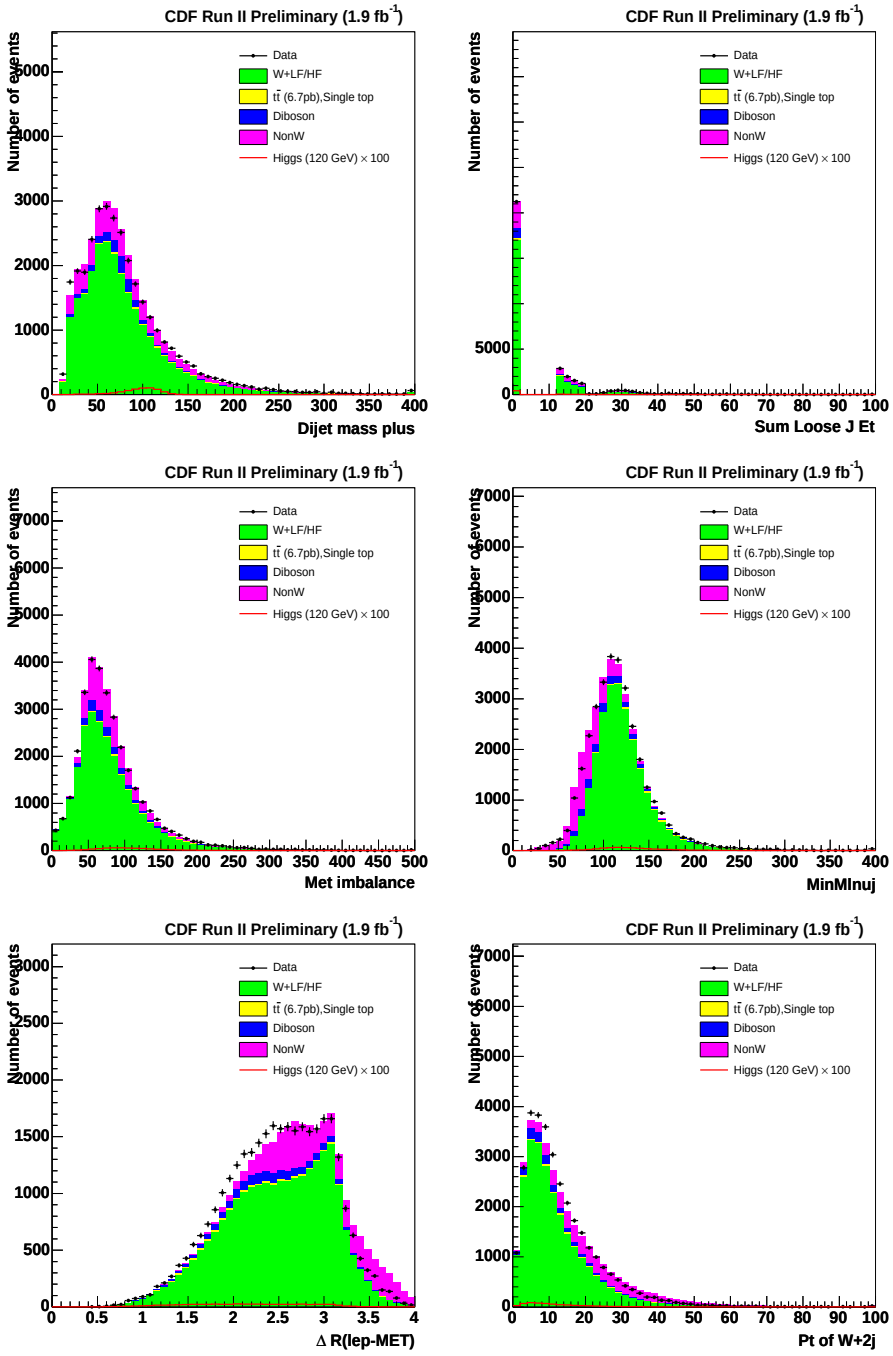

Figure 8.9: The observed and expected six NN input variables, Dijet mass+, scalar sum of the loose jet transverse energy, p_T imbalance, the invariant mass of lepton, $\not\!\!E_T$ and one of two jets, Δ R(lepton-ν) and p_T of W+2jet system in the pretag sample. The total background is normalized to data using W+jets background. Other background components are fixed.

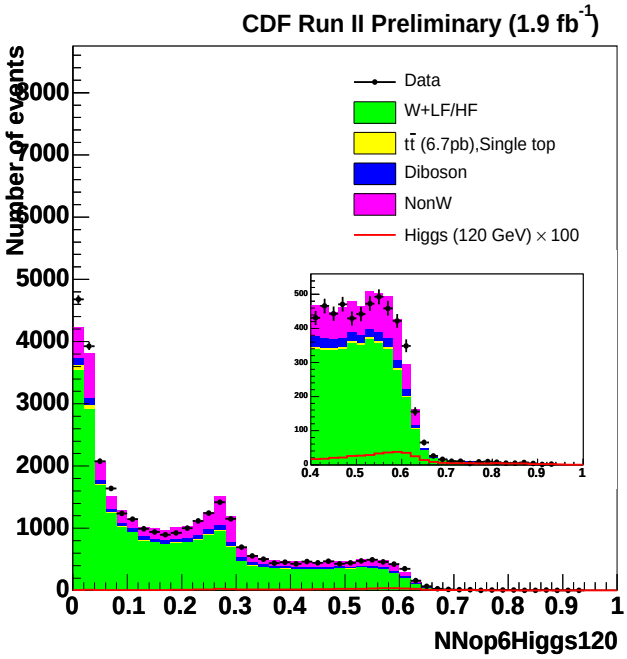

Figure 8.10: NN output shape calculated from six input variables for pretag sample. The Higgs signal should result large NN output values. The output shown here is NN trained a Higgs mass of 120 GeV/c^2. The total background is normalized to data using W+jets background. Other background components are fixed.

8.2.2 Kinematic Distributions in Double SECVTX Events

Figures 8.11-8.19 show the observed and expected kinematic distributions in the double SECVTX tagged W+2jets events. Again, our data and the background model agree within the statistical uncertainty. We also show the signal shape multiplied by 10 to visualize the signal shape.

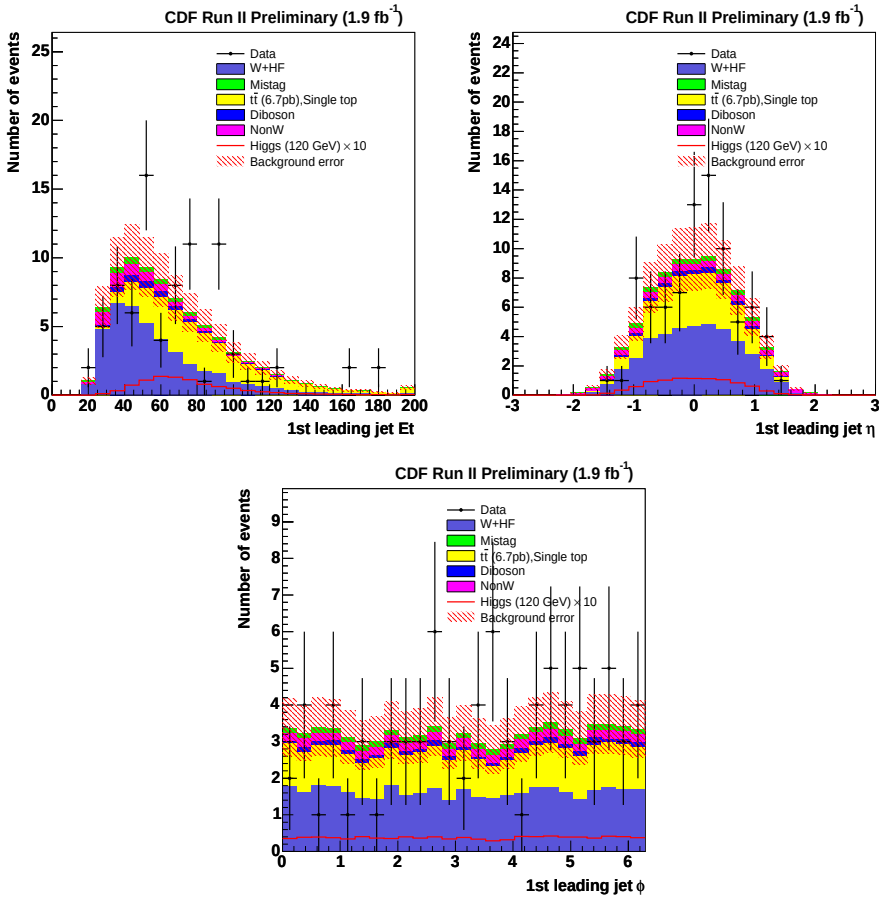

Figure 8.11: First leading jet E_T, η and ϕ kinematic distributions in double SECVTX tagged events. Background uncertainty is shown in red hash.

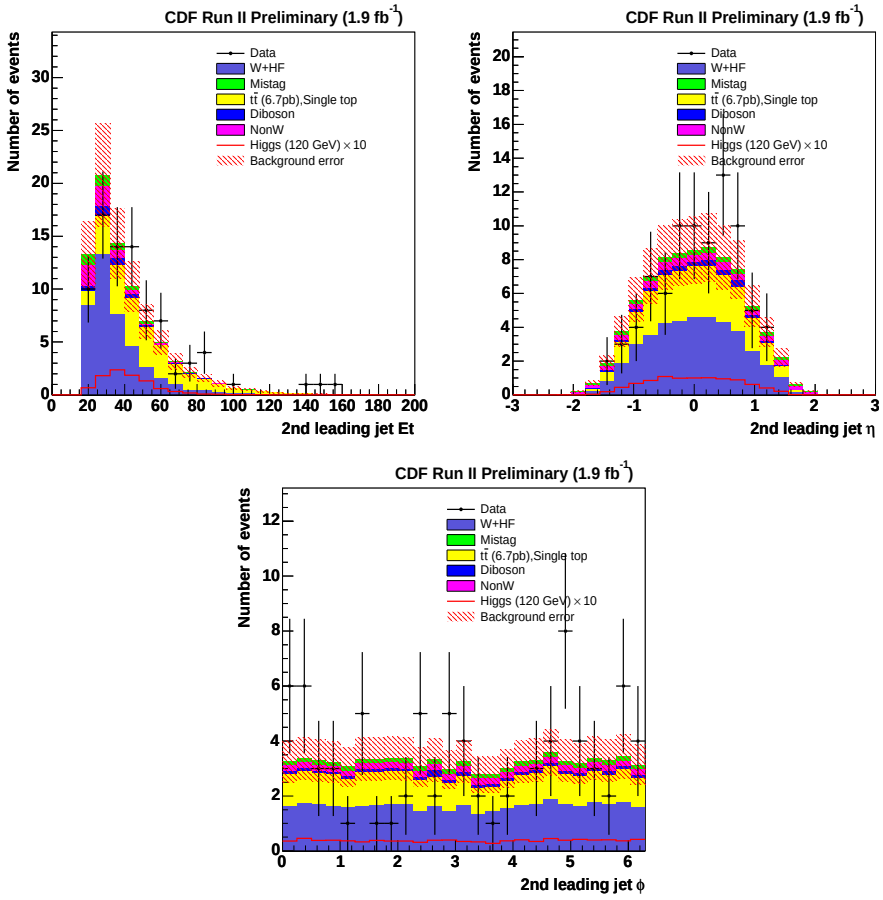

Figure 8.12: Second leading jet E_T, η and ϕ kinematic distributions in double SECVTX tagged events. Background uncertainty is shown in red hash.

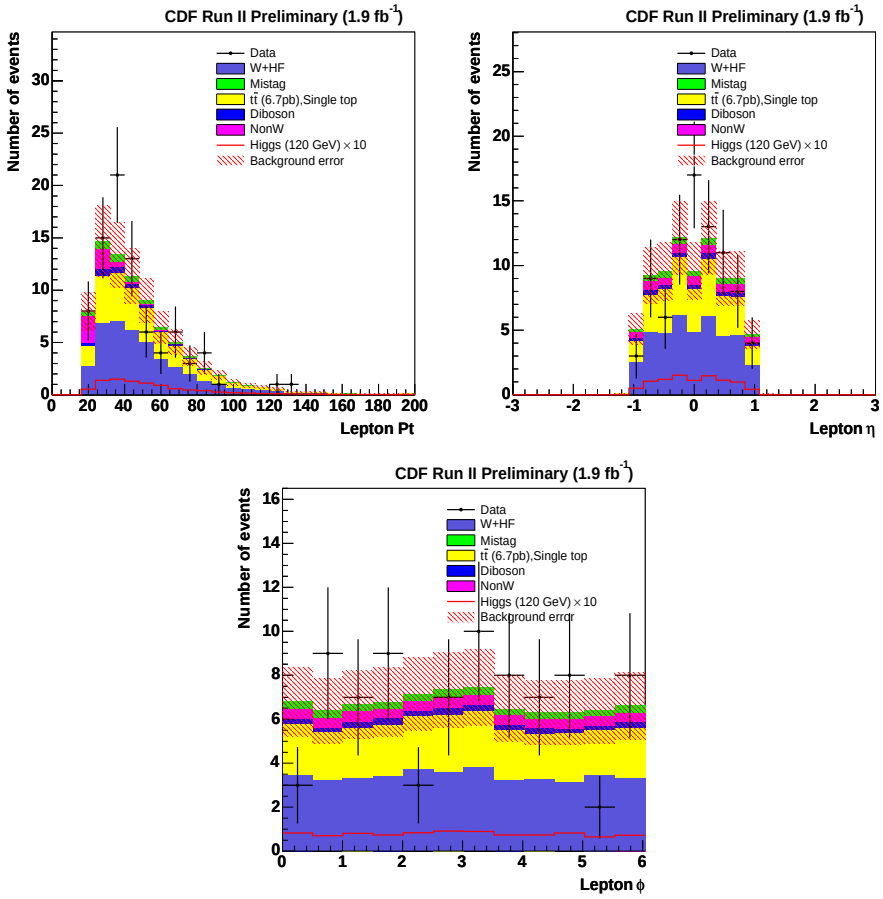

Figure 8.13: Lepton p_T, η and ϕ kinematic distributions in double SECVTX tagged events. Background uncertainty is shown in red hash.

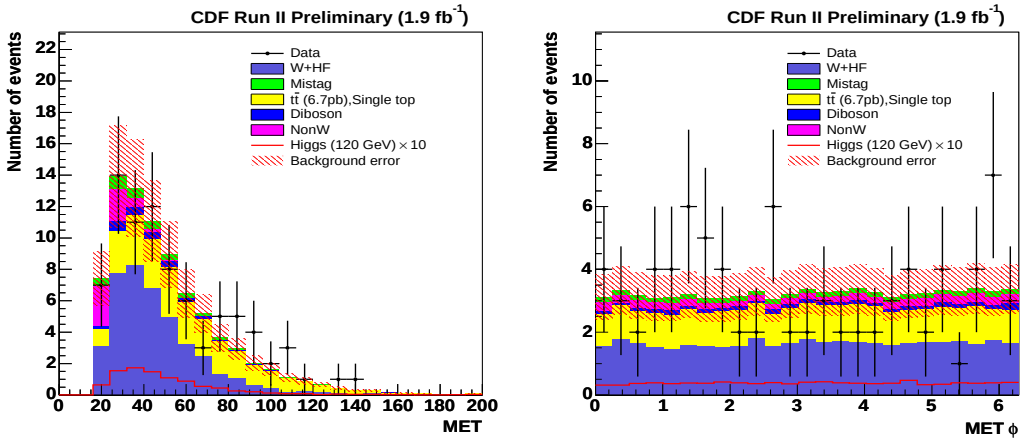

Figure 8.14: $\not\!\!E_T$ and ϕ kinematic distributions in double SECVTX tagged events. Background uncertainty is shown in red hash.

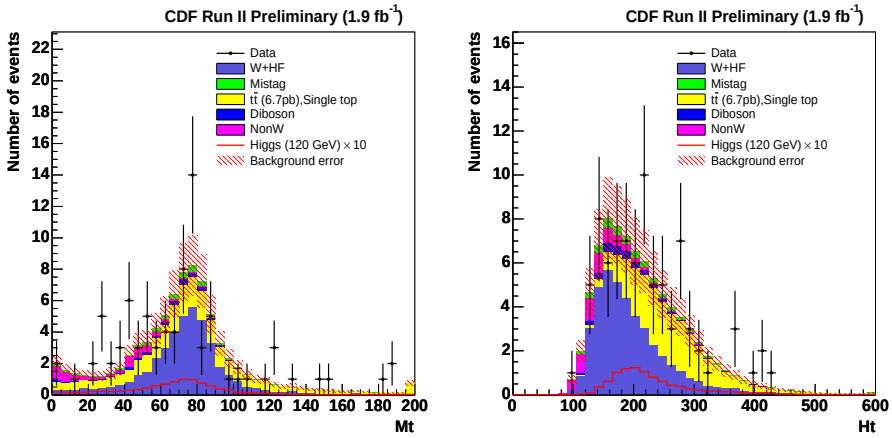

Figure 8.15: W transverse mass and Ht distributions in double SECVTX tagged events. Background uncertainty is shown in red hash.

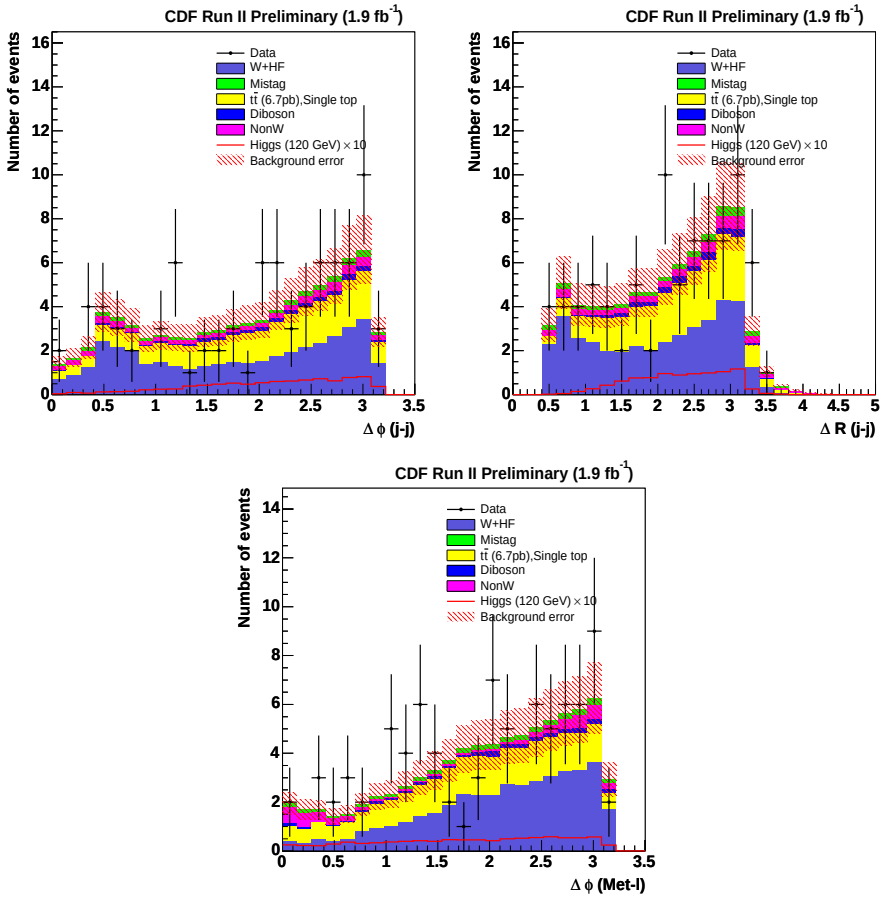

Figure 8.16: Distribution of $\Delta\phi$ between dijet, ΔR between dijet and $\Delta\phi$ between $\not\!\!E_T$ and lepton in double SECVTX tagged events. Background uncertainty is shown in red hash.

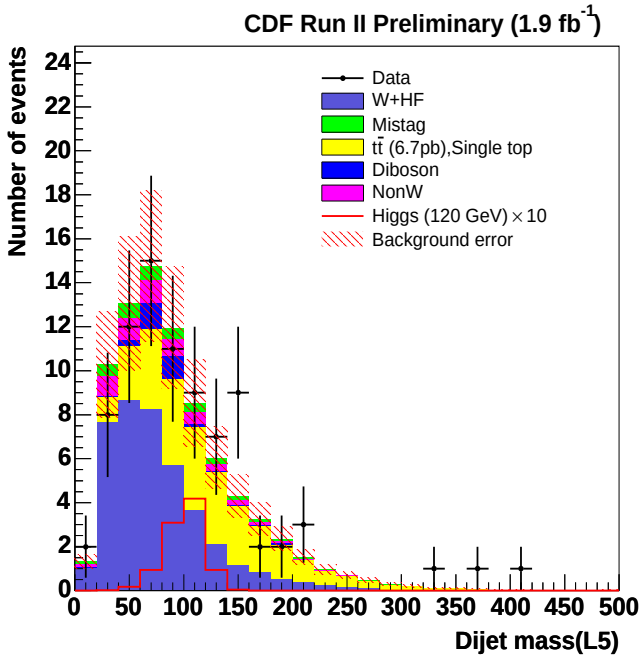

Figure 8.17: Reconstructed invariant mass of 2 jets system in double SECVTX tagged events. Background uncertainty is shown in red hash.

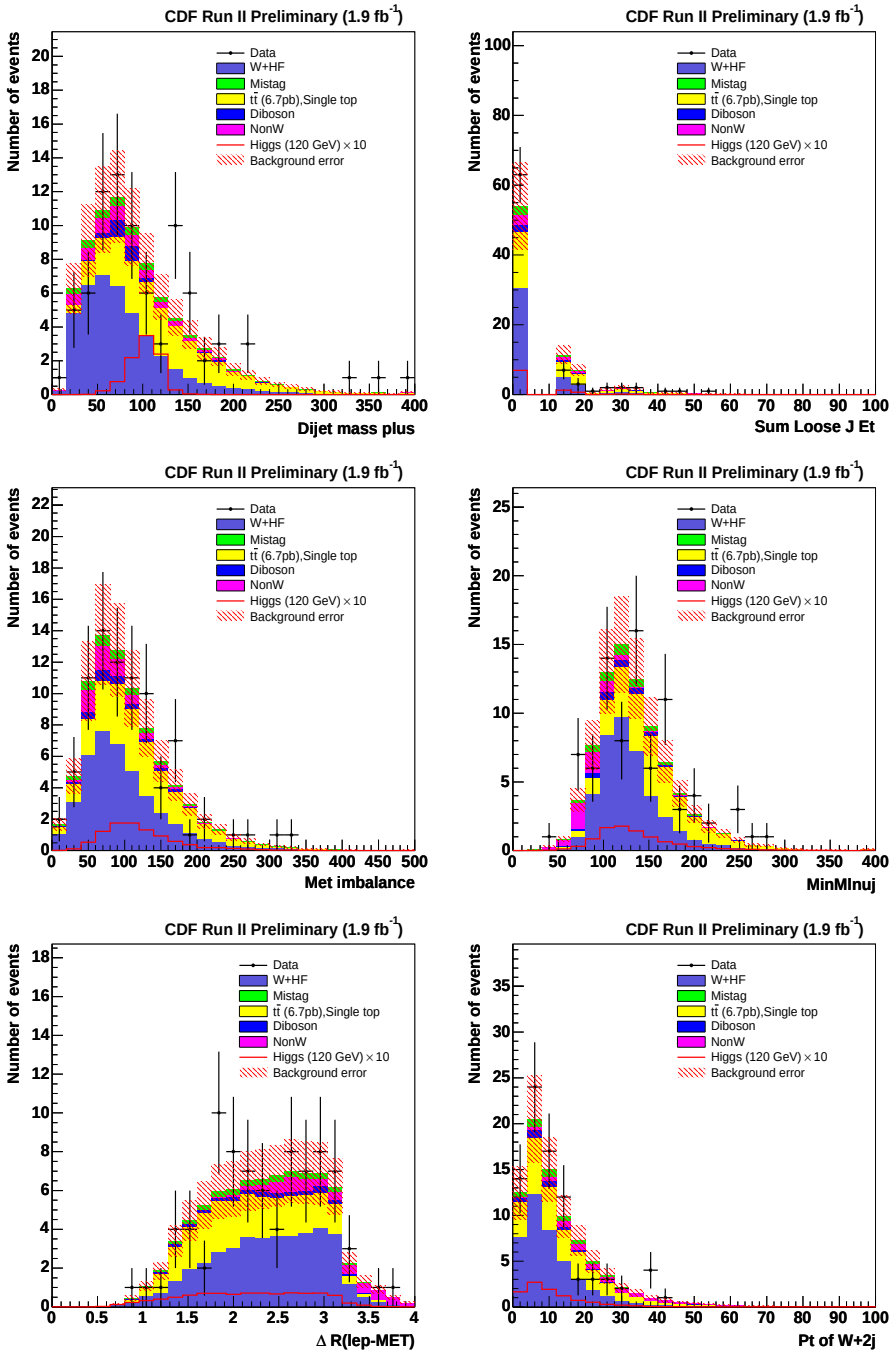

Figure 8.18: The observed and expected six NN input variables, Dijet mass+, scalar sum of the loose jet transverse energy, p_T imbalance, the invariant mass of lepton, $\not\!\!E_T$ and one of two jets, Δ R(lepton-ν) and p_T of W+2jet system in the double SECVTX tagged events. Background uncertainty is shown in red hash.

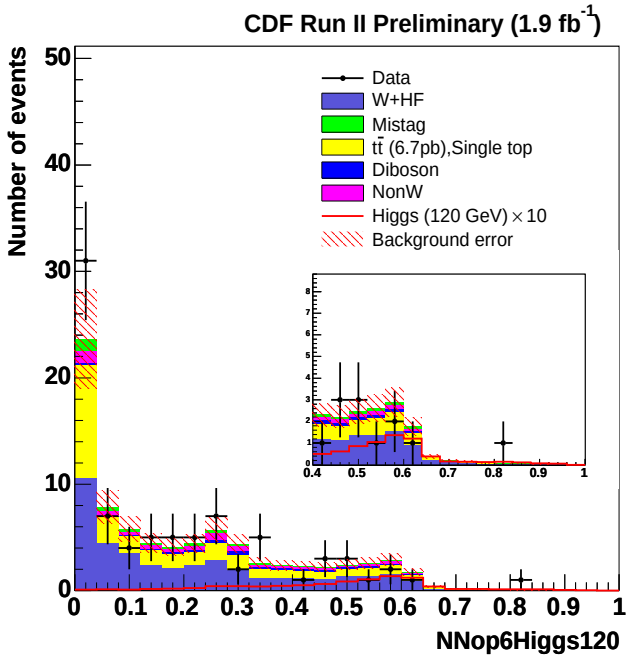

Figure 8.19: NN output shape calculated from the six input variables for ST+ST. The Higgs signal should result large NN output values. Background uncertainty is shown in red hash.

8.2.3 Kinematic Distributions in One SECVTX Tag plus One Jet Probability Tag Events

Figures 8.20-8.28 show the observed and expected kinematic shapes in the double tagged W+2jet events with one SECVTX tag plus one Jet probability tag. Again, agreements between observed and expected kinematic shapes are excellent although the statistics is not large. We also show the signal shape multiplied by 10 to visualize the signal shape.

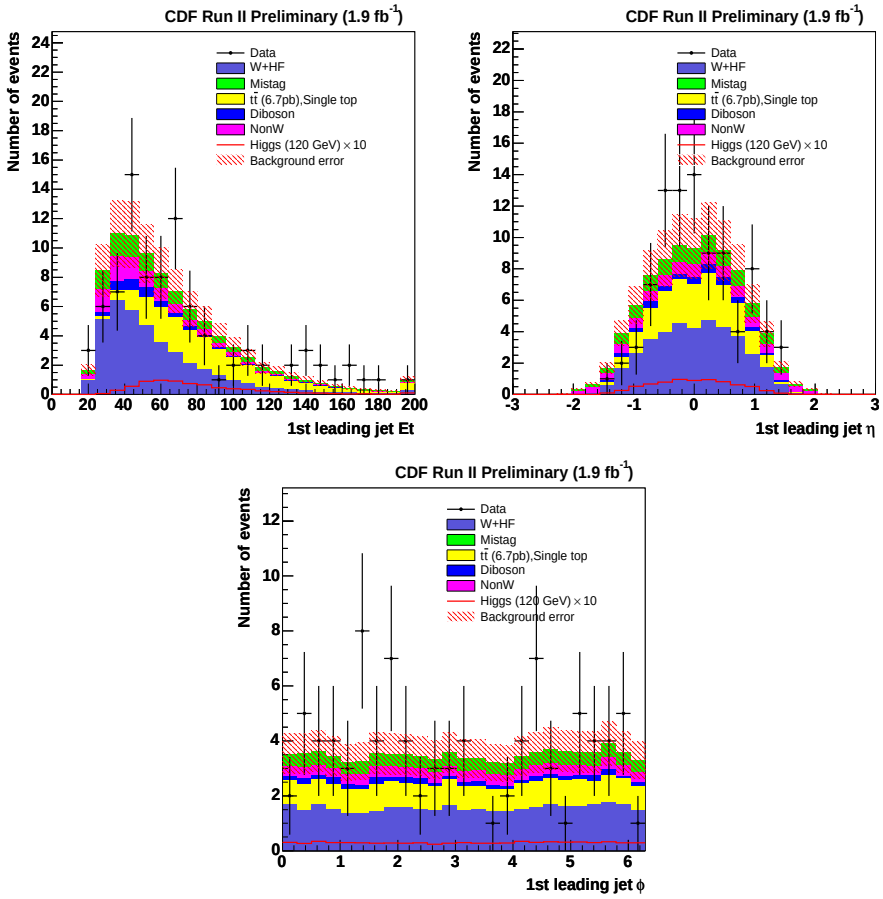

Figure 8.20: First leading jet E_T, η and ϕ kinematic distributions in one SECVTX tag plus one Jet probability tag events. Background uncertainty is shown in red hash.

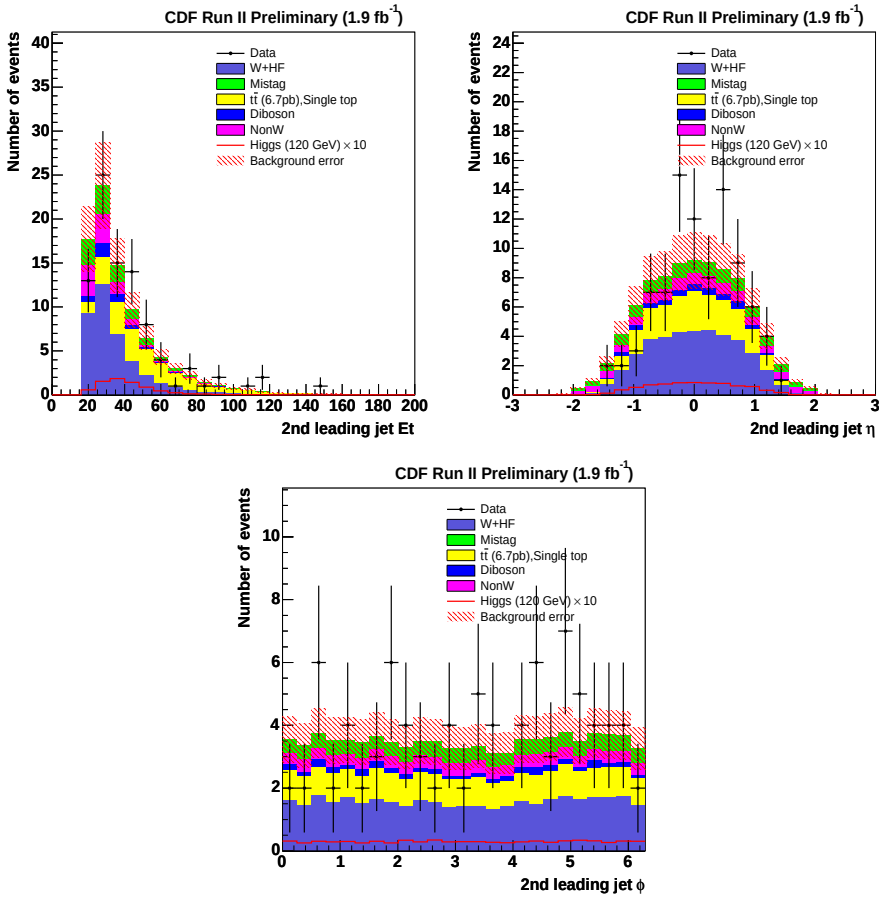

Figure 8.21: Second leading jet E_T, η and ϕ kinematic distributions in one SECVTX tag plus one Jet probability tag events. Background uncertainty is shown in red hash.

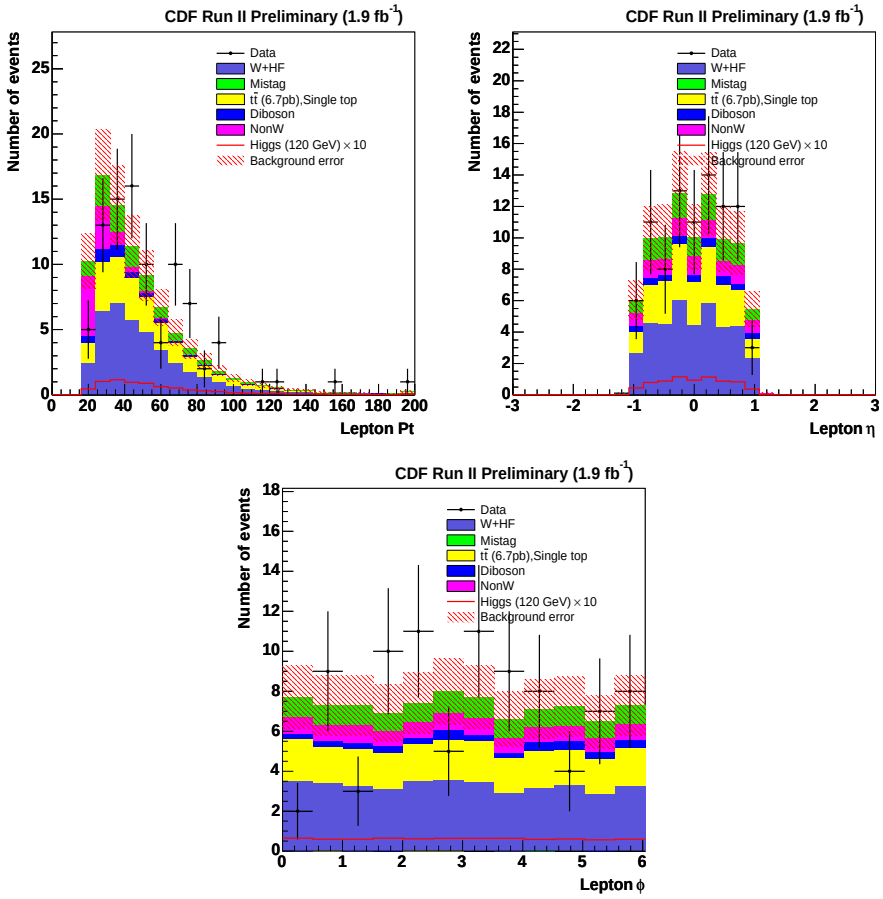

Figure 8.22: Lepton p_T, η and ϕ kinematic distributions in one SECVTX tag plus one Jet probability tag events. Background uncertainty is shown in red hash.

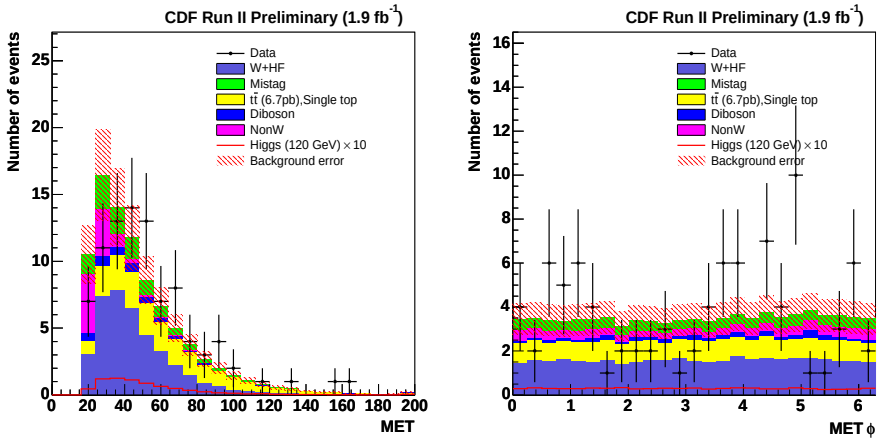

Figure 8.23: $\not\!\!E_T$ and its ϕ kinematic distributions in one SECVTX tag plus one Jet probability tag events. Background uncertainty is shown in red hash.

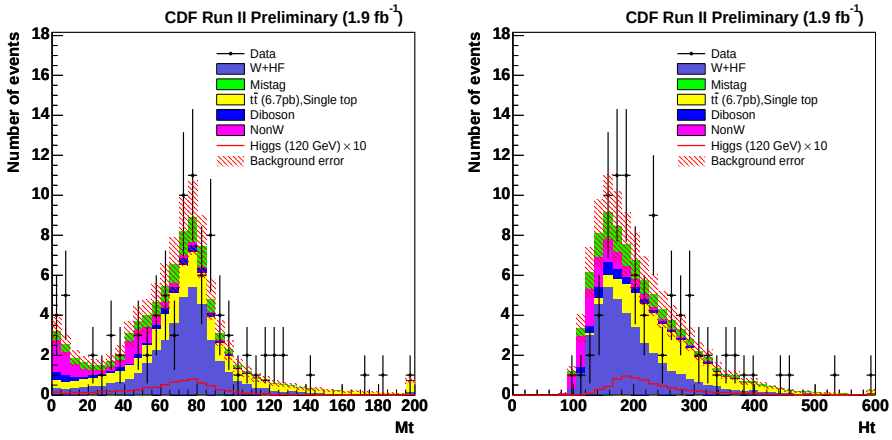

Figure 8.24: W transverse mass and Ht distributions in one SECVTX tag plus one Jet probability tag events. Background uncertainty is shown in red hash.

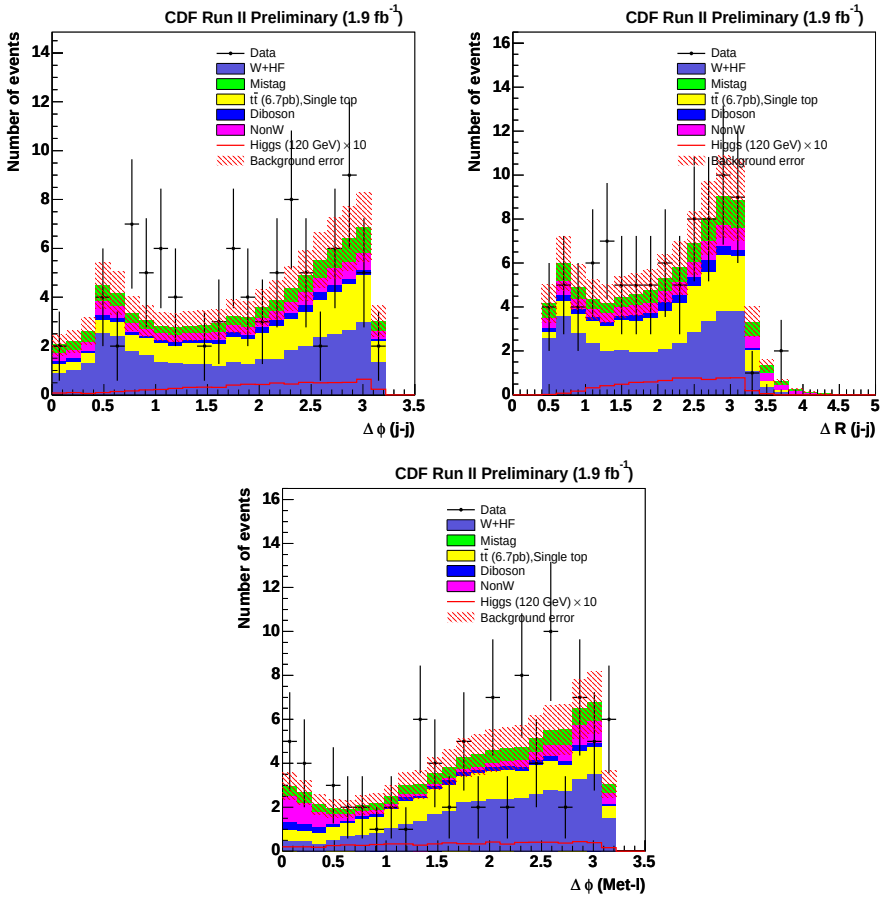

Figure 8.25: Distributions of $\Delta\phi$ between dijet, ΔR between dijet and $\Delta\phi$ between $\not\!\!E_T$ and lepton in one SECVTX tag plus one Jet probability tag events. Background uncertainty is shown in red hash.

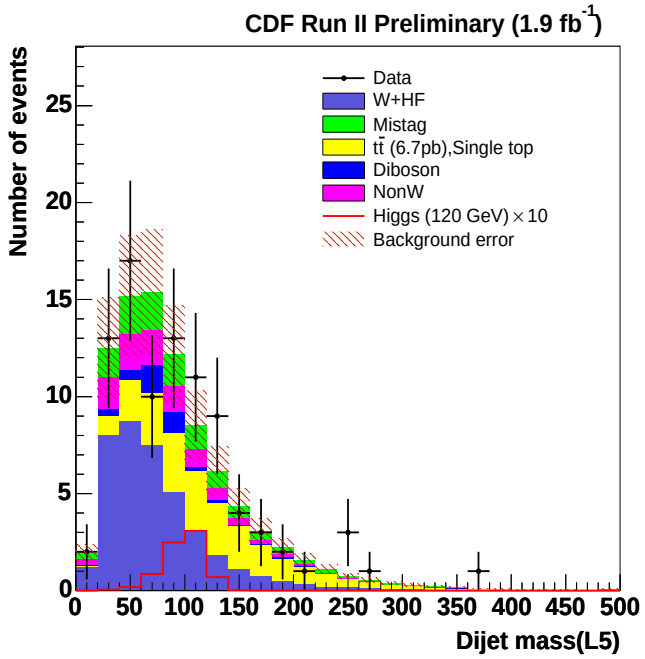

Figure 8.26: Reconstructed invariant mass of 2 jets system in one SECVTX tag plus one Jet probability tag events. Background uncertainty is shown in red hash.

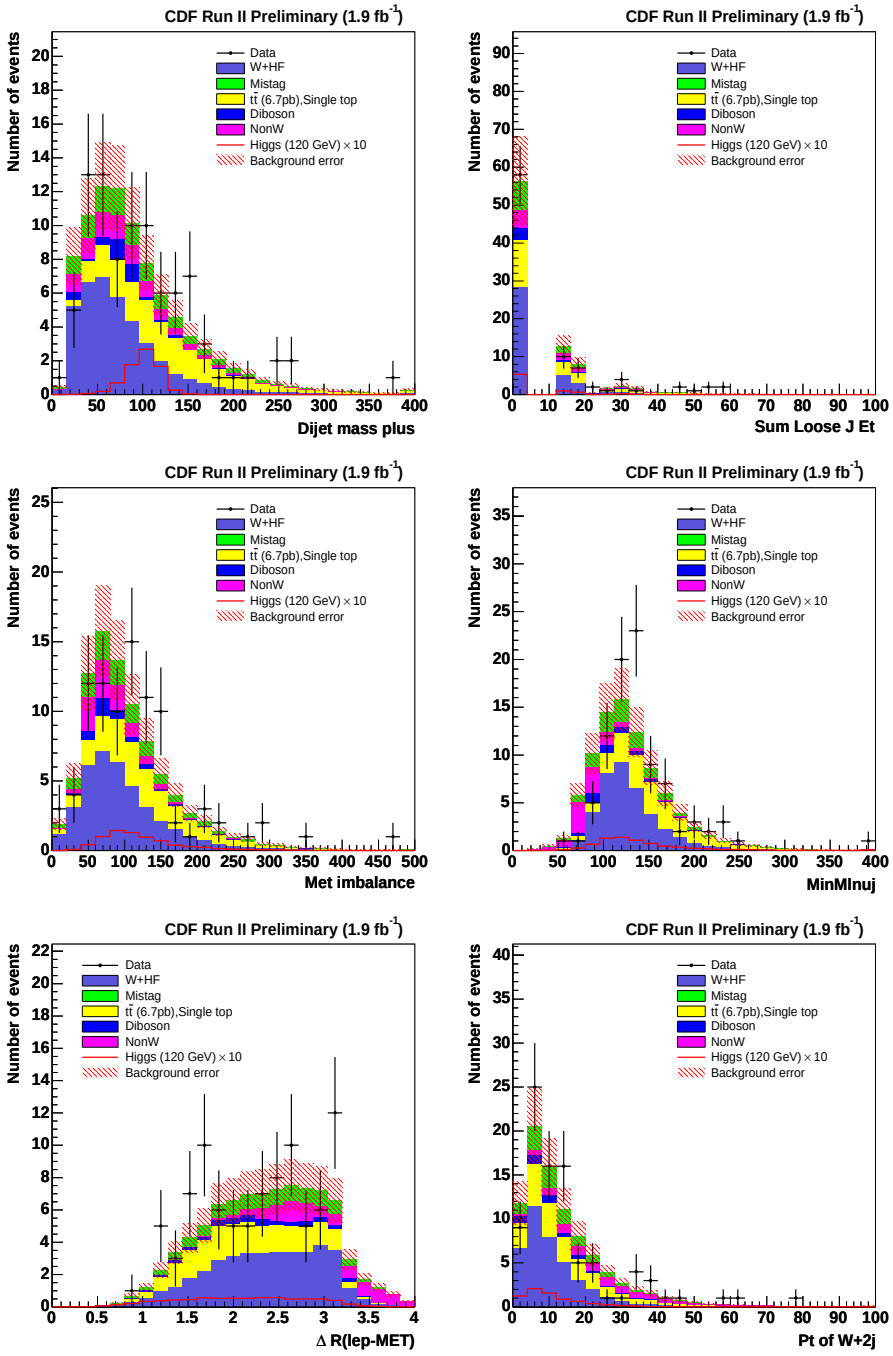

Figure 8.27: The observed and expected six NN input variables, Dijet mass+, scalar sum of the loose jet transverse energy, p_T imbalance, the invariant mass of lepton, $\not\!\!E_T$ and one of two jets, Δ R(lepton-ν) and p_T of W+2jet system in the one SECVTX tag plus one Jet probability tag events. Background uncertainty is shown in red hash.

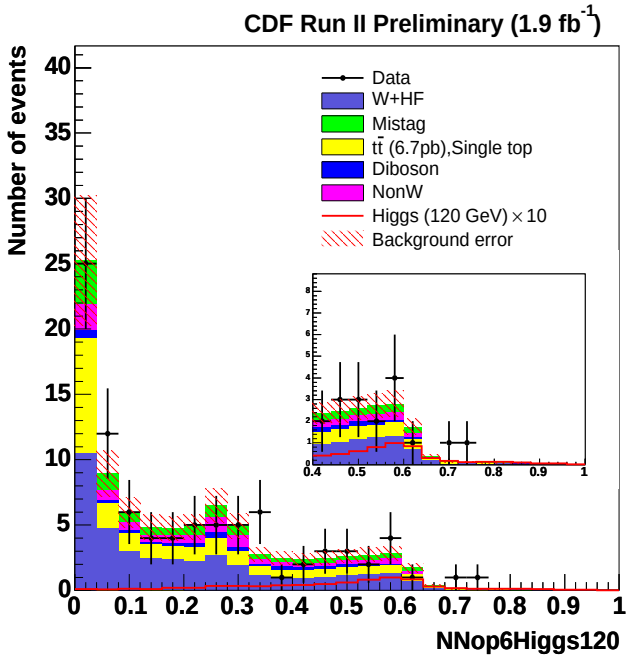

Figure 8.28: NN output shape calculated from the six input variables for one SECVTX tag plus one Jet probability tag. The Higgs signal should result large NN output values. Background uncertainty is shown in red hash.

8.2.4 Kinematic Shape in One SECVTX Tag with NN Tag Events

Figures 8.29-8.37 show the observed and expected kinematic shapes in one SECVTX tag with NN tag events. Again, agreements between observed and expected kinematic shapes are excellent although the statistics is not large. We also show the signal shape multiplied by 10 to visualize the signal shape.

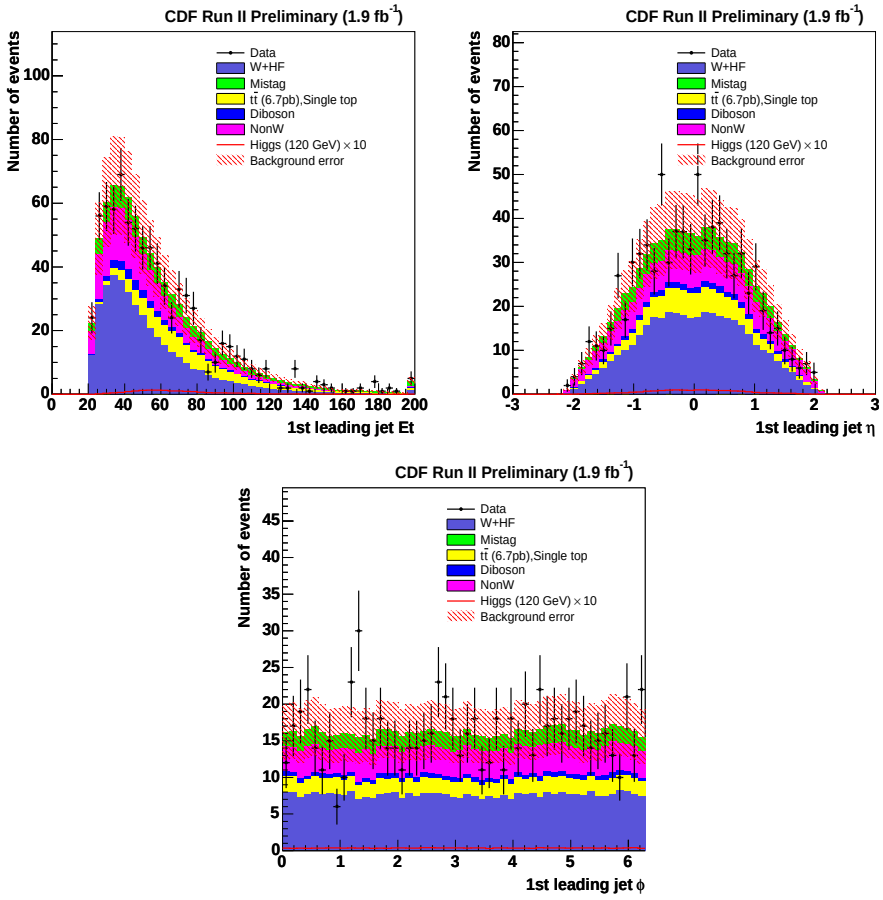

Figure 8.29: First leading jet E_T, η and ϕ kinematic distributions in one SECVTX tag with NN tag events. Background uncertainty is shown in red hash.

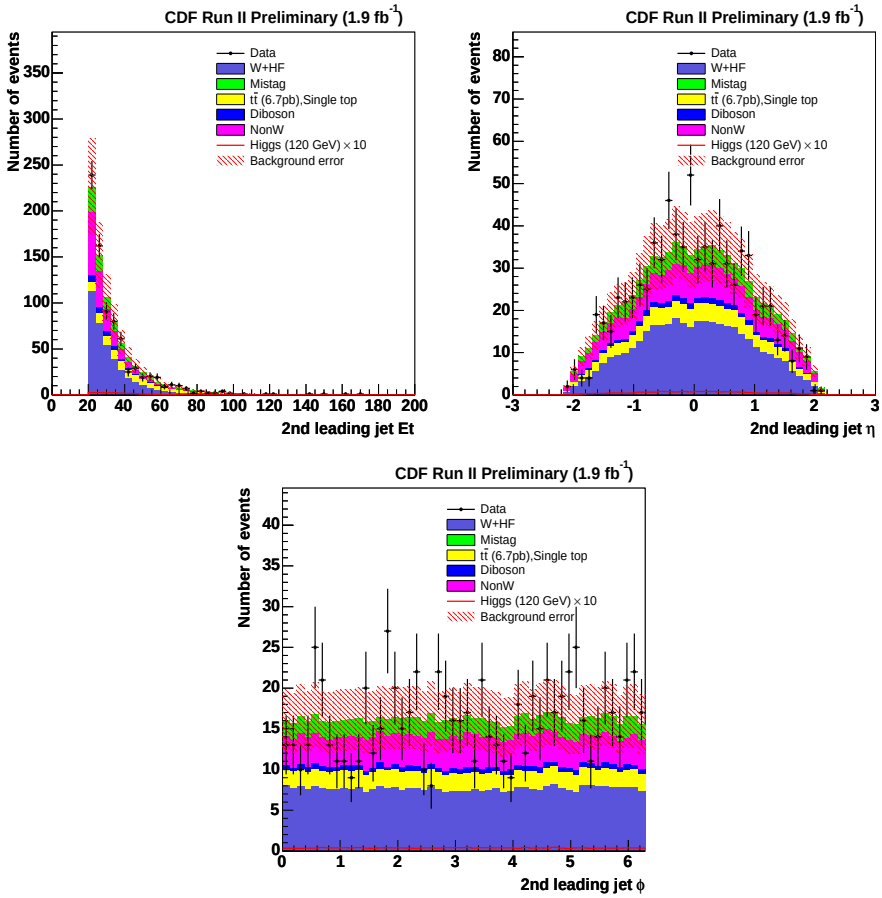

Figure 8.30: Second leading jet E_T, η and ϕ kinematic distributions in one SECVTX tag with NN tag events. Background uncertainty is shown in red hash.

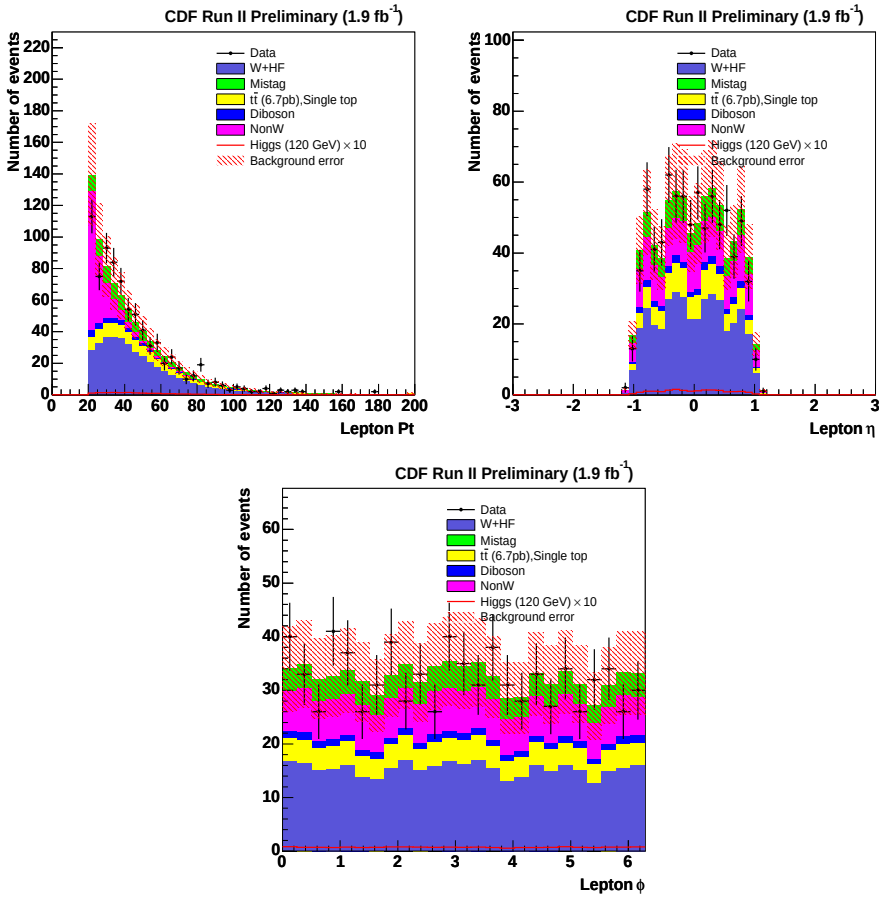

Figure 8.31: Lepton p_T, η and ϕ kinematic distributions in one SECVTX tag with NN tag events. Background uncertainty is shown in red hash.

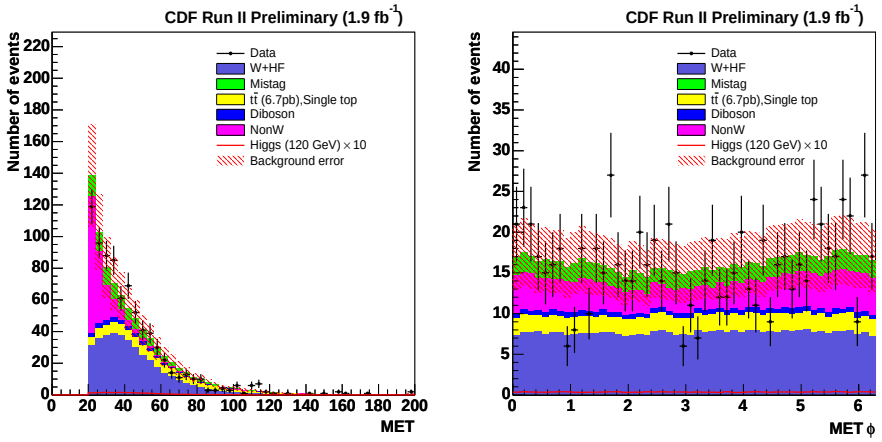

Figure 8.32: $\not\!\!E_T$ and its ϕ kinematic distributions in one SECVTX tag with NN tag events. Background uncertainty is shown in red hash.

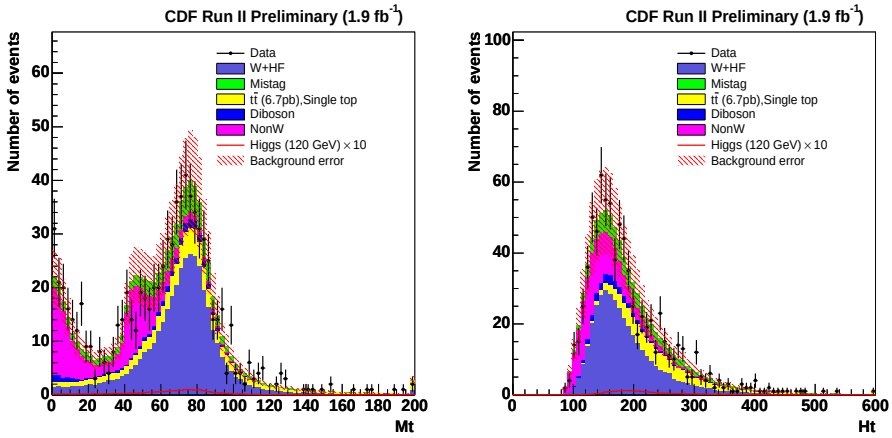

Figure 8.33: W transverse mass and Ht distributions in one SECVTX tag with NN tag events. Background uncertainty is shown in red hash.

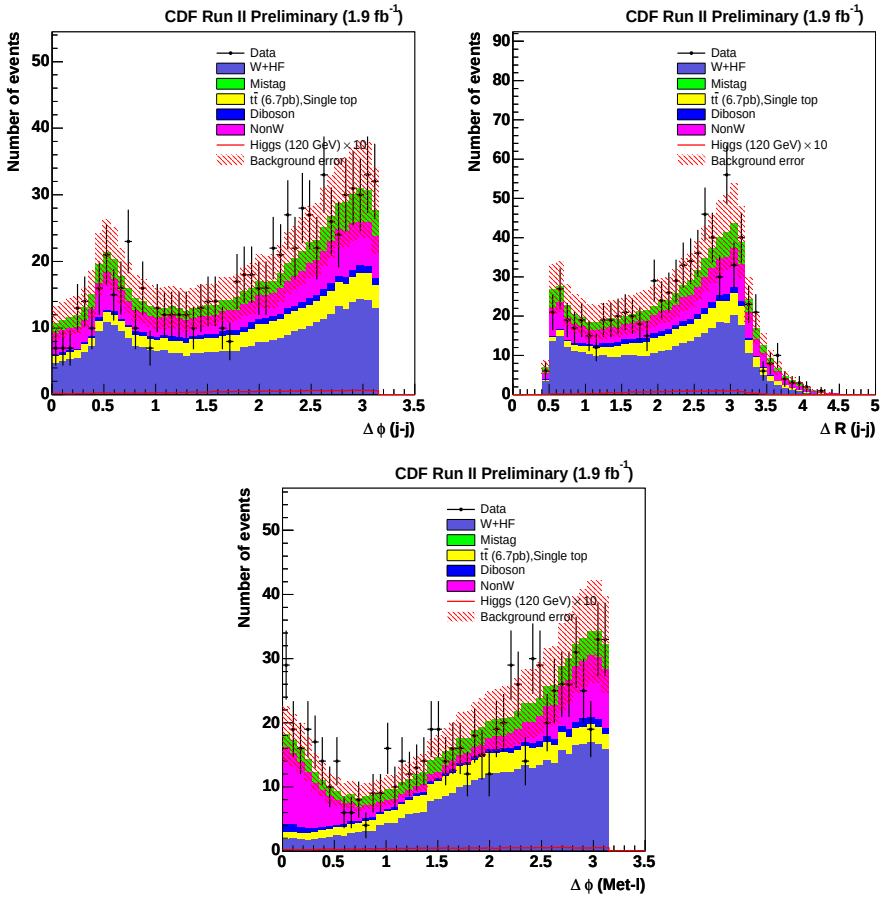

Figure 8.34: Distributions of $\Delta\phi$ between dijet, ΔR between dijet and $\Delta\phi$ between $\not\!\!E_T$ and lepton in one SECVTX tag with NN tag events. Background uncertainty is shown in red hash.

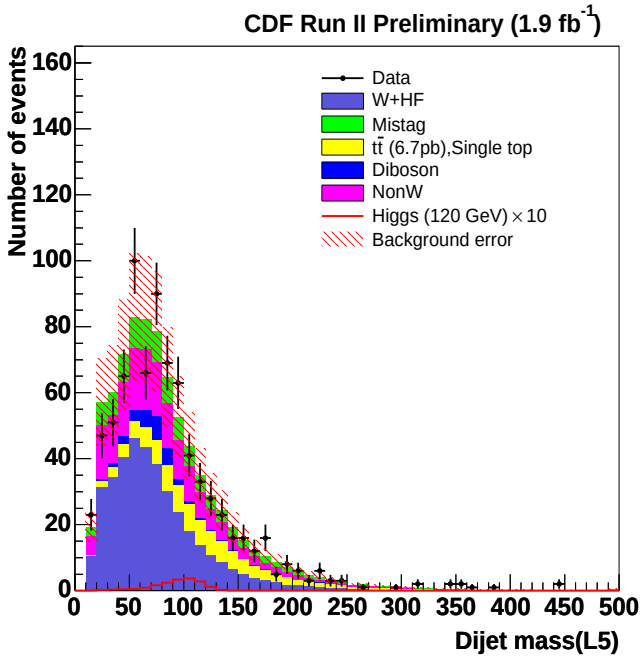

Figure 8.35: Reconstructed invariant mass of 2 jets system in one SECVTX tag with NN tag events. Background uncertainty is shown in red hash.

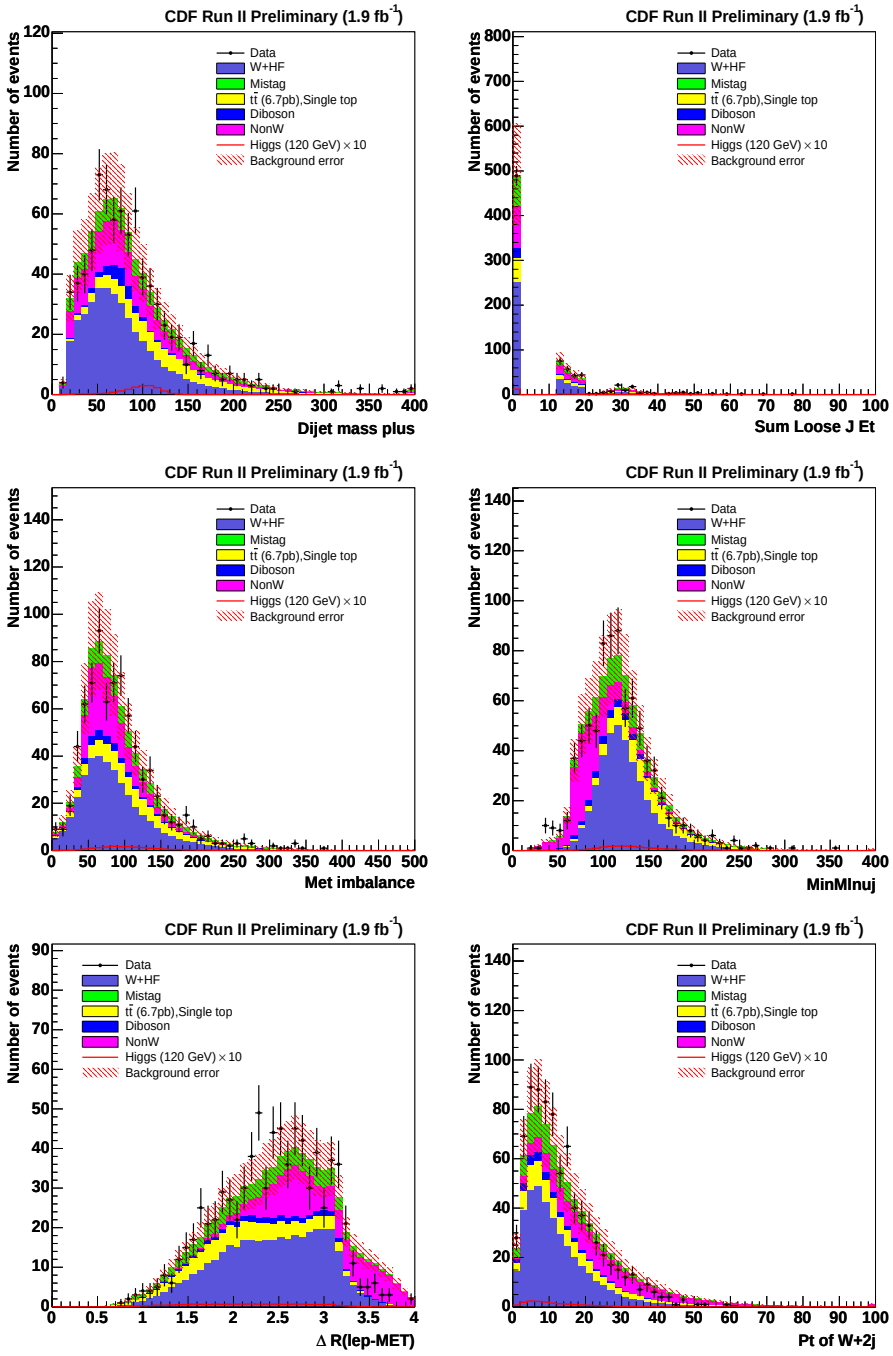

Figure 8.36: The observed and expected six NN input variables, Dijet mass+, scalar sum of the loose jet transverse energy, p_T imbalance, the invariant mass of lepton, $\not\!\!E_T$ and one of two jets, Δ R(lepton-ν) and p_T of W+2jet system in the one SECVTX tag with NN tag events. Background uncertainty is shown in red hash.

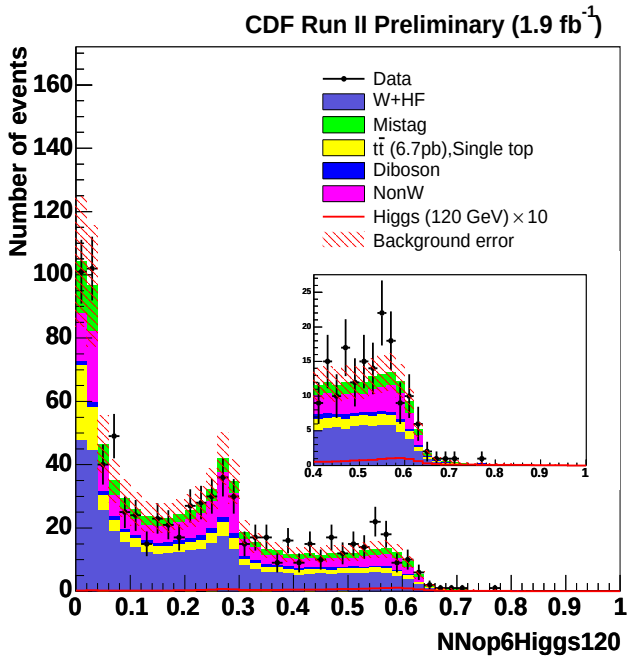

Figure 8.37: NN output shape calculated from the six input variables for one SECVTX tag w/ NN tag events. The Higgs signal should result large NN output values. Background uncertainty is shown in red hash.

8.3 The description of most Higgs signal like candidate

The highest neural network output value mean the most Higgs like event. In double SECVTX b-tagging events, there is one event which has much high neural network output. We describe the properties about this events.

The event has typical W + 2 jets signature. One electron in central region and large missing transverse energy is observed. Two jets are tagged by SECVTX b-tagging. The run number and event number is 234754 and 365736, respectively. The data is observed at CDF on February 2007. Table 8.5 shows the fundamental properties of this event. Figure 8.38 shows the various event displays of this interesting event.

NN output	0.84
E_T (CEM)	85.2 GeV
$\not\!\!E_T$	75.7 GeV
E_T (Jet1)	92.0 GeV
E_T (Jet2)	75.5 GeV
W transverse mass	57.2 GeV/c^2
M_{jj}	115.5 GeV/c^c

Table 8.5: The properties of highest neural network output event

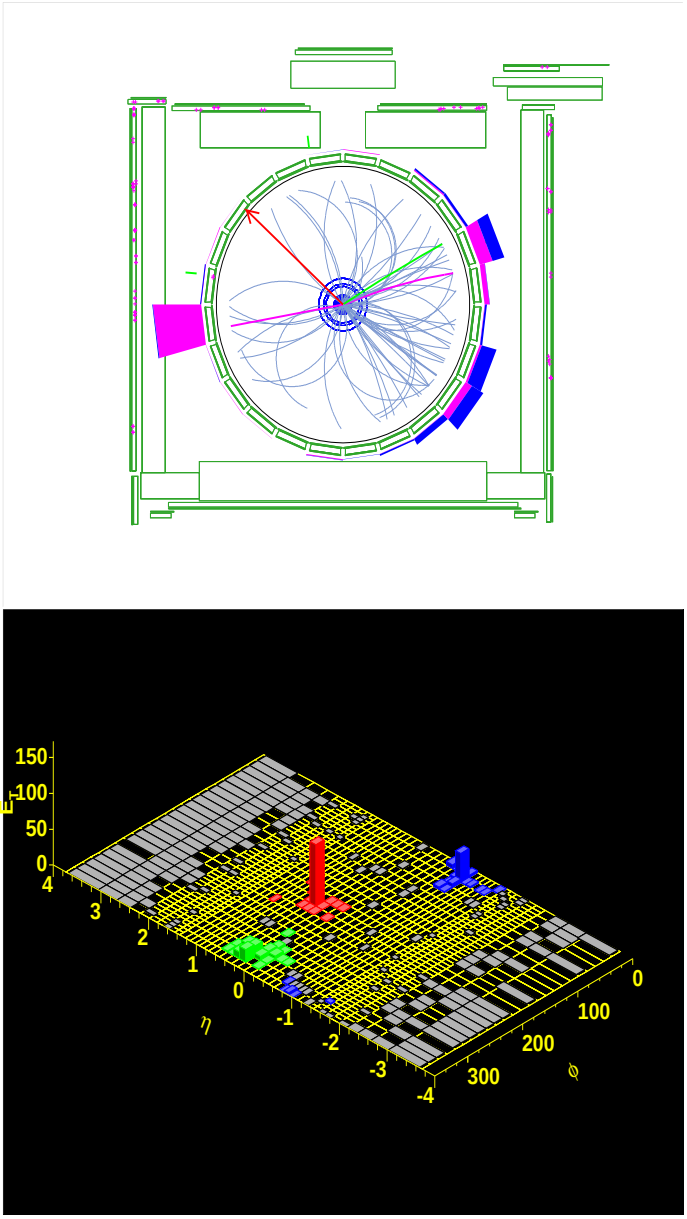

Figure 8.38: The view of most Higgs like event in $r - \phi$ plane (Top). The arrow indicates the direction of missing transverse energy of this event. The view of most Higgs event in $\eta - \phi$ plane (Bottom). Sharpest peak indicates the electron energy in calorimeter. Next sharpest two peaks indicate observed two jets.

Chapter 9

Upper Limits on Higgs Boson Production Cross Section

This chapter describes the upper limit on the WH production cross section times the branching ratio Higgs decaying into $b\bar{b}$ as a function of the Higgs boson mass because the observed data distribution show no evidence of excess and is consistent with the Standard Model background. The binned likelihood technique for Neural Network output distributions are used to set a limit. The procedure of binned likelihood technique is described and then finally a 95% confidence level upper limit is obtained.

9.1 Binned Likelihood Technique

To quantify the consistency between the CDF data and the expected background, a method of fitting technique called "binned likelihood" is considered. This method takes care of uncertainties associated with each bin content from the two histograms. The data counts in each bin is supposed to be fluctuating under Poisson statistics. The Poisson probability is

$$P_i(n_i, \mu_i) = \frac{\mu_i^{n_i} e^{-\mu_i}}{n_i!} (i = 1, 2, \cdots, N_{bin}) \tag{9.1}$$

where n_i is the number of events observed in the i-th bin, μ_i is the expected number of events in the i-th bin and N_{bin} stands for the number of bins in the target histogram. The expected number of events is represented as the sum of the numbers of signal and background events

$$\mu_i = s_i + b_i$$

where b_i means the number of background in the i-th bin and s_i mans the number of expected signal. s_i is written as a function of production cross section times branching ratio,

$$s_i(\sigma \cdot BR) = \sigma(p\bar{p} \rightarrow WH) \cdot BR(H \rightarrow b\bar{b}) \cdot \epsilon_{WH \rightarrow \ell\nu b\bar{b}} \cdot \int \mathcal{L} dt \cdot f_i^{WH \rightarrow \ell\nu b\bar{b}}$$

where $f_i^{WH \rightarrow \ell\nu b\bar{b}}$ is a signal fraction in the i-th bin. $\sigma(p\bar{p} \rightarrow WH) \cdot BR(H \rightarrow b\bar{b})$ is a parameter and the upper limit is set for $\sigma \cdot BR$. The likelihood utilizing the best binning information is defined as the multiplication of each bin probability.

$$\mathcal{L} = \prod_{i=bin} \frac{\mu_i^{n_i} \cdot e^{-\mu_i}}{n_i!}$$

For the background prediction b_i, it is categorized into two sources, QCD (mistags, $W^{\pm} + b\bar{b}$, $W^{\pm} + c\bar{c}$, Z+jets and dibosons), and TOP ($t\bar{t}$ and single top). Now b_i is written as

$$b_i = N_{TOP} f_i^{TOP} + N_{QCD} f_i^{QCD}$$

where N_{TOP} and N_{QCD} are the numbers of expected Top and QCD background,respectively. f_i^{TOP} and f_i^{QCD} are the background fractions of each background source in the i-th bin. Finally the binned likelihood is given by

$$L(\sigma \times BR) = \iiint \prod_{i=bin} \frac{\mu_i^{N_i} \cdot e^{-\mu_i}}{N_i!} G(\bar{N}_{QCD}, \sigma_{N_{QCD}}) G(\bar{N}_{TOP}, \sigma_{N_{TOP}}) G(\bar{N}_{WH}, \sigma_{N_{WH}}) dN_{QCD} dN_{QCD} dN_{WH}, \quad (9.2)$$

where $\bar{N}$ is the number of expected background. G is the Gaussian function defined by

$$G(\bar{X}, \sigma_X) = \frac{1}{\sqrt{2\pi}\sigma_X} \exp\left(-\frac{(x-\bar{X})^2}{2\sigma_X^2}\right)$$

The systematic uncertainties of the signal and backgrounds are taken into account by this Gaussian smearing by convoluting with this integration. The maximum of this likelihood gives the most probable $\sigma \times BR$. An upper limit on a certain confidence level is obtained by one side examination. Figure 9.1 shows the definition of 95% C.L. upper limit from the likelihood distribution. The upper limit for $\sigma \times BR$ is obtained from

$$95\% = \frac{\int_0^{\alpha_{95\%}} L(\alpha) d\alpha}{\int_0^{\infty} L(\alpha) d\alpha}$$

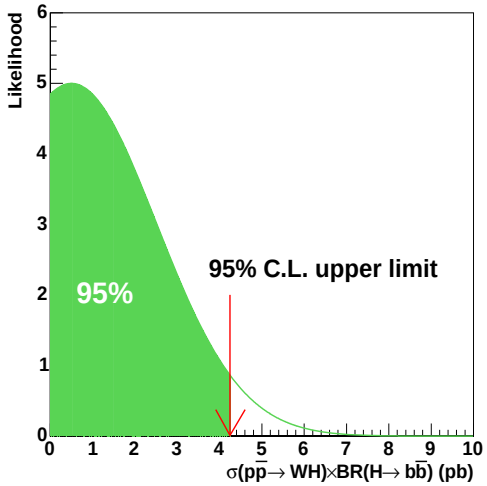

Figure 9.1: The 95% C.L. upper limit extracted from the likelihood distribution.

9.1.1 Combined Upper Limit

Three event categories were studied for SECVTX double tag (ST+ST), one SECVTX tag plus Jet probability tag (ST+JP) and one SECVTX tag w/ NN tag. The likelihood distribution for each category is multiplied to be defined the combined likelihood

$$L(\sigma \cdot BR) = L(\sigma \cdot BR|ST + ST) \times L(\sigma \cdot BR|ST + JP) \times L(\sigma \cdot BR|\text{1tag w/ NNtag})$$

where the correlation of three categories need to be considered. The systematic uncertainties on combined likelihood are divided into fully correlated part and uncorrelated part. The systematics on the acceptance before b-tagging is fully correlated due to the same source in the three categories, such as the luminosity uncertainty. The uncertainty on the b-tagging scale factor is also 100% correlated. Other uncertainty is asummued as uncorrelated.

9.2 Upper limit using Neural Network discriminant results

An expected binned maximum likelihood technique as discussed above is used to extract the upper limit on the Higgs production cross section times the decay branching ratio, $\sigma \times BR$. We first estimate the Higgs search sensitivity using Monte Carlo simulation, "pseudo-experiment", before starting the CDF data analysis. This is performed using "Pseudo-data' which is generated by fluctuating the background estimate with total uncertainties along a Gaussian and each bin entry with Poisson. Assuming such a pseudo data to be a real data with no signal, Figures 9.2-9.5 show distribution of 95% C.L. upper limit results from one thousand pseudo-experiments for the SECVTX double tag (ST+ST), one SECVTX plus Jet probability tag (ST+JP) and one SECVTX with NN tag categories, respectively. The median is quoted as the central value of pseudo-experiments for the expected limit and the RMS provides the 1 σ uncertainty band. The upper limit can be set using the Neural Network output distribution introduced to increase the sensitivity. In this section we show the results using the neural network discriminant.

9.2.1 Expected Limit Using Neural Network Output

One thousand pseudo-experiments are attempted using Neural Network output distributions. The 95% C.L. upper limits calculated from the pseudo-experiments are shown in Figures 9.2, 9.3 and 9.4 and 9.5 combined three categories. The expected limits are obtained from the median and sigmas of the distributions. Figure 9.6 shows the expected 95% C.L. upper limits estimated by fitting the NN output shape in double tag and one tag categories. To obtain maximal sensitivity, the neural network was trained for each Higgs mass point. We improve the upper limit sensitivity by 10% using additional kinematic infomation in the neural network beyond the dijet invariant mass.

The obtained expected 95% upper limits are summalized in Table 9.1. We obtain the expectations with assuming null signal. The best sensitivity result is given by ST+ST, ST+JP and one SECVTX w/ NN tag combined result.

9.2.2 Observed Limit Using Neural Network Output

Figure 9.7 shows observed 95% C.L. upper limit of $\sigma(p\bar{p} \rightarrow WH) \times BR(H \rightarrow b\bar{b})$ combined for three categories, ST + ST, ST + JP and one SECVTX with NN tag. This observed limit is consistent with the expected limits. As a cross-check, we calculate the observed 95% C.L. upper

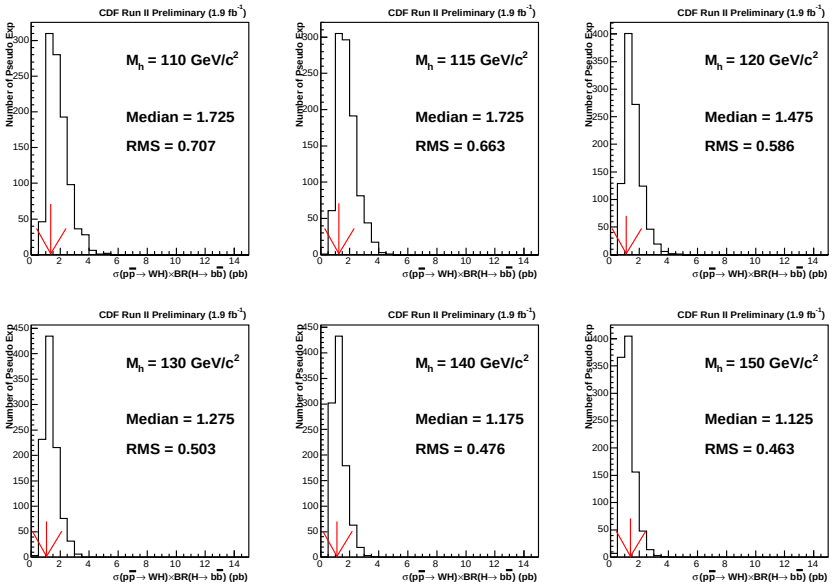

Figure 9.2: The 95% C.L. upper limit distributions from one thousand pseudo-experiments using double SECVTX tag.

limit for three tag categories separately. The results are shown in Figure 9.8. The observed 95% C.L. upper limit from combination three b-tagging categories is

$$\sigma(p\bar{p} \rightarrow WH) \times BR(H \rightarrow b\bar{b}) < 1.4 \sim 0.9 \text{ pb}$$

for the Higgs mass from 110 GeV/c^2 to 150 GeV/c^2. It corresponds to 8.5 - 78.9 times higher than the Standard Model expectation. Table 9.2 summarizes the observed limits at Higgs boson mass points, including that normalized by the Standard Model expectation.

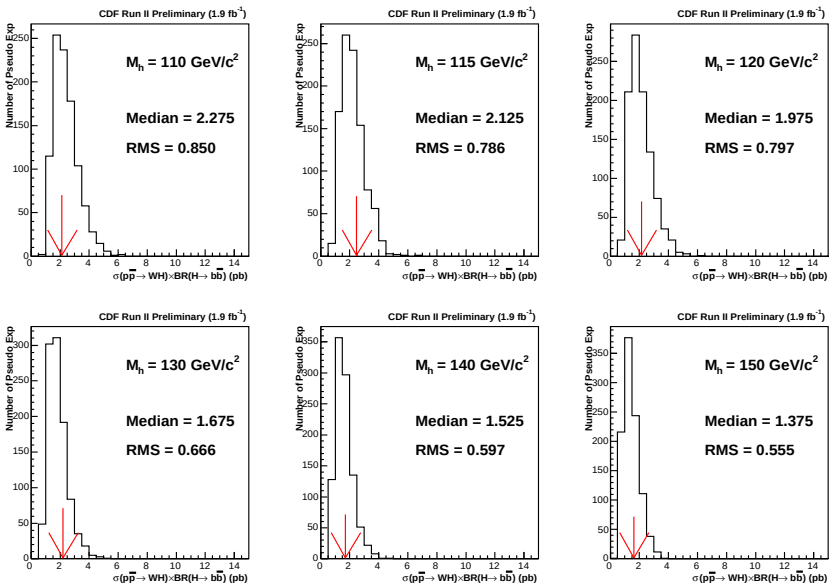

Figure 9.3: The 95% C.L. upper limit distributions from one thousand pseudo-experiments using one SECVTX tag plus one Jet probability tag.

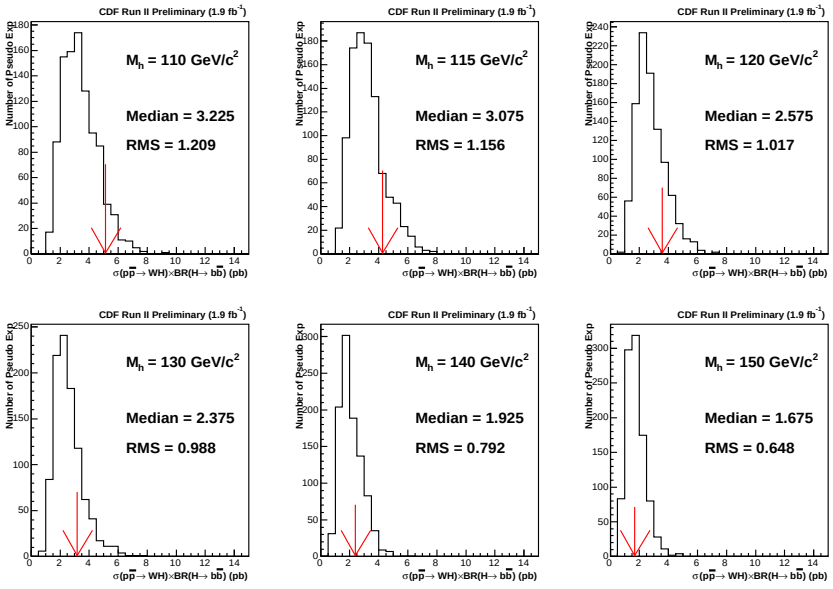

Figure 9.4: The 95% C.L. upper limit distributions from one thousand pseudo-experiments using one SECVTX tag with NN tag.

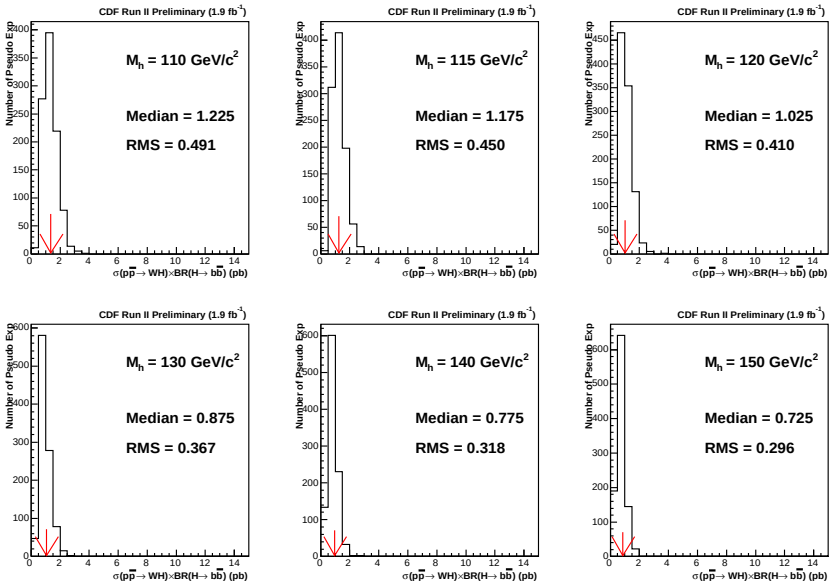

Figure 9.5: The 95% C.L. upper limit distributions from one thousand pseudo-experiments using double SECVTX tag, one SECVTX tag plus one Jet probability tag and one SECVTX tag with NN tag combined.

Mass/category	ST + ST	ST + JP	1tag w/ NNtag	1tag & 2tag
110 GeV/c^2	1.73 (10.7)	2.28 (14.1)	3.23 (19.9)	1.23 (7.6)
115 GeV/c^2	1.73 (13.1)	2.23 (16.2)	3.08 (23.4)	1.18 (8.9)
120 GeV/c^2	1.48 (14.5)	1.98 (19.4)	2.58 (25.2)	1.03 (10.0)
130 GeV/c^2	1.28 (20.4)	1.68 (26.8)	2.38 (38.1)	0.88 (14.0)
140 GeV/c^2	1.18 (38.4)	1.53 (49.8)	1.93 (62.9)	0.78 (25.3)
150 GeV/c^2	1.13 (95.9)	1.38 (117.0)	1.68 (142.8)	0.73 (61.8)

Table 9.1: The expected upper limits on $\sigma \times BR$ [pb] using the NN shape fit for Higgs mass points in three tagging categories. The values in parentheses are the upper limit normalized to the SM expectation.

Mass/category	ST + ST	ST + JP	1tag w/ NNtag	1tag & 2tag
110 GeV/c^2	1.43 (8.8)	2.18 (13.5)	5.13 (31.7)	1.38 (8.5)
115 GeV/c^2	1.33 (10.1)	2.48 (18.8)	4.28 (32.5)	1.28 (9.7)
120 GeV/c^2	1.13 (11.0)	2.18 (21.3)	3.63 (35.5)	1.08 (10.5)
130 GeV/c^2	1.08 (17.2)	2.23 (35.6)	3.18 (50.9)	1.08 (17.2)
140 GeV/c^2	1.18 (38.4)	1.78 (58.0)	2.43 (79.2)	0.98 (31.9)
150 GeV/c^2	1.43 (121.5)	1.63 (138.5)	1.73 (147.1)	0.93 (78.9)

Table 9.2: The observed upper limit $\sigma(p\bar{p} \rightarrow WH) \times BR(H \rightarrow b\bar{b})$ [pb] using NN shape fit for Higgs mass points in three tagging categories. The values in parentheses are the upper limits normalized to the SM expectation.

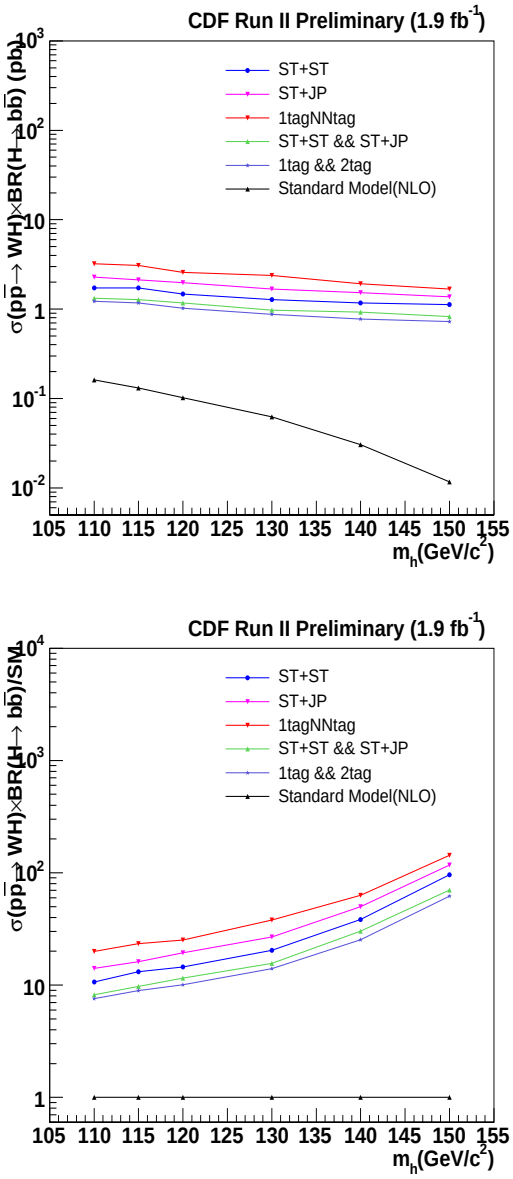

Figure 9.6: The expected 95% C.L. upper limit calculated from the NN shape (top) and that normalized to the SM expectation (bottom).

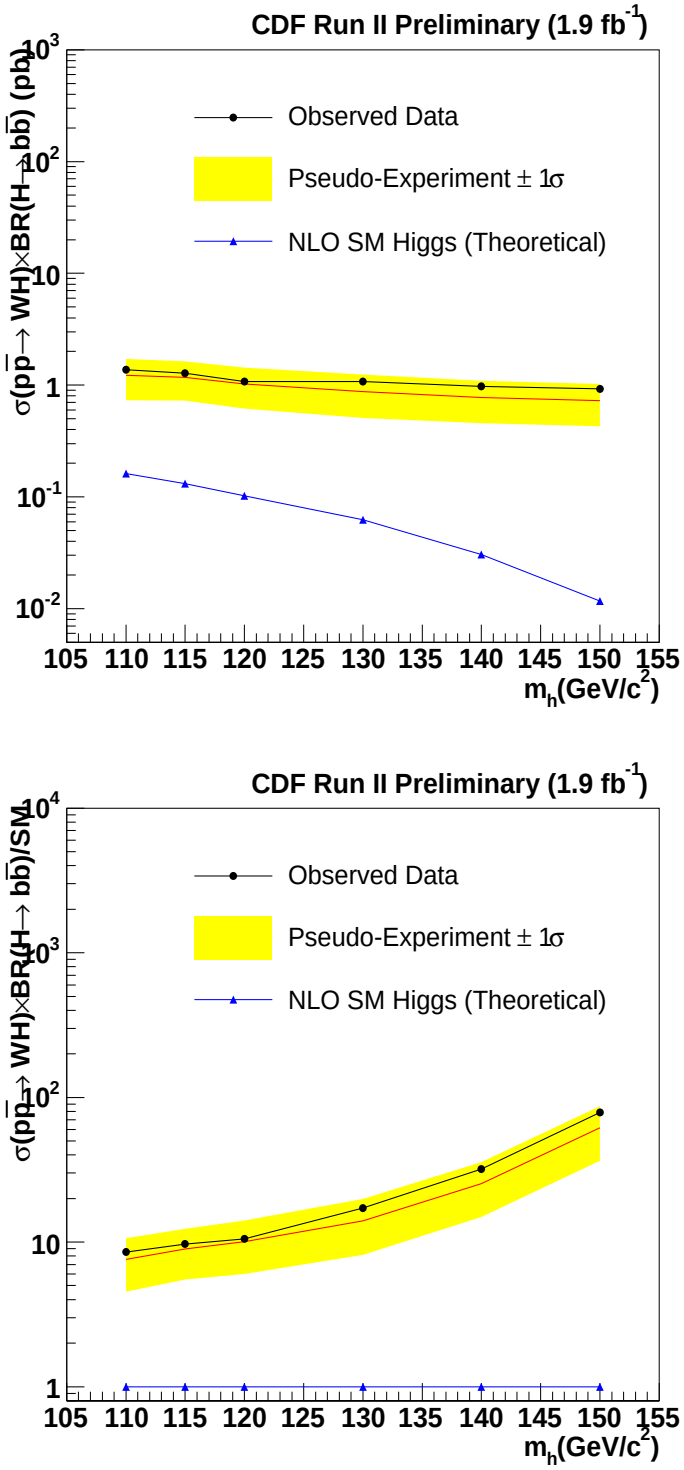

Figure 9.7: The observed limit on $\sigma(p\bar{p} \rightarrow WH) \times BR(H \rightarrow b\bar{b})$ calculated from the NN output shape (top). The bottom plots is that normalized to the SM expectation. The two categories of double SECVTX, one SECVTX tag + Jet probability tag and one SECVTX tag with NN tag are combined.

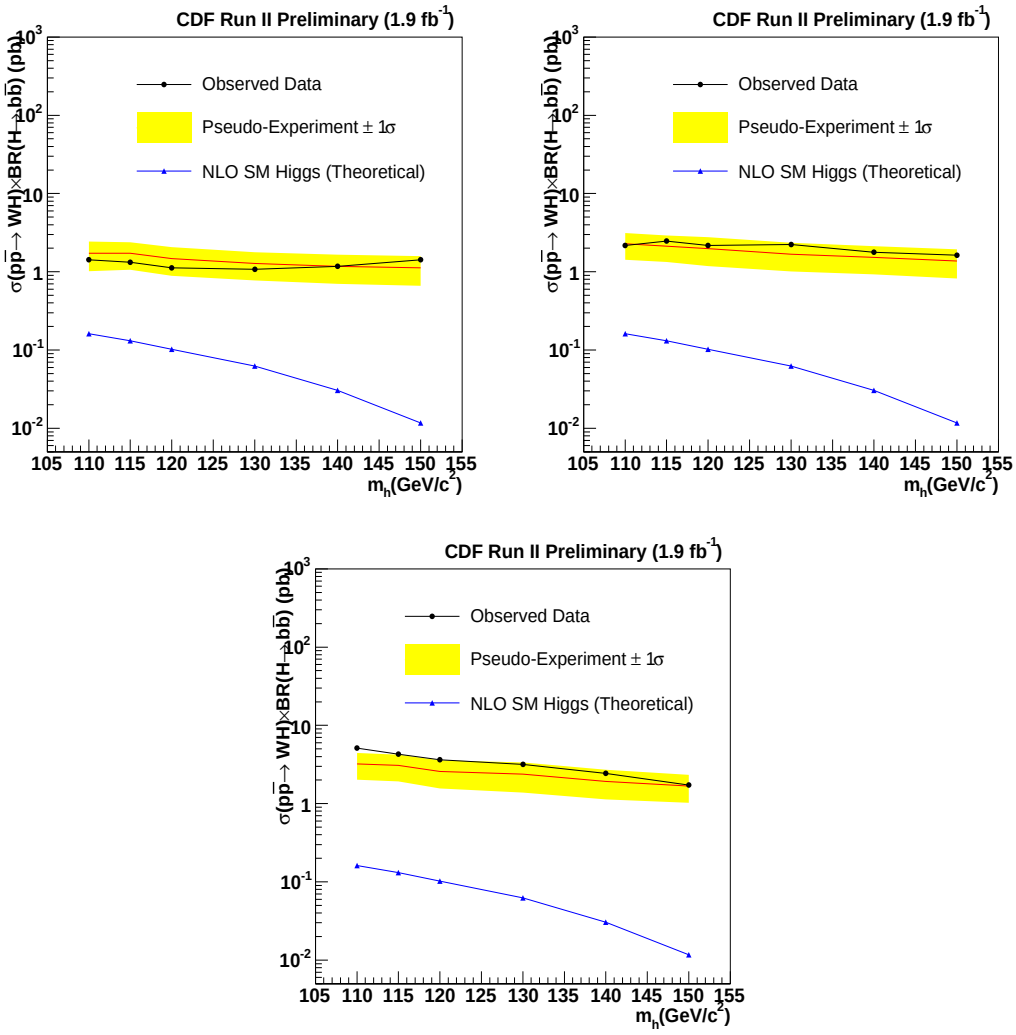

Figure 9.8: The observed 95% C.L. upper limit on $\sigma(p\bar{p} \rightarrow WH) \times BR(H \rightarrow b\bar{b})$ calculated from the NN shape for double SECVTX (top left), one SECVTX tag + Jet probability tag (top right) and one SECVTX tag with NN tag(bottom).

Chapter 10

Conclusion

We have searched for the Standard Model Higgs boson produced in association with a W boson in 1.96 TeV $p\bar{p}$ collisions with the CDF detector . The data are collected from February 2002 to May 2007 corresponding to an integrated luminosity of 1.9 fb^{-1} . We have developed double b-tagging to enhance the search sensitivity for the Higgs boson decaying into $b\bar{b}$. The double b-tagging is realized using double SECVTX tag (ST+ST), one SECVTX tag plus one Jet Probability tag (ST+JP) and one SECVTX w/ NN tagging.

If the Standard Model Higgs boson (m_h = 120 GeV/c^2) exists, the expected number of signal events are 0.94, 0.74 and 1.82 in ST+ST, ST+JP and one SECVTX w/ NN tagging categories, respectively. The numbers of observed events of 83, 90 and 805 agree with the Standard Model background predictions within the uncertainties. The observed 95% C.L. upper limit using the neural network ranges from 1.4 pb (for $m_h = 110$ GeV/c^2) to 0.9 pb (for m_h = 150 GeV/c^2).

In the WH channel, the current upper limit of low mass region is about 10 times higher than the Standard Model expectation due to the statistical limitation. Other channel [22, 23, 71] in addition to the WH channel are combined to search for the Higgs boson. The combined CDF Higgs discovery sensitivity is further improved [78]. Another Tevatron experiment D0 also gives the 95% C.L. upper limit on the Higgs search using various channels [72–77]. Figure 10.1 shows the current Tevatron (CDF+D0) combined 95% C.L. upper limit which is 4.2 - 1.1 (for $m_h = 115$ - 160 GeV/c^2) times higher than the Standard Model expectation [79].

In the next couple of years during LHC (14 TeV pp collider at CERN) is commissioning, the Tevatron Collider still continues to provide interesting data on the search for the Higgs boson. The Tevatron will deliver 3-4 times of luminosity by 2010. The new physics beyond the Standard Model will be opened or the strong constraint for the Standard Model, especially Higgs boson, will be imposed in new data. It would be possible to even discover Higgs boson in near future at Tevatron.

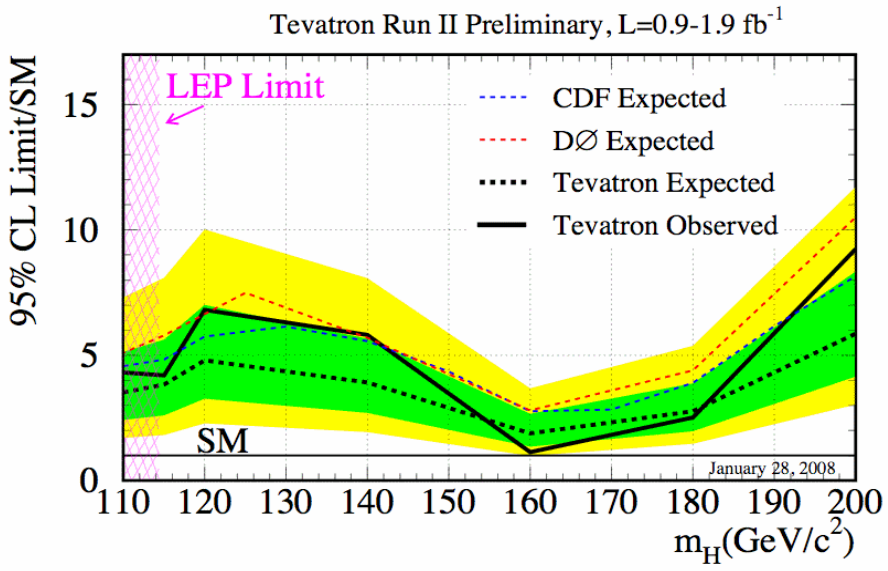

Figure 10.1: The current Tevatron (CDF+D0) combined 95% C.L. upper limit as a function of Higgs mass.

Appendix A

Non-W Background Validation

A.1 Anti-Electron Method

There are small discrepancy between data and expected background shape. The non-isolated region of lepton and high $\not\!\!E_T$ region (C Region) is are used as non-W shape modeling. An alternative QCD background modeling is investigated. The impact of non-W background modeling for the upper limit is also discussed.

The alternative modeling is made from high p_T electron data set. The fake lepton events are selected by requiring an electron cluster which passes all the electron identification criteria but fails at least two identification variables. These variables are listed in Table A.1. We check the difference between C Region modeling and anti-electron modeling by comparing the kinematic shape.

Variables	E_{HAD}/E_{EM}	L_{shr}	CES χ^2	CES Δx	CES Δz

Table A.1: The anti-electron modeling require that at least two variables of five fail criteria.

A.2 The Comparison between C Region Modeling and Anti-Electron Modeling

The difference between two non-W background modeling is validated for six neural network input shape and output shape. The number of non-W background and other backgrounds are identical to validate non-W modeling only. Figure A.1 shows six neural network input variables in one SECVTX w/ NN tag events which has largest non-W contribution. Both modeling is reasonably agreement with observed data except for ΔR(lepton-ν_{max}) and Pt of W + 2jets. While C Region shape is better agreement for reconstructed dijet invariant mass plus. Figure A.2 shows neural network output distribution. The result of neural network output of C Region is slightly better than anti-electron shape in background region and the significant difference between two non-W modeling is not observed in signal region. We also check the other variables for two non-W modeling in Figure A.3-A.9. The current data indicates the middle of two modelings. We don't conclude which is better modeling. However we check the impact of non-W modeling for final results using pseudo-experiments. The pseudo-data made from anti-electron modeling case is used in pseudo-experiments. The fitting is performed using C Region non-W modeling. The difference for upper limit is a few % level. This modeling issue is not sensitive on final results.

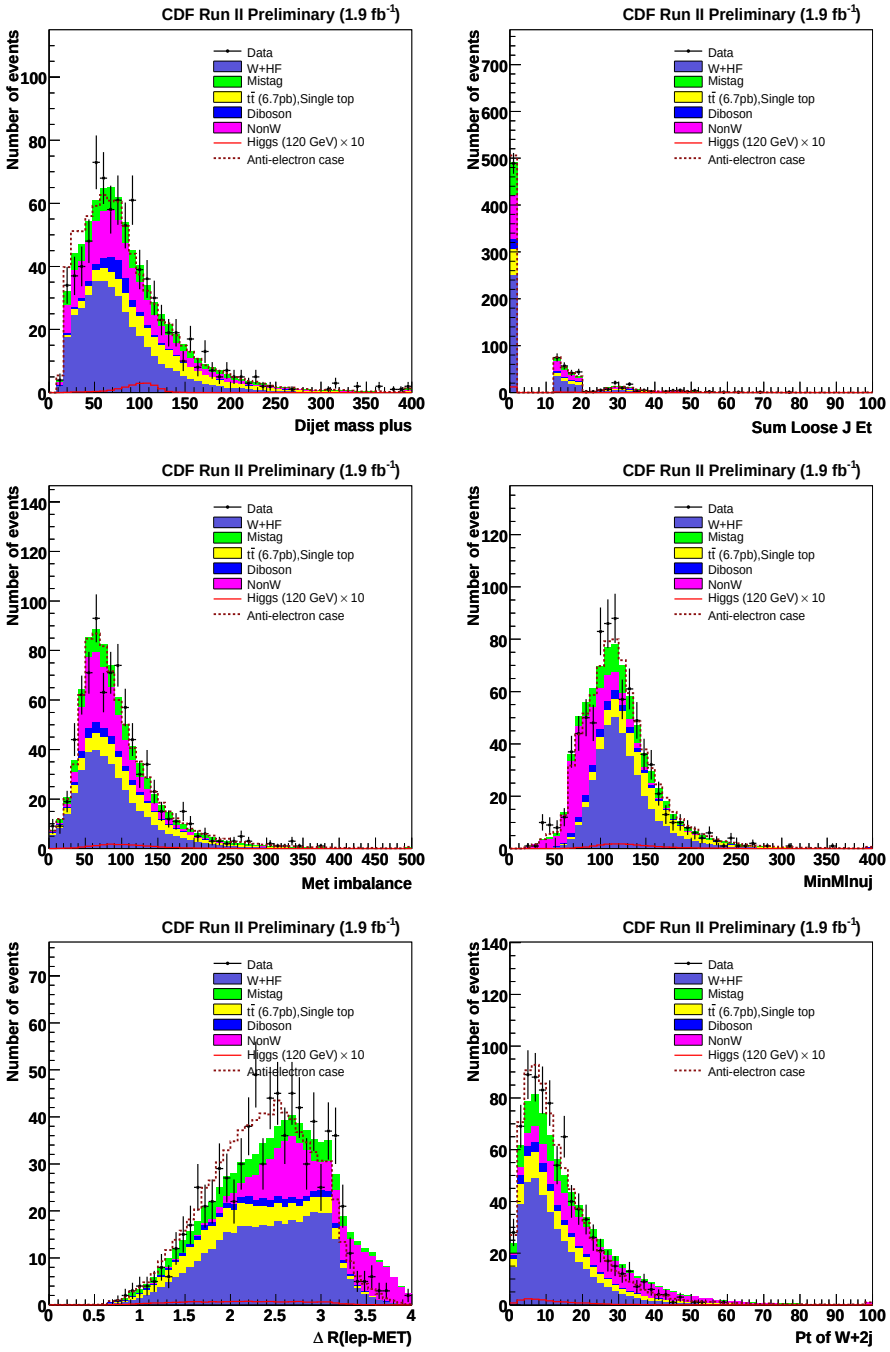

Figure A.1: The observed and expected six NN input variables, Dijet mass+, scalar sum of the loose jet transverse energy, p_T imbalance, the invariant mass of lepton, $\not\!\!E_T$ and one of two jets, Δ R(lepton-ν) and p_T of W+2jet system in the one SECVTX with NN tag events. Anti-electron shape is shown in dotted line.

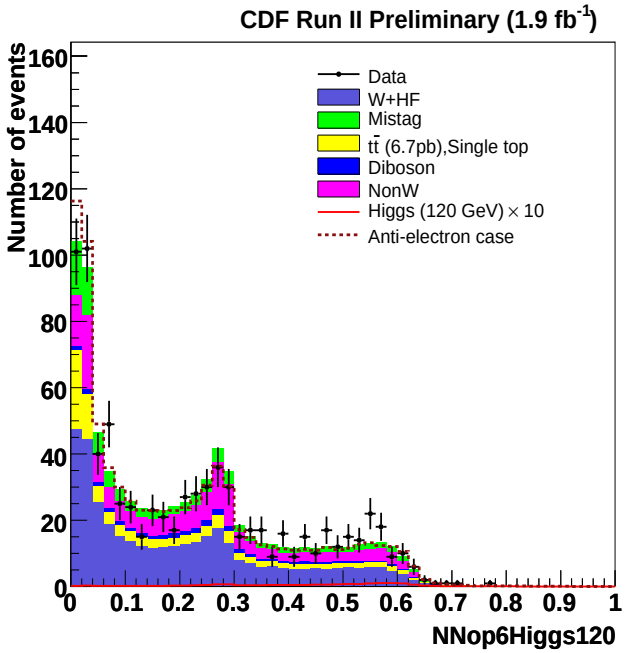

Figure A.2: NN output shape calculated from the six input variables for one SECVTX with NN tag events. The Higgs signal should result large NN output values. Anti-electron shape is shown in dotted line.

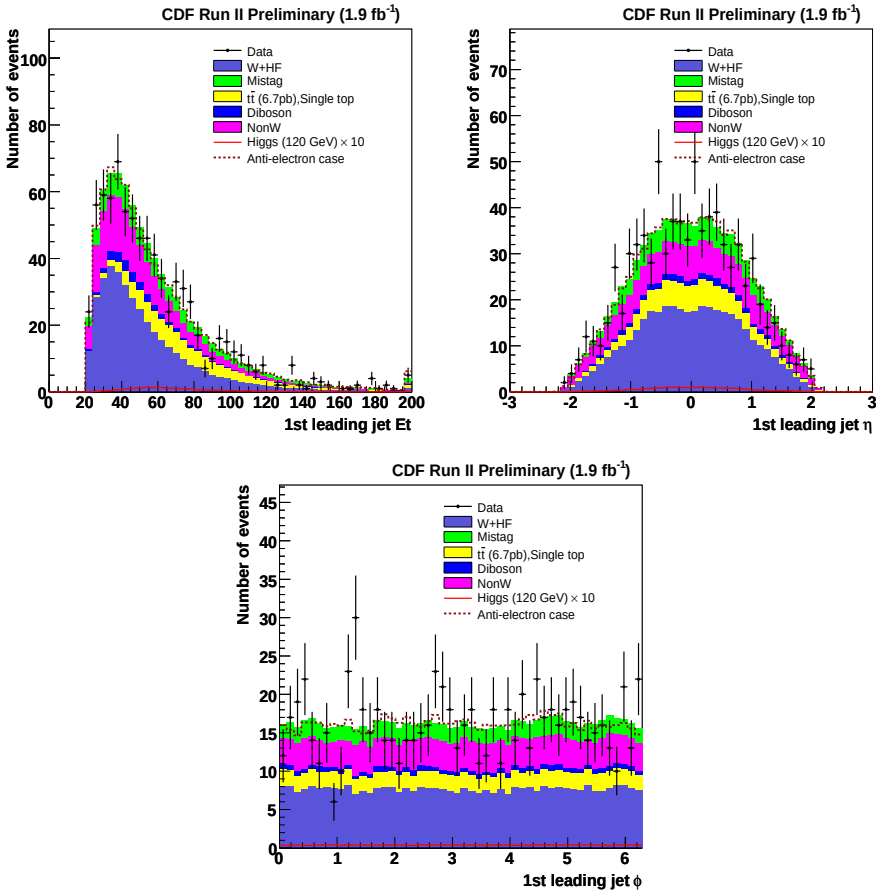

Figure A.3: First leading jet E_T, η and ϕ kinematic distributions in one SECVTX with NN tag events. Anti-electron shape is shown in dotted line.

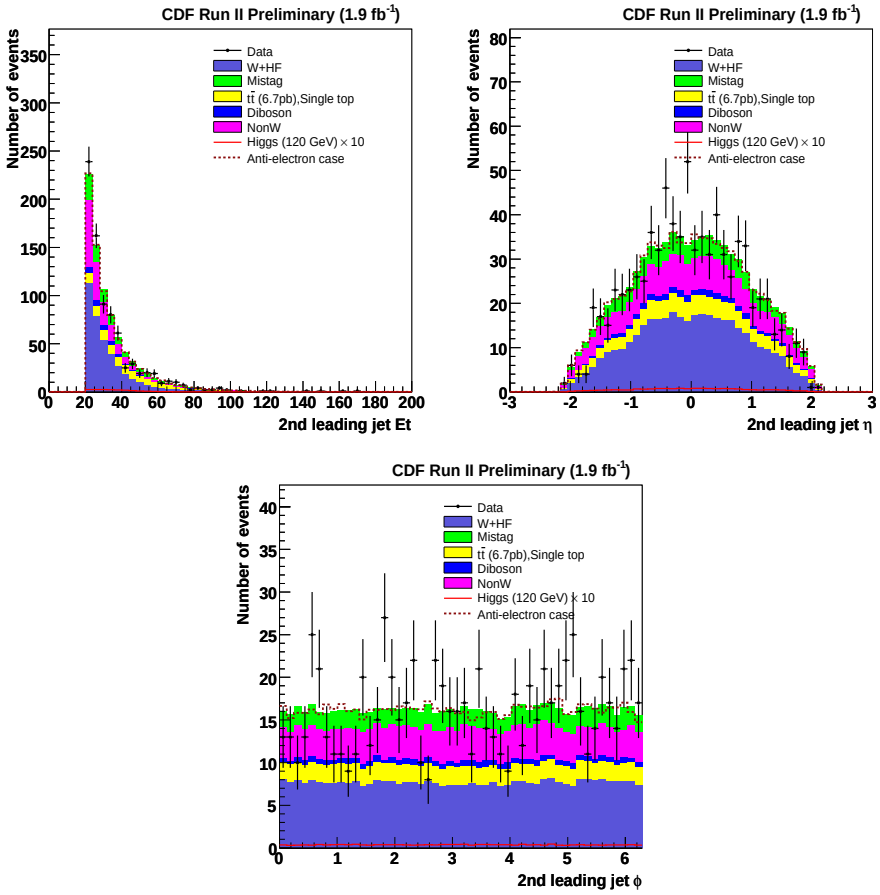

Figure A.4: Second leading jet E_T, η and ϕ kinematic distributions in one SECVTX with NN tag events. Anti-electron shape is shown in dotted line.

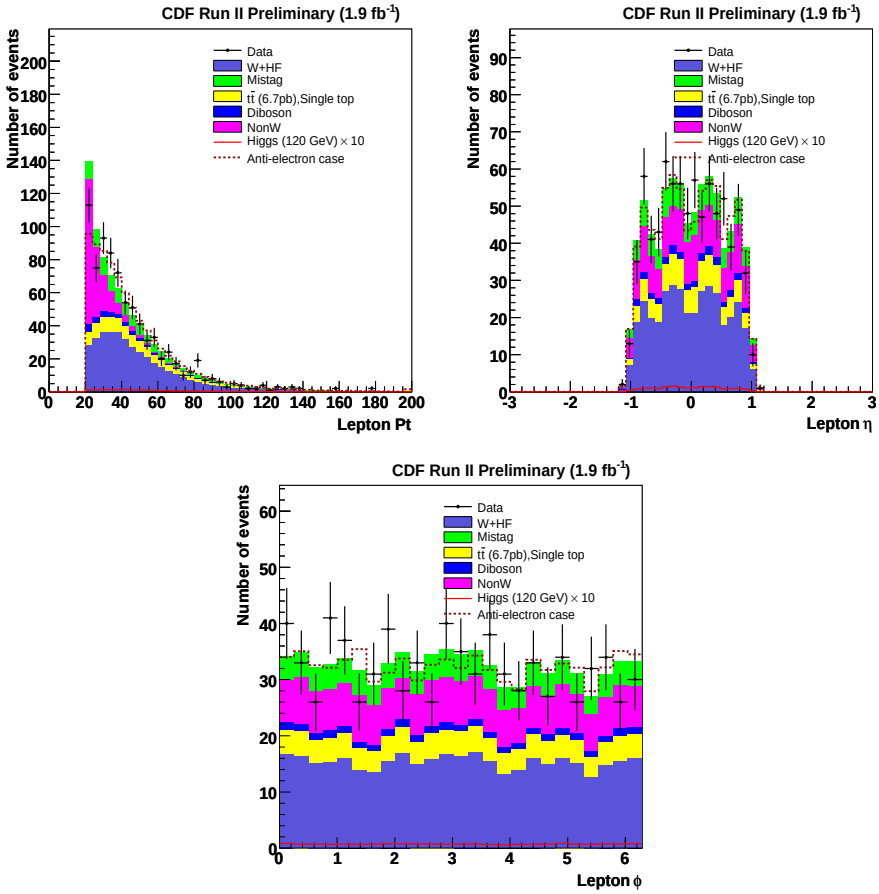

Figure A.5: Lepton p_T, η and ϕ kinematic distributions in one SECVTX with NN tag events. Anti-electron shape is shown in dotted line.

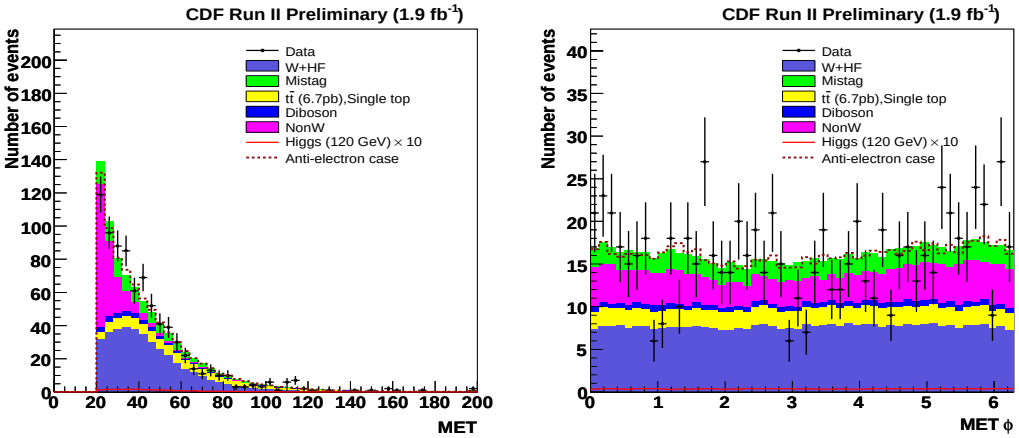

Figure A.6: $\not\!\!E_T$ and ϕ kinematic distributions in one SECVTX with NN tag events. Anti-electron shape is shown in dotted line.

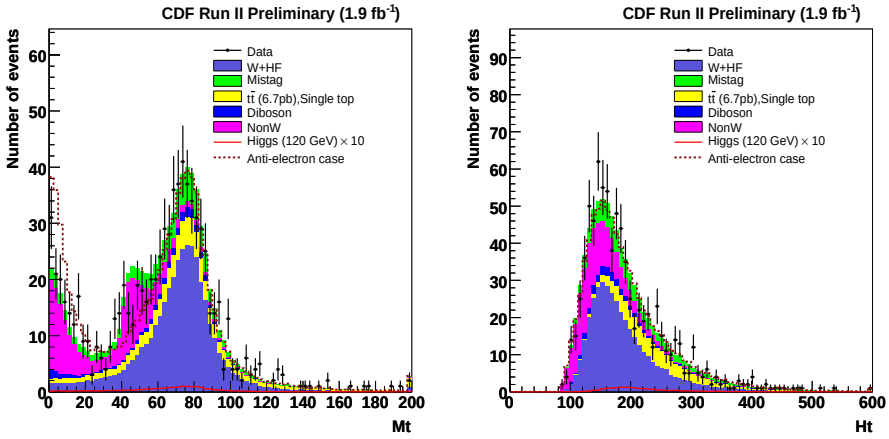

Figure A.7: W transverse mass and Ht distributions in one SECVTX with NN tag events. Anti-electron shape is shown in dotted line.

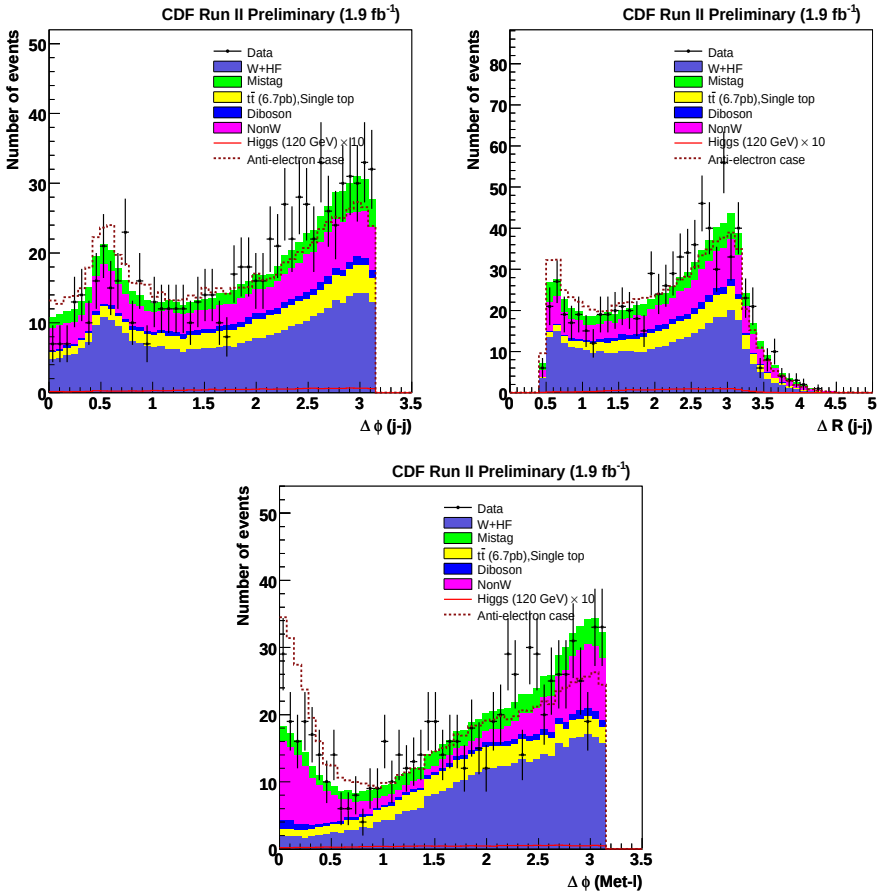

Figure A.8: Distribution of $\Delta\phi$ between dijet, ΔR between dijet and $\Delta\phi$ between $\not\!\!E_T$ and lepton in one SECVTX with NN tag events. Anti-electron shape is shown in dotted line.

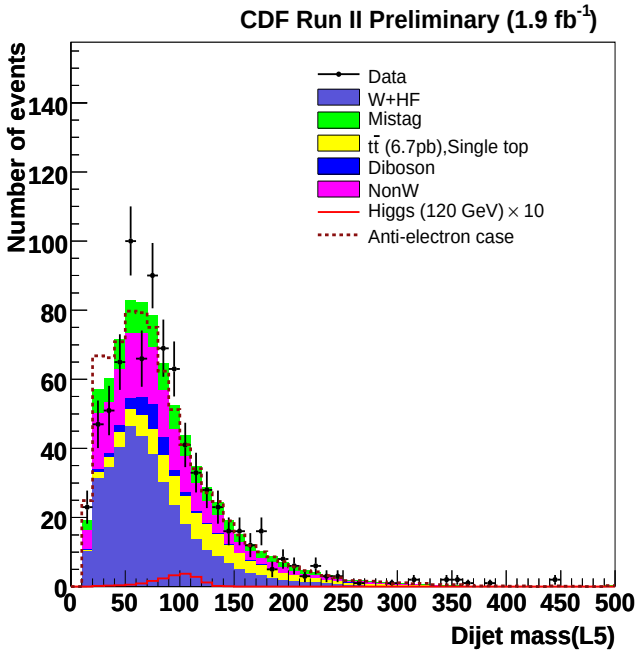

Figure A.9: Reconstructed invariant mass of 2 jets system in one SECVTX with NN tag events. Anti-electron shape is shown in dotted line.

Bibliography

[1] D.Gross, F.Wilczek, Phys. Rev. Lett. **30**, 1343 (1973).

[2] H.D. Politzer, Phys. Rept. **14**, 129 (1974).

[3] S. Weinberg, Phys. Rev. Lett. **19**, 1264 (1967).

[4] A. Salam and J.C. Ward, Phys. Rev. Lett. **13**, 168-171 (1964).

[5] S. Glashow, Nucl. Phys. **22**, 579 (1961).

[6] S.L. Glashow, J.Iliopoulos and L. Maiani, Phys. Rev. D **2**, 1285 (1970).

[7] M. Gell-Mann, Phys. Lett. **8**, 214-215 (1964).

[8] L. Randall and R. Sundrum, Phys. Rev. Lett. **83**, 3370-3373 (1999).

[9] Th. Kaluza, Sitzungsber, Preuss. Akad. Wiss. Berlin (Math.Phys) (1921).

[10] P.W. Higgs, Phys. Lett. **12**, 132-133 (1964).

[11] A. Djouadi, hep-ph/0503172v2 (2005).

[12] B. Lee, C. Quigg and H. Thacker, Phys. Rev. Lett. **38**, 883 (1977).

[13] A. Djouadi, J. Kalinowski and M. Spira, Comput. Phys. Commun. **108**, 56 (1998).

[14] http://www.physics.ucdavis.esu/ conway/research/higgs/higgs.html.

[15] Tev4LHC Higgs working group at http://maltoni.home.cern.ch/maltoni/TeV4LHC/SM.html.

[16] N. Cabibbo, Phys. Rev. Lett. **10**, 531-532 (1963).

[17] M. Kobayashi, T. Maskawa, Prog. Theor. Phys. **49**, 652-657 (1973).

[18] ALEPH, DELPHI, L3, and OPAL Collaborations and LEP Working Group for Higgs Boson Searches, Phys. Lett. B **565**, 61 (2003).

[19] The LEP Collaborations ALEPH, DELPHI, L3, OPAL and the LEP Electroweak Working Group, arXiv:0712.0929 [hep-ex].

[20] A. Abulencia *et al.* (CDF Collaboration), Phys. Rev. Lett. **96**, 081903 (2006).

[21] T. Aaltonen *et al.* (CDF Collaboration), Phys. Rev. Lett. **100**, 041801 (2008).

[22] J. Efron *et al.*, CDF Public Note 8742 (2007).

[23] The CDF Collaboration, CDF Public Note 8442 (2006).

[24] A. Abulencia *et al.*, The CDF Collaboration, Phys. Rev. Lett. 97, 081802 (2006).

[25] Y. Kusakabe, T. Masubuchi, J. Nielsen, A. Taffard, W. Yao for Higgs Working Group, CDF Public Note 8403 (2006).

[26] The D0 Collaboration, D0note 5054-CONF (2006).

[27] The D0 Collaboration, Phys. Lett. B. **655**, 209 (2007).

[28] The D0 Collaboration, Phys. Rev. Lett. **97**, 161803 (2006).

[29] The D0 Collaboration, Phys. Rev. Lett. **97**, 151804 (2006).

[30] The D0 Collaboration, D0note 5194-CONF (2006).

[31] The D0 Collaboration, D0note 5056-CONF (2006).

[32] The TEVNPH Working Group, CDF Public Note 8384, D0 Note 5227 (2006).

[33] F. Halzen, A.D. Martin, "Quarks & Leptons": An Introductory Course in Modern Particle Physics", John Wiley & Sons, Inc (1984).

[34] J.F. Gunion *et al.*, The Higgs Hunter's Guide, Westview Press (1990).

[35] T. Affolder *et al.*, CDF Public Note 6267 (2003).

[36] T. Affolder *et al.*, CDF Public Note 5687 (2001).

[37] D. Acosta *et al.*, Nucl. Instrum. Meth. A **461**, 540 (2001).

[38] D. Acosta *et al.*, Nucl. Instrum. Meth. A **494**, 57 (2002).

[39] E.J. Thomson *et al.*, IEEE Trans. Nucl. Sci. **49**, 1064 (2002).

[40] J. Fromm *et al.*, FERMILAB-CONF-98-359, 8pp. C98/08/31 (Dec 1998).

[41] M. Shimojima, *et al.*, IEEE Trans. Nucl. Sci. **47**, 236-239 (2000).

[42] F. Snider *et al.*, FERMILAB-CONF-07-102-E, RT2007-PS2C008 (2007).

[43] F.D. Snider, Nucl. Instr. and Meth. A **566** 133-141 (2006).

[44] C. Hays, Nucl. Instr. and Meth. A **538** 249-254 (2005).

[45] A. Bhatti, F. Canelli, B. Heinemann *et al.*, hep-ex/0510047 (2005).

[46] K. Hatakeyama, The CDF and D0 collaborations, FERMILAB-CONF-06-176-E (2006).

[47] K. Burkett, J. Da Costa, S. Rappoccio, CDF Public Note 6417 (2003).

[48] C. Neu (CDF Collaboration), "CDF b-tagging: Measuring Efficiency and False Positive Rate", FERMILAB-CONF-06-162-E. Published Proceedings TOP 2006 (2006).

[49] A. Abulencia *et al.* (CDF Collaboration), Phys. Rev. D **74**, 072006 (2006).

[50] E. Palencia, F. Garberson, CDF Public Note 8882 (2007).

[51] L. Lonnblad, C. Peterson, H.Pi, T. Rognvaldsson, Comput. Phys. Commun. **81**, 185 (1994).

[52] T. Masubuchi, Y. Kusakabe, M. McFarlane, J. Nielsen, A. Taffard, W. Yao, CDF Public Note 8272 (2006).

[53] T. Sjostrandm, S. Mrenna, P. Skands, JHEP 0605 (2006) 026.

[54] R. Field, R. Craig Group, the proceedings of the HERA-LHC workshops, hep-ph/0510198.

[55] M.L. Mangano, M.Moertti, F. Piccinini, R.Pittau, A.Polosa, JHEP 0307:001 (2003).

[56] J. Alwall *et al.*, arXiv:0706.2334.

[57] A. Ryd *et al.*, BAD 522 V6 (2006).

[58] http://root.cern.ch/.

[59] T. Ash, ICS Rep. 8901, Univ. California, San Diego, (February 1989).

[60] S. Richter *et al.*, A Neural Network b Tagger for Single-Top Analysis, CDF Note 7816 (2007).

[61] D. E. Acosta *et al.*, Phys. Rev. D **72**, 052003 (2005).

[62] A. Abulencia *et al.*, Phys.Rev. D **75**, 092006 (2007).

[63] B. Alvarez *et al.*, CDF Public Note 8899 (2007).

[64] A. Abulencia *et al.* (CDF Collaboration), Phys. Rev. D **75**, 092004 (2007).

[65] W-M. Yao *et al.*, Journal of Physics G **33**, 1 (2006).

[66] A. Bhatti et al.,Nucl.Instrum.Meth.A **566**, 375-412 (2006).

[67] Han, Boisvert, "Trigger Efficiencies for the High Et Central Electron in the Gen6 data", CDF Note 8629.

[68] D. Hare, E. Halkiadakis, T. Spreitzer, "Electron ID Efficiency and Scale Factors for Winter 2007 Analysis", CDF Note 8614.

[69] Grundler, Lovas, A. Taffard, "High-Pt muons recommended cuts and efficiencies for Winter 2007", CDF Note 8618.

[70] The CDF Collaboration, CDF Conference Note 9166 (2008).

[71] The CDF Collaboration, CDF Conference Note 8923 (2007).

[72] The D0 Collaboration, D0 Conference Note 5472 (2007).

[73] The D0 Collaboration, D0 Conference Note 5506 (2007).

[74] The D0 Collaboration, D0 Conference Note 5482 (2007).

[75] The D0 Collaboration, D0 Conference Note 5485 (2007).

[76] The D0 Collaboration, D0 Conference Note 5537 (2007).

[77] The D0 Collaboration, D0 Conference Note 5485 (2007).

[78] The CDF Collaboration, CDF Conference Note 8941 (2007).

[79] The TEVNPH Working Group for the CDF and D0 Collaborations, CDF Note 8961/D0 Note 5536 (2007).